Gating for scanned ion beam therapy

Bewegungssynchronisiert unterbrochene Bestrahlung für gescannte Ionenstrahltherapie
Zur Erlangung des Grades eines Doktors der Naturwissenschaften (Dr. rer. nat.)
genehmigte Dissertation von Dipl.-Phys. Peter Steidl aus Hadamar
Dezember 2011 — Darmstadt — D 17

TECHNISCHE
UNIVERSITÄT
DARMSTADT

GSI

Gating for scanned ion beam therapy
Bewegungssynchronisiert unterbrochene Bestrahlung für gescannte Ionenstrahltherapie

Genehmigte Dissertation von Dipl.-Phys. Peter Steidl aus Hadamar

1. Gutachten: Prof. Marco Durante, Ph.D.
2. Gutachten: Prof. Dr. Dr. h. c. Gerhard Kraft

Tag der Einreichung: 17. Oktober 2011
Tag der Prüfung: 12. Dezember 2011

Darmstadt — D 17

Zusammenfassung

Die Bestrahlung bewegter Tumore mit einem gescannten Teilchenstrahl bedarf besonderer Techniken, um durch die Bewegung verursachte Unter- und Überdosierungen zu vermeiden. Eine solche Technik ist die atemsynchronisiert unterbrochene Bestrahlung (Gating), mit der man eine Reduzierung der effektiven Tumorbewegung erreicht. Da diese allerdings nicht völlig kompensiert wird, kann es auch hier auf Grund des Interplay-Effekts zu unakzeptablen Dosisverteilungen kommen. Zudem ist ein Bewegungserfassungssystem erforderlich, mit dem Dosisapplikation und Zielbewegung synchronisiert werden.

In Experimenten und Simulationen wurde die Abhängigkeit des Interplay-Effekts für verschiedene Restbewegungsamplituden von Bestrahlungsparametern dosimetrisch untersucht. Es konnte nachgewiesen werden, dass insbesondere ein vergrößerter Strahlfokus zu einer signifikanten Reduzierung der Dosisinhomogenitäten führen kann.

Bei der Verwendung von Surrogaten zur Erfassung der Tumorbewegung kann es zu Ungenauigkeiten durch Fehlkorrelationen kommen. Um diese in zukünftigen Studien dosimetrisch quantifizieren zu können, wurde ein Phantom, das Thoraxatmung und unabhängige 6D-Tumorbewegung simulieren kann, entwickelt und erfolgreich experimentell validiert.

Schließlich wurden zwei Bewegungserfassungssysteme von VisionRT Ltd. bzw. Anzai Medical Co.,Ltd. evaluiert. Hauptaugenmerk lag dabei auf der Quantifizierung von Gating-Verzögerungen und auf der Korrelation zu Tumorbewegungen.

Die Ergebnisse dieser Arbeit werden für die Gating-Bestrahlungen von Patienten am HIT, die in den nächsten Monaten beginnen sollen, verwendet werden. Zudem steht nun ein Bestrahlungsphantom zur Verfügung, das viele Einsatzmöglichkeiten bietet und bereits jetzt von mehreren Forschungsgruppen genutzt wird.

Abstract

In treatment of motion affected tumours by means of a scanned particle beam severe under and over dosage can occur due to the interplay effect. By using gated beam delivery effective target motion is reduced, but even for the residual motion the interplay effect can lead to unsatisfactory dose distributions. Furthermore, an appropriate motion monitoring system is essential since beam delivery has to be synchronized to target motion.

In this work three aspects were investigated to move gating closer towards clinical operation at Heidelberg Ion-Beam Therapy Center (HIT): Firstly, influences of beam parameters on dosimetric effects of residual motion were investigated in experiments and simulations. Increased focus sizes and reduced iso-energy distances turned out to be an effective method to gain dose homogeneity whereas reduction of lateral beam position spacing did not show such an effect. Secondly, to enable systematic studies of mitigation techniques and effects of miscorrelation between motion monitoring system and tumour motion a phantom with 6D target and independent thorax motion was constructed and validated successfully in experiments. Thirdly, two motion monitoring systems by VisionRT Ltd. and Anzai Medical Co.,Ltd., respectively, were compared in terms of gating delays and correlation to tumour motion extracted from MV-fluoroscopy. While the VisionRT system showed larger delays than the Anzai system under laboratory conditions, no significant difference between the systems with respect to tumour-correlation was found in a clinical study.

Results of this work will be incorporated into patient treatments using gating that will start at HIT within the next few months. Furthermore, a phantom simulating thorax and target motion with a variety of applications such as 4D imaging is now available and already in use by several groups.

Contents

1 Motivation

Cancer is one of the most leading causes of death worldwide. According to the World Health Organisation (WHO) in 2008 7.6 million died due to it which corresponds to about 13% of all deaths [WHO]. In Germany in 2006 about 430.000 incidents and about 210.000 cancer related deaths were reported [RKI].

For about 50% of incidents radiation therapy is a helpful treatment option and has been used for many years [Schardt et al., 2010]. Within the last twenty years due to physical and biological reasons (see section 2.1) more promising techniques came up using ions instead of photons or electrons as a projectile for tumour irradiation. It turned out that ion-therapy can gain higher tumour conformity and better control rates than conventional photon therapy [Durante and Loeffler, 2010; Levin et al., 2005; Schulz-Ertner et al., 2007; Tsujii et al., 2004]. Ion-therapy has the potential to be more precise in targeting. Using ions and especially a certain dose delivery thecnique, beam scanning, the volume where the dose is applied to can be almost exactly matched to the tumour volume, which is not the case in photon therapy. This potential of higher tumour volume conformity leads to less dose in healthy tissue which is one of the goals of improving radiation therapy [Schardt et al., 2010].

As long as the target stays stationary high volume conformity can be achieved, to accomplish this goal for moving tumours is a big challenge. Statistics of cancer incidents show that tumours in moving organs (e. g. lung or liver tumours) occur quite often. Tables 1.1 and 1.2 list the ten most occurring cancer types and the ten death-causing cancer types, respectively, taken from data which was published by the International Agency for Research on Cancer (IARC) based on the year 2008. One can see that lung cancer is the most likely cancer for men. Liver and stomach cancer which are also affected by breathing are among the top five. In case of women lung cancer is also one of the more frequent cancers. In terms of mortality it is even number two.

Some different strategies have been proposed to treat moving organs using ions [Bert and Durante, 2011]. One of these strategies is to synchronize irradiation with tumour motion and to gate the irradiation in time intervals when the tumour is at a certain position (gating). This gated irradiation combines comparable high conformity with comparable low complexity (see section 2.2.4). So far, gating using a scanned ion beam has not been used clinically, but it will be the first technique being used at the Heidelberg Ion-Beam Therapy Center (HIT). Goal of this work was to answer some of the open questions (mitigation of residual motion effects and motion sensor evaluation) and to develop a phantom for dose verifications and robustness analysis to bring gating more close to clinical application at HIT.

Table 1.1.: Cancer incidents worldwide. Numbers are given for the ten most occurring cancer types for men and women in 2008. Data taken from [IARC]

men cancer	number	ASR[a]	women cancer	number	ASR[a]
Lung	1092056	34.0	Breast	1384155	39.0
Prostate	899102	28.0	Colorectum	571204	14.7
Colorectum	663904	20.4	Cervix uteri	530232	15.3
Stomach	640031	19.8	Lung	515999	13.6
Liver	523432	16.0	Stomach	348571	9.1
Oesophagus	326245	10.2	Corpus uteri	288387	8.2
Bladder	294345	9.0	Liver	226312	6.0
Non-Hodgkin lymphoma	199736	6.1	Ovary	224747	6.3
Leukaemia	195456	5.9	Thyroid	163968	4.7
Lip, oral cavity	170496	5.3	Non-Hodgkin lymphoma	156695	4.2
All cancers[b]	6617844	203.8	All cancers [b]	6044710	165.1

[a] Age standardised rate per 100.000 per year

[b] excluding non-melanoma skin cancer

Table 1.2.: Cancer mortalities worldwide. Numbers are given for the ten most cancer caused deaths for men and women in 2008. Data taken from [IARC]

men cancer	number	ASR[a]	women cancer	number	ASR[a]
Lung	948993	29.3	Breast	458503	12.5
Liver	478134	14.6	Lung	427586	11.0
Stomach	463930	14.2	Colorectum	288654	7.0
Colorectum	320397	9.7	Cervix uteri	275008	7.8
Oesophagus	276007	8.6	Stomach	273489	6.9
Prostate	258133	7.5	Liver	217592	5.7
Leukaemia	143555	4.3	Ovary	140163	3.8
Pancreas	138377	4.3	Oesophagus	130526	3.4
Bladder	112308	3.3	Pancreas	128292	3.1
Non-Hodgkin lymphoma	109484	3.3	Leukaemia	113606	3.1
All cancers[b]	4219626	128.6	All cancers[b]	3345176	87.6

[a] Age standardised rate per 100.000 per year

[b] excluding non-melanoma skin cancer

2 Foundations and purpose of this work

2.1 Particle therapy

Basic goal of radiation therapy is to apply a high dose to the tumour by sparing the normal tissue as much as possible. Conventional photon therapy has been adapted and optimized to meet this goal. An outmost precision can be obtained by crossfire techniques such as intensity modulated radiotherapy (IMRT) but on the cost of a higher integral dose to the normal tissue and longer irradiation times. Ions have properties which make them more advantageous as a projectile for radiation therapy.

2.1.1 Physical advantage

While photons loose their energy in matter due to the photoelectric effect, the Compton effect or the pair production effect (depending on the photon energy) [Knoll, 2010], ions follow different rules. For ions with therapy relevant energies the Bethe-Bloch [Bethe, 1930; Bloch, 1933a,b] formula describes very well their energy loss (or stopping power) in matter [Nakamura et al., 2010]:

$$-\frac{dE}{\rho dx}\left[\frac{\mathrm{MeV\,cm^2}}{\mathrm{g}}\right] = k_1 Z_\mathrm{P}^2 \frac{Z_\mathrm{T}}{A_\mathrm{T}} \frac{1}{\beta^2} \left[\frac{1}{2}\ln\left(\frac{k_2 \beta^2 \gamma^2 T_\mathrm{max}}{I^2}\right) - \beta^2 - \frac{\delta\left(\beta\gamma\right)}{2}\right] \tag{2.1}$$

with $k_1 = 2\pi N_\mathrm{A} r_\mathrm{e}^2 k_2$ and $k_2 = 2m_\mathrm{e}c^2$. Projectile dependency is given by its atomic number Z_P, the velocity dependent relativistic factors β and γ and the maximum kinetic energy which can be transmitted to a free electron in one single collision T_max, which depends on the projectiles mass and velocity. Target material impacts stopping power by its charge-over-mass-ratio $Z_\mathrm{T}/A_\mathrm{T}$ ($[A] = \mathrm{g/mol}$) and the ionization potential I [Barkas and Berger, 1964; Bichsel, 1992; Sternheimer, 1966]. $\delta\left(\beta\gamma\right)$ is a density correction [Sternheimer, 1952; Sternheimer and Peieris, 1971; Sternheimer et al., 1984] valid for higher energies. Basically, for a given projectile and material, the stopping power is only a function of β.

Initial projectile energies relevant for particle therapy are up to about 430 MeV/u (carbon ions) and 230 MeV (protons), respectively ($\beta\gamma \leq 1$). In figure 2.1 for protons and carbon ions the in radiotherapy more frequently used linear energy transfer (LET) is plotted over a certain range of particle energy. The LET is the energy loss not normalized to the target density:

$$\mathrm{LET}_{\infty} = \frac{dE}{dx} \left[\frac{\mathrm{keV}}{\mu\mathrm{m}}\right] \tag{2.2}$$

While for protons the maximum is at about 0.08 MeV/u the maximum in the carbon curve appears at about 0.35 MeV/u. The y-axis, of course, strongly depends on the projectile (Z_P^2-dependency) which can also clearly be seen in figure 2.1.

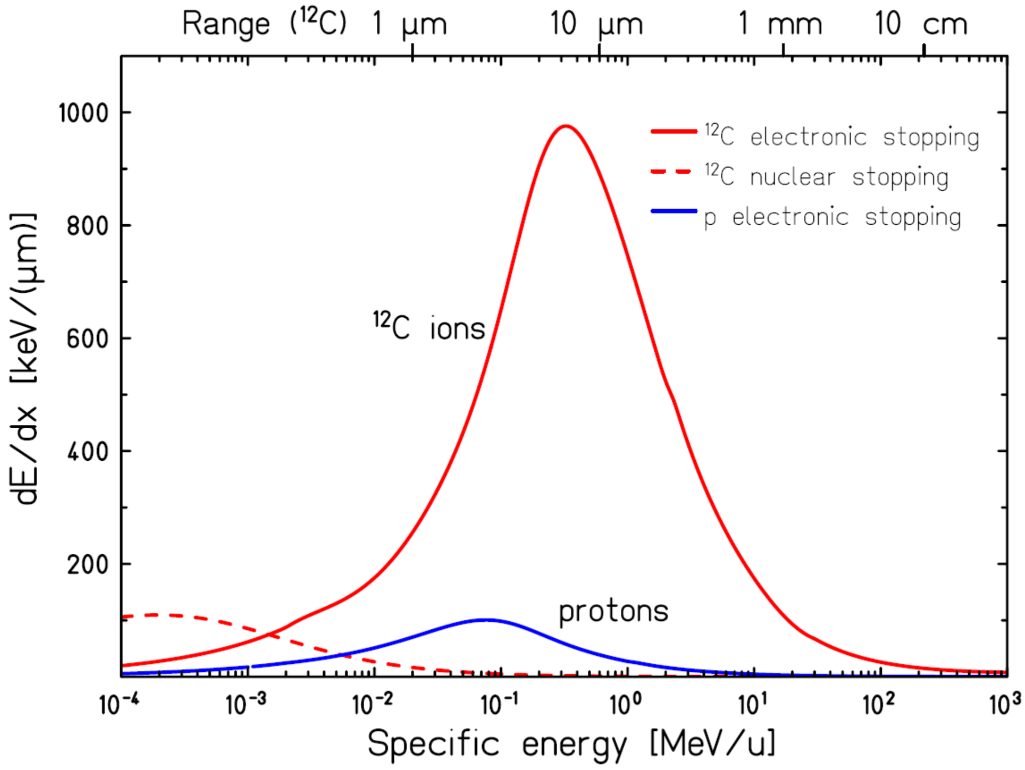

Figure 2.1.: Specific energy loss of carbon ions and protons in water for a therapy relevant energy range. Nuclear stopping power is indicated for carbon by the dashed line. In addition, at the top carbon ranges are given [Schardt et al., 2010]. The maximum appears at higher energies for carbon ions than for protons. In addition, the absolute values of the carbon curve are higher due to the Z_P^2-dependency.

If, for instance, a carbon ion with therapeutic initial energy gets slower it first follows the $1/v^2$ dominated region of equation 2.1: while velocity decreases stopping power increases. Once energy gets below some few MeV/u the ion starts to collect electrons. This leads to a decreased effective charge given by the Barkas formula [Barkas, 1963]

$$Z_{\mathrm{P,\,eff}} = Z_\mathrm{P}\left(1 - \exp\left(-125\beta Z_\mathrm{P}^{-\frac{2}{3}}\right)\right) \tag{2.3}$$

which leads to a decrease of stopping power due to the $Z^2_{\mathrm{P,\,eff}}$-dependency.

In addition, for low energies corrections added as summands within the square brackets of equation 2.1 get important, namely shell corrections [Barkas and Berger, 1964], the Bloch correction [ICRU, 1993a] and the Barkas correction [Barkas et al., 1956; Lindhard, 1976].

Electric stopping power below the Bethe-Bloch area was described by [Lindhard et al., 1963] (behaviour linear to β). This is the region where the particles approximately have the velocity of the electrons in the target. The maximum in between (compare figure 2.1) is fitted [Andersen and Ziegler, 1977].

Finally, for very low energies non-ionizing nuclear recoil energy loss starts to dominate the stopping power (indicated by the dashed line in figure 2.1) [ICRU, 1993a; Lindhard et al., 1963; Ziegler et al., 1985].

This behaviour of first increasing and, at the last few µm, decreasing dE/dx leads to a depth-dose distribution with a sharp peak (Bragg-peak). The dose (or absorbed dose) is defined as the energy absorbed per unit mass

$$D\,[\mathrm{Gy}] = \frac{\Delta E}{m}\left[\frac{\mathrm{J}}{\mathrm{kg}}\right] \tag{2.4}$$

and, thus, proportional to the energy loss and the particle fluence:

$$D\,[\mathrm{Gy}] = 1\cdot 10^9 e \frac{dE}{\rho dx}\left[\frac{\mathrm{MeV\,cm^2}}{\mathrm{g}}\right] F \left[\frac{1}{\mathrm{cm^2}}\right] \tag{2.5}$$

In figure 2.2 depth-dose distributions for two carbon ion energies and two photon energies are compared. Photon doses show a smooth maximum in little depths (build-up due to forward scattering of the Compton electrons). After that dose decreases exponentially. Due to the above discussed aspects carbon shows a sharp Bragg-peak. For both radiation types the position of the maximum can be shifted to higher depths by increasing initial energy. 25 MV is already the order of maximum available photon energies for therapy (in the Heidelberg clinic typically 6 MV beams are used). 270 MeV/u is, however, even a low energy for a synchrotron accelerated carbon beam. While, therefore, the position of the photon dose maximum is limited to a depth of a few cm a Bragg-peak can easily reach higher depths. Thus, the advantage for treating deep seated tumours is obvious. In addition, the sharp peak for ion irradiation promises low dose deposition in normal tissue.

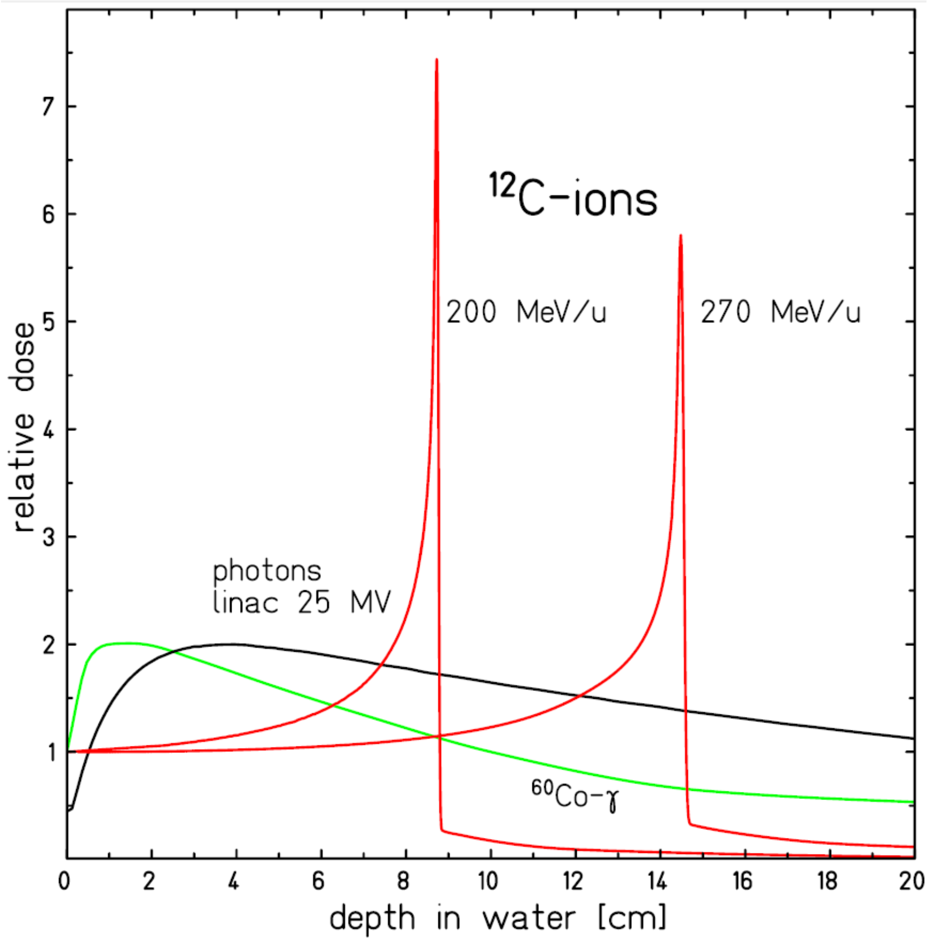

Figure 2.2.: Depth-dose distributions of ^{12}C ($200\,\mathrm{MeV/u}$ and $270\,\mathrm{MeV/u}$), LINAC photons ($25\,\mathrm{MV}$) and ^{60}Co photons ($1.173\,\mathrm{MeV}$ and $1.332\,\mathrm{MeV}$ [BNL]) [Schardt et al., 2010]. The dose maximum moves shifted to higher depth for increasing energy. While ions show a sharp peak (Bragg-peak) in large depths, photon dose shows a maximum in little depth and decreases exponentially.

2.1.2 Biological advantage

Besides the physical differences discussed above there can be biological differences in terms of dose response dependent on the irradiation type.

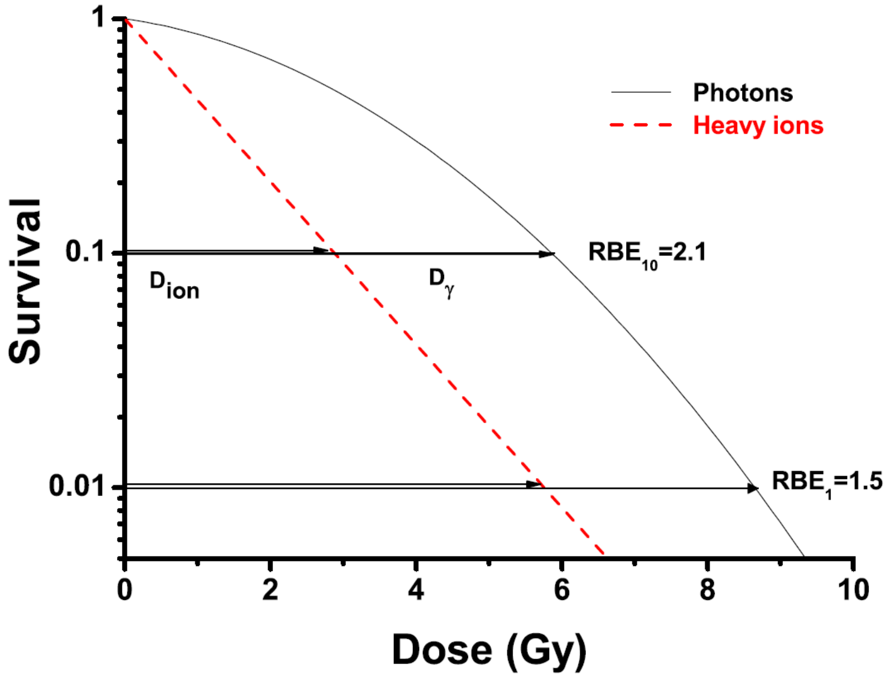

Figure 2.3.: Sketch of survival curves for photons and carbon ions. Carbon ions show a much steeper decrease of survival with dose, thus, they are more effective. The relative biological effectiveness (RBE) is indicated for 10% and 1% survival and differs for these two levels [Schardt et al., 2010].

Figure 2.3 shows a potential behaviour of a cell response curve with respect to cell survival. Sketched is the cell survival over dose (survival curve) for a photon and a carbon beam which can be parameterized using a linear-quadratic model [Hall and Giaccia, 2011]:

$$S = e^{-\alpha D - \beta D^2} \tag{2.6}$$

The sketch indicates that for a given survival fraction less dose is needed for carbons compared to photons. Thus, for the same dose the biological effect of carbon is higher than for photons. This enhancement in biological effect is quantified using the so called relative biological effectiveness (RBE), which is defined as follows [Hall and Giaccia, 2011]:

$$\mathrm{RBE} = \frac{D_{\mathrm{Photons}}}{D_{\mathrm{Test}}} \tag{2.7}$$

Thus, the RBE is the ratio of the dose needed by a certain test radiation relative to photon dose leading to the same biological effect. In our case the test radiation would be carbon ion irradiation.

Due to the low LET of protons RBE for proton irradiation is usually assumed to be 1.1 [Paganetti, 2003; Paganetti et al., 2002]. For heavy ions, because of the large variation of LET, it is a more complex situation. RBE depends on several quantities: the biological endpoint (effect), dose, LET, particle type, and tissue sensitivity [Belli et al., 1998; Furusawa et al., 2000; Schardt et al., 2010; Suzuki et al., 2000; Weyrather et al., 1999]. Due to this complexity the RBE is calculated based on a model whereat two different approaches were developed by [Scholz and Kraft, 1996] at GSI and [Kanai et al., 1999] at National Institute of Radiological Sciences (NIRS), respectively.

An explanation why high-LET radiation can lead to higher biological effects than low-LET radiation is the track structure: for low-LET radiation a single particle can only transfer a low amount of energy. Therefore, for photon irradiation lots of photons are needed to deposit the same dose as a few carbon ions would deposit. This results in higher local effects for carbon ions while for photons dose is more or less equally distributed. Figure 2.4 illustrates this effect: a simulated local dose distribution is shown in an area of the typical size of a cell nucleus for photon and carbon irradiation of different specific energies. The average dose is in all cases normalized to 2 Gy. One can see that for photons dose is homogeneous while carbon ions show discrete peaks at single particle tracks. The local doses can be extremely high. The number of tracks increases with energy, because the energy loss decreases and, thus, fluence has to be increased to gain the same dose (compare equation 2.5).

Using high-LET irradiation the probability to hit the sensitive volume of a cell, the cell nucleus, is smaller then using a low-LET irradiation due to the different fluence. But if the high-LET particle hits the cell nucleus the local dose deposit to a certain part of the nucleus will be much higher then for low-LET irradiation. Thus, there is the potential to have a higher biological effect for the same deposit dose.

2.1.3 Treatment planning

To be able to make use of the advantages mentioned above first of all the target has to be identified. Target definition is done based on a computed tomography (CT). Following [ICRU, 1993b] several volumes are defined: the gross tumour volume (GTV), the clinical target volume (CTV) and the planning target volume (PTV). The GTV comprises the macroscopic visible tumour. The CTV includes besides the GTV all tissue which has, in addition, to be treated. Thus, the CTV is the volume where the prescribed dose has to be delivered to. To achieve this an additional margin is added leading to the PTV. This volume comprises the CTV and accounts for any

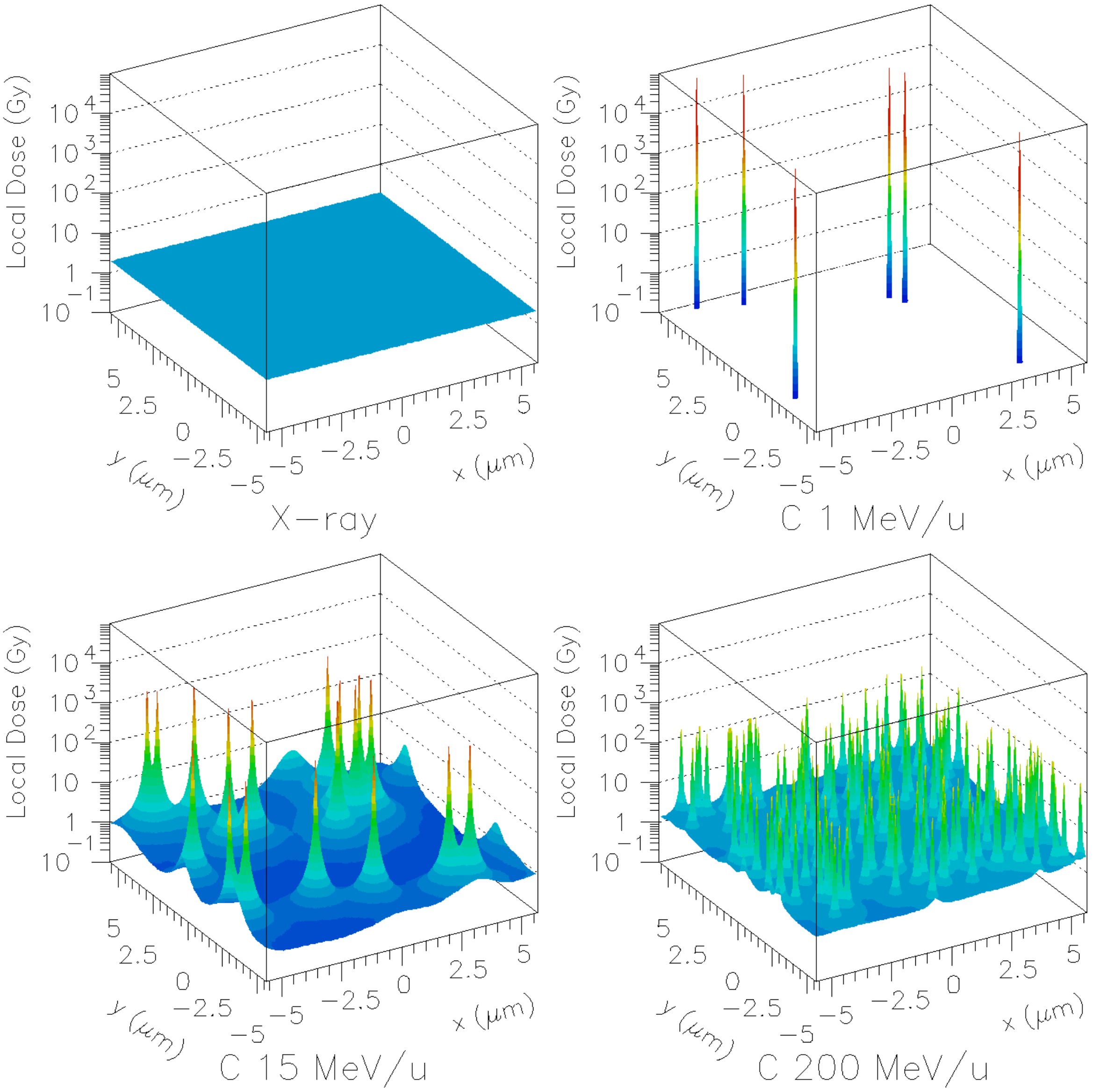

X−ray

C 1 MeV/u

C 15 MeV/u

C 200 MeV/u

Figure 2.4.: Microscopic dose distribution for photons and carbon ions with different specific energies. Photon dose is homogeneous while carbon dose is locally very high. Fluence increases with energy due to decreasing LET. Also the maximum local doses decrease with increasing energy [Scholz, 2003]

uncertainty arising from patient setup and beam delivery. To ensure that the CTV is treated sufficiently the beam has to be delivered in a way that the entire PTV is covered with the prescribed dose (PD) (according to [ICRU, 1993b] 100 % of the PTV have to be covered with 95 % to 107 % of the PD). Based on the CT using the contoured volumes an appropriate treatment planning system (TPS) optimizes beam parameter in a way that delivery of the resulting plan leads to the planned dose distribution.

2.1.4 Beam delivery methods

The PD is usually delivered distributed over several days (so called fractions) due to benefits in respect of repair mechanisms [Hall and Giaccia, 2011]. Furthermore, in each fraction typically more then one beam incidence angle (so called field) is used to increase the ratio between target dose and dose in normal tissue. The beam angle relative to the patient can be changed by rotating the patient couch or rotating the beam by means of a gantry. Pictures of a photon and ion gantry are shown in figure 2.5.

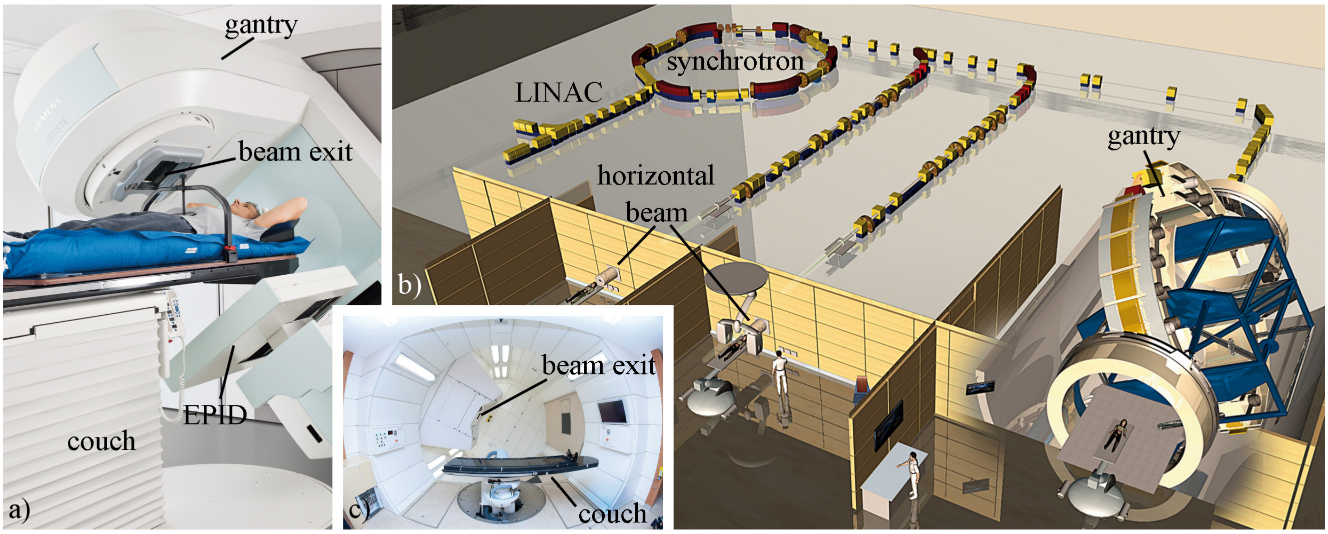

Figure 2.5.: Pictures of a photon and an ion gantry. **(a)** Picture of the Siemens Artiste photon linear accelerator [Siemens]. The whole accelerator (and, thus, the beam) can be rotated around the patient. Opposite to the beam exit an electronic portal imaging device (EPID) can measure the beam exiting at the back side of the patient. **(b)** Beam line of the Heidelberg Ion-Therapy Center (HIT) [HIT]. Patients can be treated in two rooms with a horizontal beam and one room where the beam can be rotated around the patient using the first heavy-ion gantry. **(c)** Picture of the gantry treatment room. [HIT]

High-energetic photons (6 MV to 24 MV) are usually produced by an electron accelerator where the electrons are stopped in a target. The resulting bremsstrahlung is then laterally shaped using collimators to adapt it to the beam's eye view (BEV) projection of the PTV. Due to the disadvantageous depth-dose distribution of photons usually 4-7 fields (different gantry angles) are delivered within one fraction to reduce dose in healthy tissue. Behind the patient exiting photons can be measured using an electronic portal imaging device (EPID) which enables acquisition of MV-fluoroscopy (see also figure 2.5(a)).

Cyclotrons and synchrotrons, the accelerator types commonly used for production of ion beams in therapy so far, are primarily providing a pencil beam of ions. Thus, the beam delivery system has to shape this pencil beam in a way that it deposits dose to the planned volume. An overview of all potential methods is given in literature [Chu et al., 1993]. The two extreme forms, the fully passive system (beam scattering system) [Chu et al., 1993] and the fully active system [Haberer et al., 1993; Pedroni et al., 1995], are explained in the following.

A sketch of a fully passive system is shown in figure 2.6(a). A monoenergetic beam is first scattered to widen it to the maximum lateral necessary size. After that a range modulator converts the monoenergetic beam to a beam with a certain spread of energies. Since particle energy corresponds to particle range at this stage a certain range area can be covered by the so called spread out Bragg-peak (SOBP). A range shifter then shifts this SOBP to the depth necessary to cover the tumour. From this point patient specific modulations have to be done: A collimator ensures that the lateral shape of the beam is formed as the lateral shape of the PTV in BEV and, finally, a patient specific compensator creates the distal dose cut-off.

Fully active systems use ion optics and the accelerator itself to spread the dose over the target volume. In planning stage the target is divided in small sub volumes: first it is segmented into a certain number of slices where each slice corresponds to the range of particles of certain energy (iso-energy slice (IES)). Each IES is then covered with a grid of desired beam spot positions (beam position grid). During beam application particles are delivered to a certain IES by selecting the corresponding initial beam energy. Then by using two dipole magnets oriented perpendicular to each other the beam is swept over the IES by aiming one beam spot position after another. Lateral beam shaping using dipole magnets is also called scanning (raster scanning [Haberer et al., 1993] or spot scanning [Pedroni et al., 1995]). While some scanning systems (e. g. at GSI) are fully active systems, for instance at Paul Scherrer Institut (PSI) (Switzerland) energy variation is passively done since there a cyclotron is used. In figure 2.6(b) a sketch of a fully active system is given.

While in a scattering system using an appropriate range modulator the target dose distribution is intrinsically homogeneous, for a active system two conditions have to be matched: the lateral overlap factor (laOF) and the longitudinal overlap factor (loOF) of the beam spots have to be sufficient. The lateral overlap is defined as follows:

$$\mathrm{laOF} = \frac{\mathrm{FWHM}_{Beam}}{\Delta s} \tag{2.8}$$

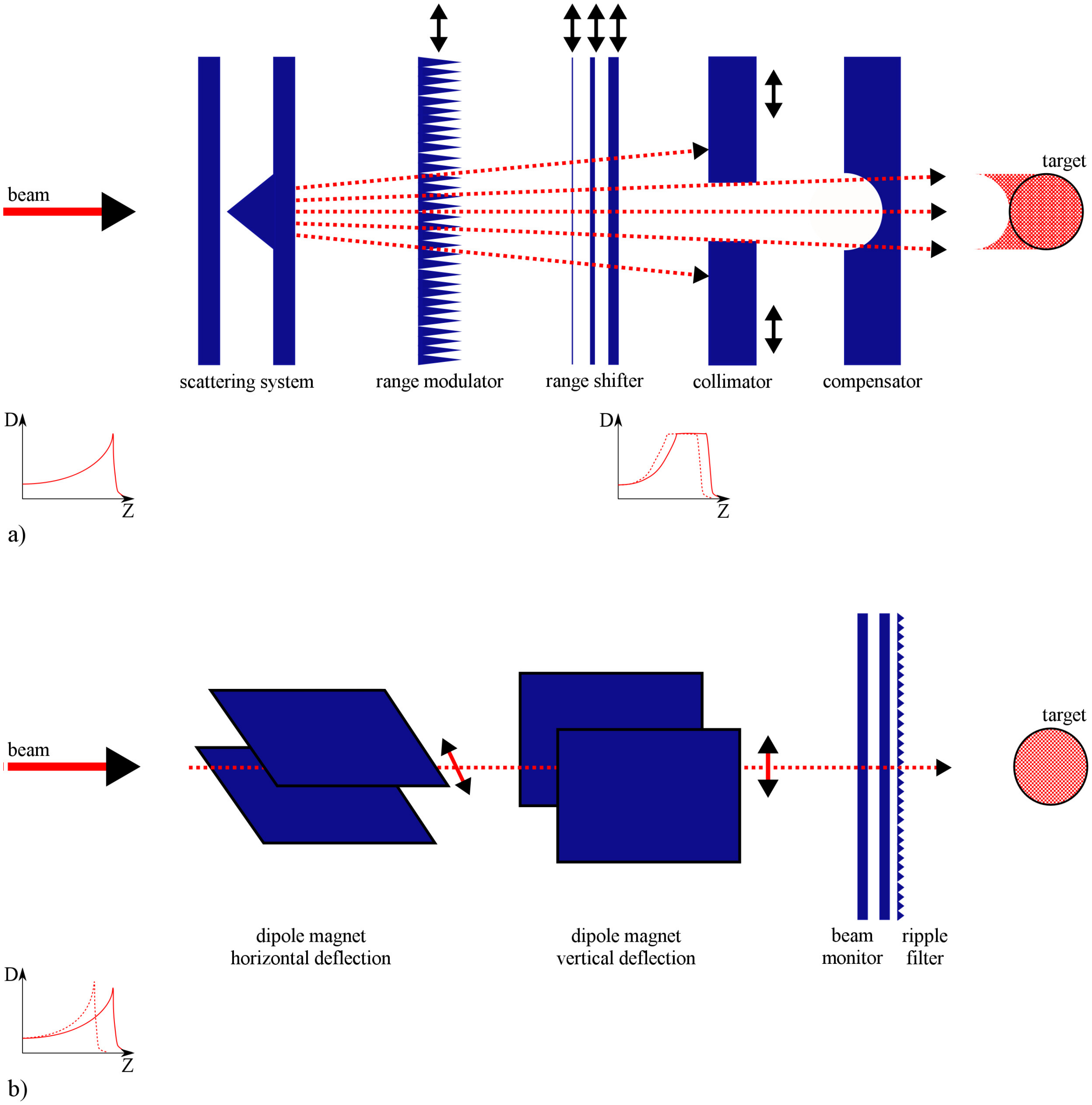

Figure 2.6.: **(a)** Sketch of a passive beam delivery system (beam scattering). The scattering system combined with the collimator shape the beam laterally to the target dimensions. The range modulator, range shifter and compensator create an energy mix resulting in a spread-out Bragg-peak (SOBP) covering the target. The proximal edge can not be adapted to the target dimensions (indicated by the read area representing the target dose area). **(b)** Sketch of an active beam delivery system (beam scanning). The Bragg-peak is directed to each raster position within the target. Range is controlled by the initial beam energy and lateral positioning is done by two deflection magnets which are oriented perpendicular to each other. Target dose area (read area) can nicely shaped to the target dimensions.

where FWHM is the full width at half maximum of the beam spot and Δs is the lateral spacing of the beam position grid.

On the right hand side of figure 2.6(b) it is indicated that also in such a system some passive devices are needed. To gain a sufficient overlap of the Bragg-peaks a ripple filter (RiFi) is used. A RiFi widens the Bragg-peak to a width of some mm. The longitudinal overlap is given by the Bragg-peak width resulting from the used RiFi [Weber and Kraft, 1999] and the used IES spacing Δz:

$$\mathrm{loOF} = \frac{d_{RiFi}}{\Delta z} \tag{2.9}$$

Studies for stationary targets have been done by [Haberer et al., 1993; Weber, 1996]: Sufficient dose distributions can be reached with laOF= 3 and loOF= 1 [Kraemer et al., 2000]. At GSI a RiFi adjusted for 3 mm IES spacing is used.

An advantage of a fully active system is the much less material in the beam line. In a passive system lots of the incident particles are absorbed by the beam shaping devices introducing secondary irradiation (especially neutrons [Binns and Hough, 1997; Yan et al., 2002]). For particles heavier than protons fragmentation of the primary beam is also an issue. But in an active system fragmentation can also be present due to nuclear interactions within the patient (Fragments in the beam are the reason for the dose tail behind the Bragg-peak in figure 2.2). In addition, the proximal dose gradient can not be shaped with passive devices leading to worse volume conformity of scattering systems compared to the scanning technique (compare figure 2.6 on the right hand side).

Besides the different beam purity and conformity dose delivery timing is different which has implications on the irradiation of moving targets: while dose in the passive case is applied to the whole target volume at one time in the active system it is built up spot by spot. The consequences will be discussed in section 2.2. It has to be noted that some facilities are able to scan much faster than it is possible at GSI [Furukawa et al., 2010b; Pedroni et al., 2004; Zenklusen et al., 2010] which may reduce influences of target motion on the resulting dose distribution.

2.1.5 Status

At the moment 34 sites using ions for cancer treatment are in clinical operation ([PTCOG]). Three of them use beam scanning (HIT, Heidelberg, Germany [Haberer et al., 2004]; PSI, Villigen, Switzerland [Pedroni et al., 1995, 2004]; Rinecker Proton Therapy Center (RPTC), Munich, Germany) and two sites both techniques (MD Anderson Cancer Center (MDACC), Houston, USA [Smith et al., 2009]; NIRS, Chiba, Japan). All the others use the passive beam delivery technique, so far. 24 new facilities are currently under construction or in planning stage. Minimum 5 of them will have scanned beam application (for some this information is not available).

Till end of 2010 78275 patients were treated using ions, most of them with protons (67097) [PTCOG]. So far, moving organs were only treated with ions in facilities using a passive beam delivery system [Schardt et al., 2010]. The reason for that will be discussed in the next sections.

2.2 Treatment of moving tumours

2.2.1 Causes of tumour motion

Tumour motion can be classified into three types [Bert and Durante, 2011]:

i) patient motion

ii) motion in-between two fractions (inter-fractional motion)

iii) motion within one fraction (intra-fractional motion)

Motion of the patient itself (i) is compensated by immobilization of the patient. For instance in brain-tumour treatments using ions usually by means of a mask the head is fixed to the treatment couch. Inter-fractional motion (ii) can occur e. g. in prostate cancer. Prostate position may change from day to day due to altering filling of bladder and rectum [Chandra et al., 2003; Langen and Jones, 2001]. Both motion causes are linked to a time scale of some minutes to hours and, therefore, can be compensated during patient setup as long as treatment time is short. If the time-scale of the motion is shorter or comparable to the treatment time it is called intra-fractional motion (iii). Intra-fractional motion is mainly caused by respiration which affects tumours situated in the thorax or abdomen. For example, for lung tumours motion amplitudes of up to 25 mm were observed while the main motion direction was found to be the superior-inferior (SI)-direction (motion along the head-feet-axis) [Britton et al., 2007; Koch et al., 2004; Liu et al., 2004; Neicu et al., 2003; Seppenwoolde et al., 2002; Sonke et al., 2008]. Furthermore, e. g. for liver tumours drifts of the centre of motion (base-line drifts) of up to 6.3 mm have been observed [von M. Siebenthal et al., 2007a,b].

Since this work is focused on a technique which mitigates intra-fractional motion all the following refers to that type of tumour motion.

2.2.2 Implications of tumour motion

First implication is obvious: a moving target can leave the PTV if motion is not taken into account in planning stage. This geometrically displacement can lead to severe under dosage of the CTV. Therefore, motion amount has to be estimated and incorporated into treatment planning which will be briefly discussed in section 2.2.3.

The second effect of motion is correlated to the dependency of the depth-dose distribution on the initial energy. During respiration e. g. the position of ribs change which leads to altering composition of the material within the entrance channel. Bones reduce beam energy much more than inter-rib tissue. Thus, the energy of the beam changes during motion which affects the range in case of particle irradiation (compare figure 2.2). If particle energy drops too much it can effect in under dosage of parts of the tumour since in some motion states range does not suffice to cover the whole PTV. Figure 2.7 shows as an example range changes due to respiratory motion for a lung cancer patient. The iso-range lines differ a lot between the two shown breathing phases (maximum inhale and maximum exhale).

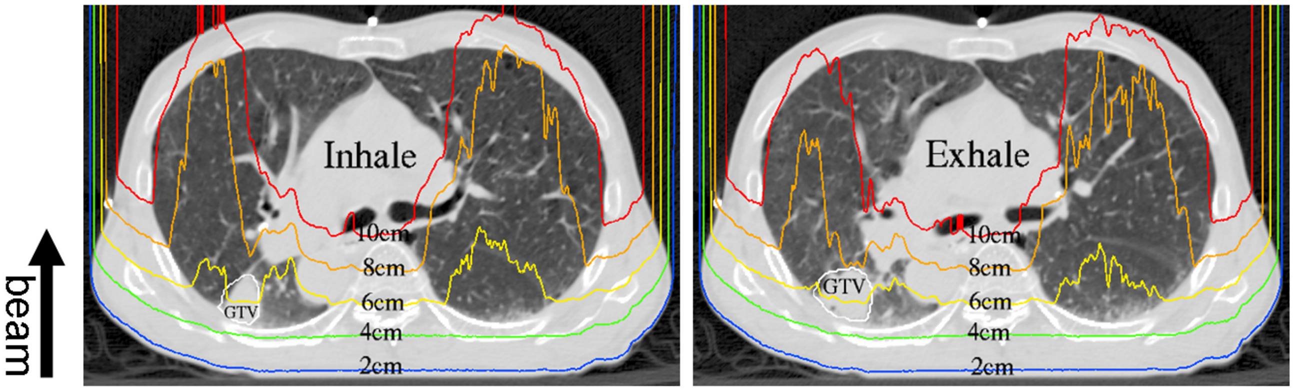

Figure 2.7.: Range Changes due to respiratory motion. For two breathing phases (maximum inhale and maximum exhale) iso-range lines for ranges of 2 cm to 10 cm are displayed. [Bert and Durante, 2011]

The third implication occurs in case of particles only for active beam delivery and results from the time dependency of the beam delivery system: the target is scanned point by point and slice by slice. If the target moves the effective raster point position relative to the target will change during irradiating a certain raster point. The beam spot motion interferes with the target motion and this causes inhomogeneous dose distributions which may be unacceptable in clinical situations.

Figure 2.8 shows as an example the result of a film irradiation using a scanned carbon beam for a stationary and a moving case. In both cases the aim was to irradiate vertical stripes which well worked in the stationary case in figure 2.8(a). In figure 2.8(b) only target motion was switched on resulting in a strange blackening pattern due to the interference of target and beam motion. This behaviour is also called interplay effect. Severe under and over dosage can be the result [Bert et al., 2008; Groezinger et al., 2006; Lambert et al., 2005; Phillips et al., 1992] which is, by the way, also true for IMRT [Bortfeld et al., 2002; Chui et al., 2003], the most modern photon therapy.

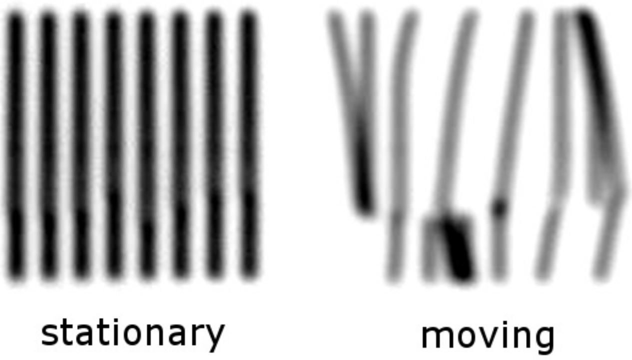

Figure 2.8.: Irradiation of a stationary and a moving film with the same plan aiming for vertical stripes [Groezinger, 2004].

2.2.3 Tumour motion and treatment planning

To evaluate the motion amount first of all a time resolved computed tomography (4DCT) is acquired [Rietzel et al., 2005]. Based on the CTV contoured in several breathing phases an additional volume is defined which is the geometrical union of the CTVs in all motion states: the internal target volume (ITV) [ICRU, 1999]. A margin accounting for setup and beam delivery uncertainties is then added to the ITV resulting in the PTV.

For some beam delivery techniques the ITV not necessarily has to incorporate the whole target motion. This is the case if the irradiation is only applied during a fraction of motion states (gating) or if the beam follows the target (beam tracking). This will be more detailed discussed in the following section.

Otherwise, in case of particles a pure geometrical union of the CTVs may not be enough due to the range changes presented above [Rietzel and Bert, 2010].

So far, based on the resulting PTV the TPS then optimizes the plan as it would be done in a stationary case [Bert and Durante, 2011]. In photon therapy ideas of incorporating full 4D information into the plan optimization have been published [Nohadani et al., 2010].

2.2.4 Tumour motion and beam delivery

In conventional photon therapy and in ion therapy using the passive beam delivery technique increase of the PTV can be a solution. If the target, the CTV, in any motion state keeps within the PTV (and in case of particles range changes are incorporated into the ITV) acceptable target dose can be achieved. However, dose to normal tissue is highly increased.

In contrast for scanned particle beams increase of the PTV only does not work due to the interplay effect. Thus, more complex efforts have to be done to mitigate effects of target motion in scanned particle therapy.

The simplest approach of the three motion effect mitigation techniques is called rescanning or repainting [Phillips et al., 1992]. The beam is scanned over the PTV n times by delivering $1/n$ of the prescribed dose in each scan. There are several flavours of this technique under investigation [Furukawa et al., 2007, 2010a; Seco et al., 2009], but the basic principle is always the same: In each scan a certain interplay pattern is generated. The n resulting interplay patterns can look all different, which depends on timing issues (synchronization between beam delivery timing and breathing period [Furukawa et al., 2010a]). Thus, it is possible that these n interplay patterns of all n scans at the end sum up to a homogeneous dose distribution.

The most complex mitigation technique is beam tracking [Groezinger et al., 2004]. The aim of beam tracking is to follow the target with the beam and irradiate it as if it would be a stationary target. Target position is tracked online and fed into the treatment control system (TCS) in real-time. The TCS then calculates offsets in all three dimensions and adjusts the beam laterally by changing the scanner magnet settings and longitudinally e. g. by a fast wedge system [Bert et al., 2007; Chaudhri et al., 2010; Groezinger et al., 2004]. Such a wedge can decrease or increase the beam energy slightly by putting more or less absorber material in the beam resulting in different Bragg-peak positions. Beam tracking would gain healthy tissue sparing since as less healthy tissue is irradiated as it would be in stationary irradiation. The problem with this technique is the high complexity especially in respect of determining the current target position in real-time.

Less complexity than beam tracking and less healthy tissue irradiation than for rescanning is combined in the third approach: gating [Minohara et al., 2000]. The basic idea is to irradiate the target almost like a stationary one and switch off the beam when the target leaves the target volume.

Figure 2.9 illustrates the principle: The target motion is tracked using an appropriate motion monitoring system resulting in a motion signal of the target (top row). On this trajectory a certain window, the gating window (GW), is defined. The target has to be within the target volume during that GW. The gating control system which is usually incorporated into the motion monitoring system generates a gate request signal (second row) which is high while target motion is within the GW. If the synchrotron has beam available (third row) beam will be extracted (fourth row). In case of using a cyclotron this last condition is missing since beam can be extracted during all gating windows.

Rescanning is the most simple of the three techniques. In most flavours no motion monitoring system is needed. Treatment planning is relating to workflow like for a stationary target, only the PTV is increased in a way that all motion states of the CTV are comprised. But this simplicity is also the disadvantage of this method: the increased target volume implies irradiation of healthy tissue. In addition that all n interplay patterns sum up to a homogeneous dose distribution is not guaranteed. Bad timing combinations can lead to severe interplay patterns also using rescanning [Furukawa et al., 2010a].

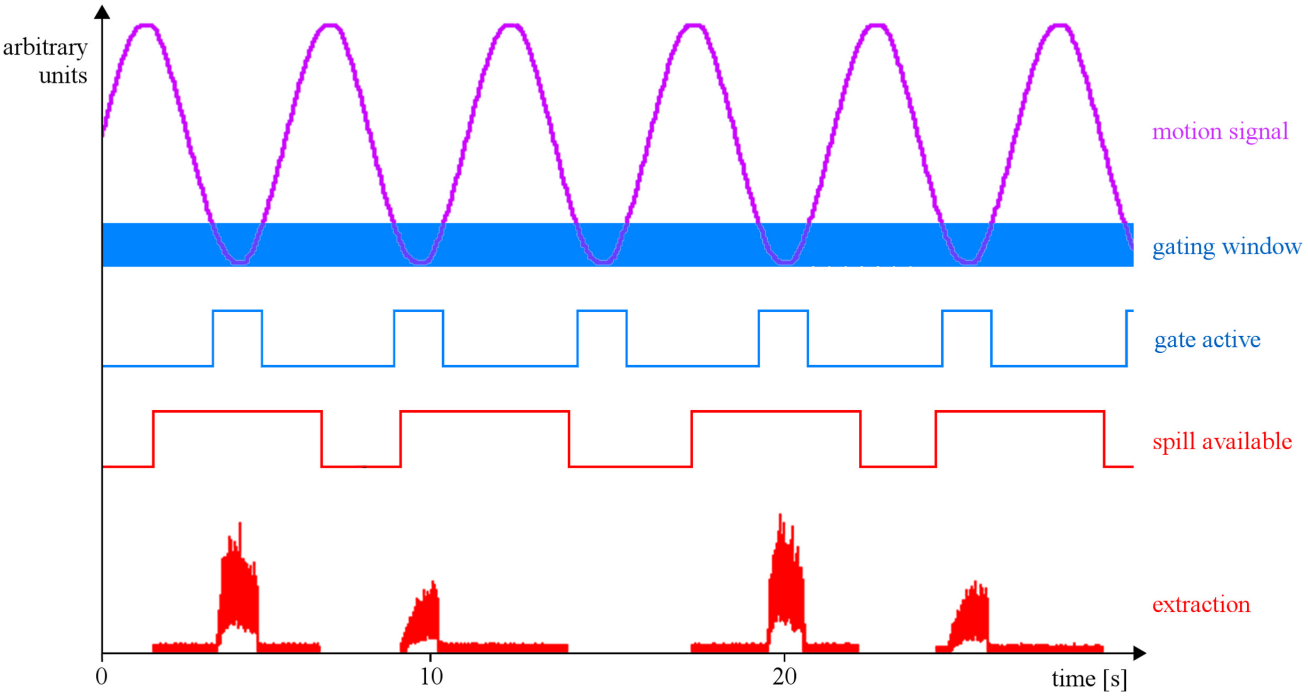

Figure 2.9.: Sketch of the gating principle: based on a target motion trajectory a gating window (GW) is defined (first row). Based on that GW a gate signal is generated (second row) by the gate controller (usually incorporated into the motion monitoring system). Beam is actually extracted when the gate signal is high and beam is available (fourth row). In case of a synchrotron beam is not continuously available (third row) in contrast to a cyclotron.

Beam tracking represents the other edge of the spectrum. It is the most complex technique. A very precise motion monitoring system is essential, because tracking of a target needs exact knowledge of its position. In addition a 4D treatment planning is necessary. And, at least for the only implemented pencil beam tracking system [Bert et al., 2007; Chaudhri et al., 2010; Groezinger et al., 2004], passive systems, the energy degrader, enter the beam line. Due to the high complexity and lots of open questions e. g. concerning target motion tracking, beam tracking might be a technique to aim for in long term perspective, but it is not likely to get it in clinical operation within the next years.

That is different for the last technique: gating. As for beam tracking (and for some rescanning flavours [Furukawa et al., 2007, 2010a; Seco et al., 2009]) a motion monitoring system is needed. But the requirements to such a system are less [Rietzel and Bert, 2010]: In contrast to beam tracking for gating it only has to ensure that the tumour is within the PTV when the beam is switched on. Normal 3D treatment planning is used typically on the end-exhale phase of the 4DCT. In addition, a smaller PTV compared to rescanning can be used. It has only to have the size corresponding to the GW which leads to sparing of healthy tissue.

But there are some issues which have to be considered before using gating with a scanned particle beam clinically: Effective motion within irradiation is reduced by irradiating only within a certain gating window. Thus, motion effects are reduced, but not vanished. Appropriate techniques to mitigate effects of residual motion have to be established, which may be less complicated then mitigating effects of larger motion [Bert et al., 2010]. In addition an appropriate motion monitoring system is needed. To ensure target position within a certain window, correlation of external (motion monitoring system) and internal (tumour) motion, but also timing issues (probable delays) play a role. For systematic studies of the effects of miss-correlation on dose results an appropriate phantom can be very helpful. In addition, for clinical application investigation of available commercial motion monitoring systems is needed to find an appropriate system.

2.3 Purpose of this work

There are more open questions which have to be answered prior to clinical operation of gating using a scanned particle beam than the three issues mentioned above (e. g. matching of actual tumour motion at treatment day compared to motion gathered from the 4DCT some days earlier). But the purpose of this work is to focus on these three tasks: motion effect mitigation of residual motion within the GW, development and test of a motion phantom and evaluation of two motion monitoring systems available at HIT.

A detailed introduction into residual motion effect mitigation as well as the results of the performed 3D-motion experiments and gating simulations are presented in chapter 3. In chapter 4 the built motion phantom is described including results of the validation experiments. Finally, in chapter 5 a comparison study of the two at HIT available motion monitoring systems, the VisionRT system (AlignRT®/GateRT®– VisionRT Ltd., London, UK) and the Anzai system (RGS AZ-733V – Anzai Medical Co.,Ltd, Tokyo, Japan) is presented.

3 A beam parameter study for mitigation of residual motion effects

3.1 Introduction

Gating has been successfully used in radiation therapy for many years [Berson et al., 2004; Lu et al., 2007; Minohara et al., 2000], but, so far, only with photons or passively delivered ions. Gating helps reducing the amount of target motion, but, thereby, the treatment time is increased by a factor of 2 to 5 [Li et al., 2005; Tsunashima et al., 2008]. Thus, a gating window (GW) on the one hand has to be as small as possible to reduce motion as much as possible. But on the other hand the treatment should be doable within reasonable time which limits the GW to a minimum size. This minimum size results in a residual motion of the target within the GW.

As described earlier residual motion can be handled using passive beam delivery system by increasing the PTV comprising an ITV to cover all motion states. In case of scanned particle therapy this may be not enough since the interplay effect can lead to inhomogeneities due to residual motion.

[Bert et al., 2009] showed a possibility of mitigating residual motion effects: increased overlap. As mentioned in section 2.1.4 for stationary targets a lateral overlap factor (laOF) of 3 and a longitudinal overlap factor (loOF) of 1 ensures homogeneous dose distributions. If the target does not move the actually hit beam spot positions are as distant as they were planned resulting in a sufficient overlap of the single beam spots. If motion comes into play two neighbouring beam spot positions relative to the targets coordinate system may have more or less the distance as planned depending on the actual motion during their irradiation. This leads to a higher or lower dose at this target region.

To increase the overlap two approaches are possible (compare section 2.1.4):

i) reduction of the lateral grid spacing Δs and the iso-energy slice (IES) distance Δz, respectively

ii) increase of beam focus and Bragg-peak width, respectively

Lateral and longitudinal grid spacing can be adapted as input parameters for the treatment plan optimization. The beam focus can be changed using ion-optical systems within the beam line and the width of the Bragg-peak is adjustable with application of a ripple filter (RiFi) [Weber and Kraft, 1999].

The experimental validation of [Bert et al., 2009] was based on film irradiations and a one dimensional target motion. Longitudinal changes were introduced using a double wedge system which is part of the beam tracking system at GSI [Saito et al., 2009].

To get from this basic proof of principle to an applicable knowledge about appropriate beam parameters for a certain patient with a certain tumour motion, as an intermediate step more complex beam parameter experiments were needed including detectors capable for dosimetric evaluations. Furthermore, results of this study should be incorporated into the preparation of gated patient treatments at HIT.

Thus, for a large variation of beam parameters gating experiments were performed at HIT. Measured doses were reconstructed and interpolated by simulations. The experimental setup, the data consistency analysis, experimental results and simulations are presented in the following sections.

3.2 Material and methods

3.2.1 Experimental setup

Experiments were performed at the quality assurance cave (QA-cave) at HIT. In several beam times main data acquisition was prepared. The actual dosimetric beam parameter study was performed in two successive nights whereas at the day in-between the QA-cave needed to be cleared due to accelerator experiments at daytime. Therefore setup had to be repositioned each evening.

Figure 3.1 shows the experimental setup. Experiments were performed using a water phantom (MP3 water phantom – PTW, Freiburg, Germany) in which an array of 24 pinpoint ionization chambers (PTW PinPoint® model 30009/30015 – PTW, Freiburg, Germany) was placed. Such a pinpoint array typically is used for plan verification in heavy ion therapy [Karger et al., 1999]. Instead of placing the pinpoint array stationary at a certain position within the water phantom it was moved using a robotic arm which motion implementation will be further described in chapter 4.

The target was moved following a three-dimensional sinusoidal trajectory

$$\begin{aligned} x(t) &= \frac{1}{2} \cdot A_{\mathrm{P}} \cdot \sin\left(\frac{2\pi}{T} t\right) - \frac{1}{2} \cdot A_{\mathrm{P}} \\ y(t) &= \frac{1}{4} \cdot A_{\mathrm{P}} \cdot \sin\left(\frac{2\pi}{T} t + \frac{\pi}{2}\right) \\ z(t) &= \frac{1}{4} \cdot A_{\mathrm{P}} \cdot \sin\left(\frac{2\pi}{T} t + \frac{\pi}{2}\right) \end{aligned} \tag{3.1}$$

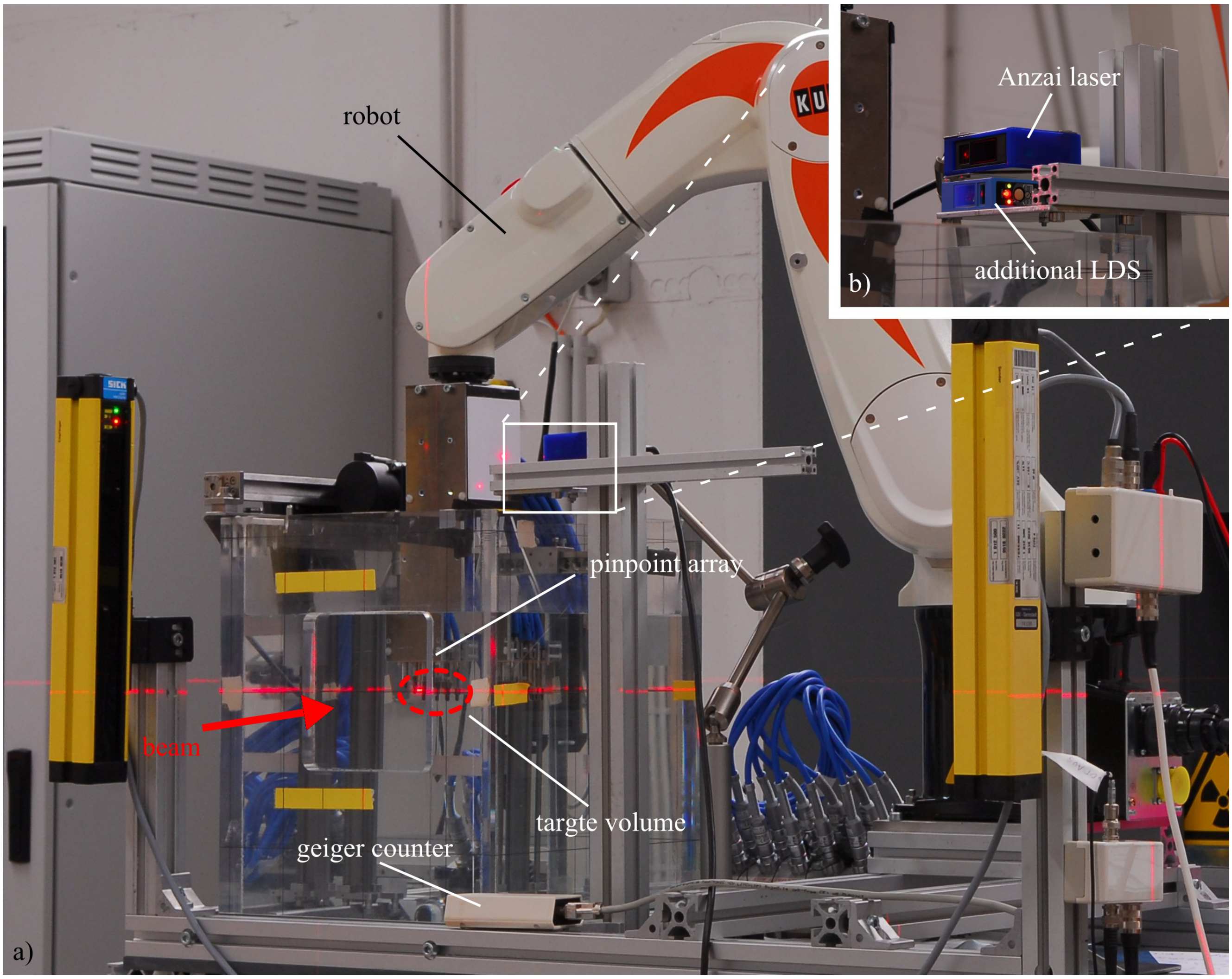

Figure 3.1.: Experimental setup. **(a)** Shown is the robot holding the pinpoint ionization chamber array within the water phantom. On the bottom the Geiger counter providing a beam status signal additionally to the one generated by the treatment control system (TCS) is placed. **(b)** The Anzai laser and an additional laser distance sensor (LDS) measure the main motion amplitude of the target motion. The Anzai is used to apply gating signals to the TCS based on the measured motion.

using as main motion component a left-right motion with a peak-to-peak amplitude A_P of 20 mm and a period T of 3 s.

Based on this motion gating signals were generated by means of the Anzai system. Gating was performed amplitude based with GWs of up to 50 % (see also section 3.2.3). Additional to the Anzai laser a second laser distance sensor (LDS) was used to measure target motion independently. Furthermore, using a Geiger counter a beam status signal which was independent from the one generated by the treatment control system (TCS) was measured.

3.2.2 Monitor calibration and divergent beam

To be able to compare results of the two nights and, in addition, make a comparison to calculations possible, appropriate calibrations had to be done. This implies two steps:

i) calibration of the used ionization chambers

ii) calibration of the beam monitor

Step one is necessary to calculate the absorbed dose from the charge collected in the ionization chamber. Ionization chambers are generally calibrated using a reference beam (e. g. ^{60}Co) at standard conditions (20 °C and 101.3 kPa). The resulting calibration factor has to be converted to the non-reference condition the chamber is used in. Protocols for such a calibration can be found in the literature [IAEA, 2000]. Important in this context is that one correction factor, the density correction, can change on time scales of hours since also air pressure and temperature can change even if an air conditioning system is in operation. Thus, this correction factor k_p/k_m was measured prior to each night using a farmer ionization chamber (PTW, Freiburg, Germany) and a ^{90}Sr-source.

Since beam monitoring is also done using ionization chambers fluctuations in the air density also affect the beam monitoring system. Besides measuring the beam position this system controls the particle numbers delivered to the target. These particle numbers are associated to machine units (MU) which are calculated from measured charges using a calibration factor. Since this calibration factor is dependent on air density delivered particle numbers may be wrong if the system is not calibrated properly. The calibration procedure is described by [Karger et al., 2010]: A farmer chamber is positioned in a solid water plate at ISO-centre and irradiated with a homogeneous field. The number of delivered particles N_ions is calculated and divided by the applied MU to get the monitor calibration factor

$$C_\mathrm{MC} = \frac{N_\mathrm{ions}}{\mathrm{MU}}. \tag{3.2}$$

This calibration factor is used to convert planned particle numbers to MU and ensures that the right particle numbers are delivered to the target.

This calibration was done prior to each measurement shift. However, due to the large setup (compare figure 3.1) the calibration could not be done in the ISO-centre but $\Delta z_{\mathrm{MC}} = -38\,\mathrm{mm}$ closer to the beam exit. Measured dose is proportional to the fluence (compare equation 2.5) and the fluence depends on the lateral grid spacing. Since the effective lateral grid spacing changes when changing the measuring position in beam's direction due to the divergent beam the measured dose changes, too. The relative dose change can be expressed as follows:

$$\frac{D(z)}{D(z_{\mathrm{ISO}})} = 1 \bigg/ \left(1 + \frac{\Delta z_{\mathrm{MC}}}{\Delta z_{\mathrm{ISO-MX}}} + \frac{\Delta z_{\mathrm{MC}}}{\Delta z_{\mathrm{ISO-MY}}} + \frac{\Delta z_{\mathrm{MC}}^2}{\Delta z_{\mathrm{ISO-MX}} \cdot \Delta z_{\mathrm{ISO-MY}}}\right) \tag{3.3}$$

where $\Delta z_{\mathrm{ISO-MX}}$ and $\Delta z_{\mathrm{ISO-MY}}$ are the distances between ISO-centre and the horizontal and vertical bending magnet, respectively. In case of the HIT QA-cave $\Delta z_{\mathrm{ISO-MX}} = 6521.9\,\mathrm{mm}$ and $\Delta z_{\mathrm{ISO-MX}} = 7223.5\,\mathrm{mm}$. Thus, in our case in the farmer chamber more dose was measured than expected leading to a too high calibration factor and, thus, to too less particles in the target. Therefore, dose results were corrected for this under dosage. In addition, equation 3.3 was experimentally validated by measuring the resulting dose of the monitor calibration irradiation plan with the farmer chamber for a Δz_{MC} of $(-40, -38, 0, 93, \text{and } 147)\,\mathrm{mm}$.

3.2.3 Beam delivery parameters and target volume

All four overlap changing beam delivery parameters were varied: lateral grid spacing Δs, iso-energy slice (IES) distance Δz, focus size (full width at half maximum (FWHM)) and Bragg-peak width. While the first three are available by requesting different accelerator settings the last parameter implies exchange of the RiFi [Weber and Kraft, 1999]. Two ripple filters were used: the "normal" 3 mm-RiFi which is also used for patient irradiations and a 2x3 mm-RiFi which consists of two 3 mm-RiFis attached perpendicular to each other. It is important that such a device does not widen the Bragg-peak twice as much as the 3 mm-RiFi does. As illustrated in figure 3.2 for a carbon beam of 250 MeV/u using a 3 mm-RiFi the Bragg-peak width at 75 % of its maximum is 3.0 mm while using the 2x3 mm-RiFi this width is 3.9 mm. Thus, the $(2 \times 3)\,\mathrm{mm}^2$-RiFi may correspond to some kind of 4 mm-RiFi.

18 plans were optimized to deliver a target dose of 2 Gy to an ellipsoidal ITV with diameters of (56, 40, and 70) mm (x-,y-, and z-direction). Cuts through the calculated stationary dose distribution including the ITV margin and pinpoint positions are shown in figure 3.3.

Plans were irradiated with GWs of up to 50 % corresponding to a maximum residual motion of 10 mm and motion phases of 0° to 180°. In the first and third row of figure 3.3 pinpoint

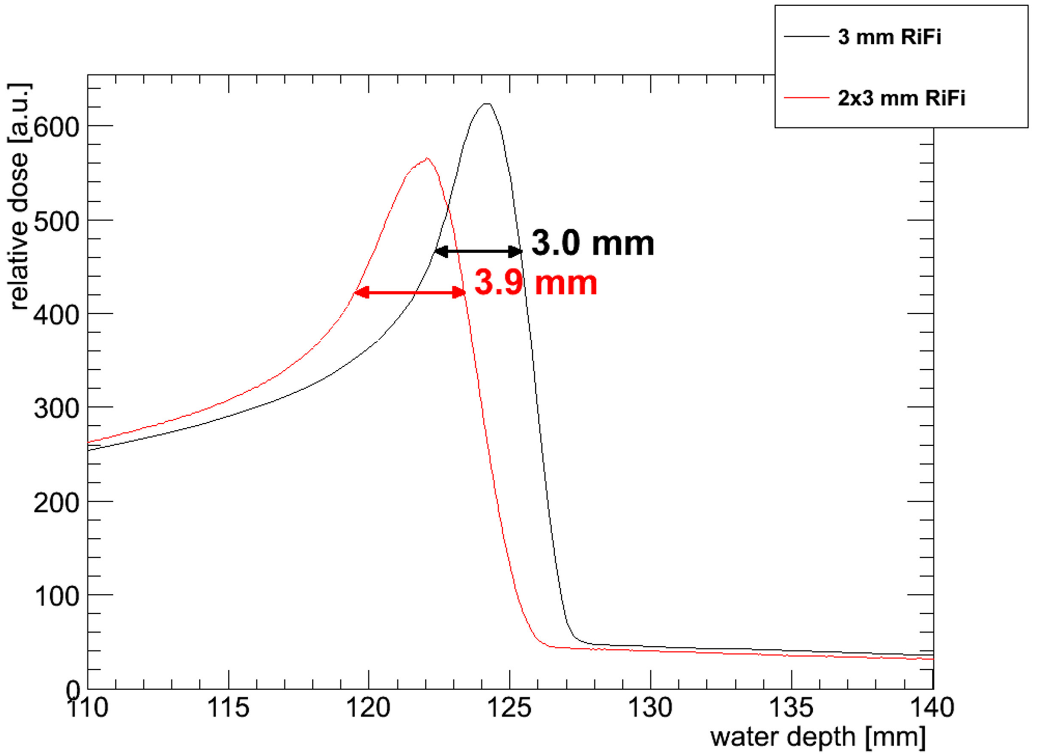

Figure 3.2.: Bragg-peak width of a 3 mm-RiFi and 2x3 mm-RiFi for a 250 MeV/u ^{12}C-beam. Widths are calculated at 75 % of the peak height.

positions for the two corner cases 0° and 180° are plotted over the stationary dose distribution. The pinpoint positions for the stationary irradiations correspond to the 90° motion state. It can be seen that some pinpoints leave the target volume during motion. Thus, for the analysis a CTV was defined as the intersection volume of the moving target volume during motion within a gating window of 50 % with the ITV. Only pinpoints within this CTV were included into the data analysis which reduces the number of used ionization chambers to 12.

Normally first the CTV is defined and the ITV is then calculated as the union of several motion states of the moving CTV. The here performed inverse definition of the CTV has practical reasons. Due to the large amount of parameters and the limited beam time we decided to use a single plan only for all residual motion amplitudes of a certain beam parameter combination.

The used parameter combinations, the measured GWs as well as the day of measurement are listed in table 3.1.

3.2.4 Data acquisition

Pinpoint doses were measured using two multichannel dosemeters (MULTIDOS® – PTW, Freiburg, Germany) which provide 12 input channels each.

Using a Beckhoff EtherCAT system (Beckhoff Automation GmbH, Frankfurt, Germany) the following data were acquired with a temporal resolution of 1 ms:

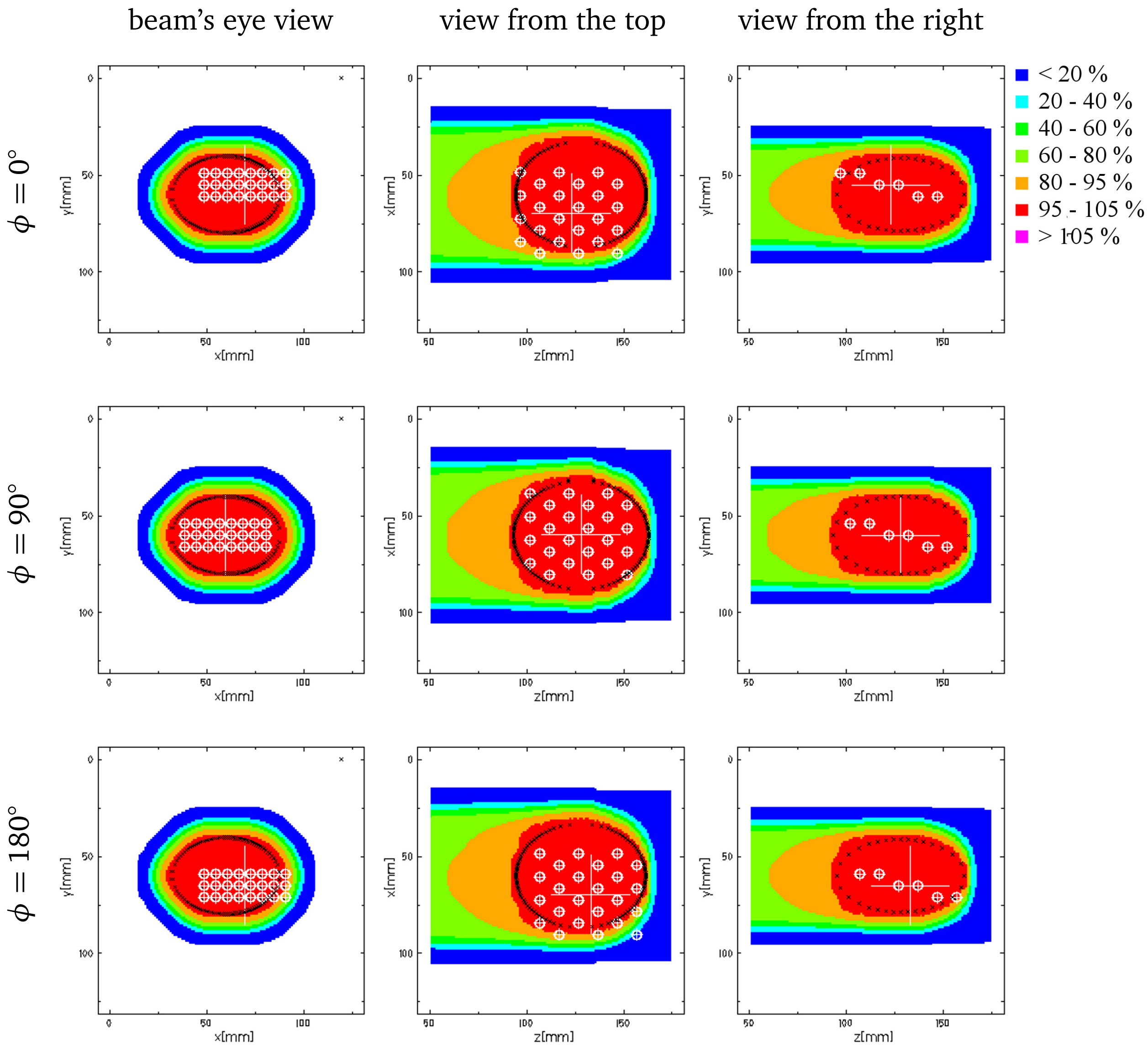

Figure 3.3.: Cuts through the stationary dose distribution in beam's eye view, top view and view from the right hand side. Intersections are drawn at target position (big white cross) for three motion phases. The two cases $\phi = 0°$ and $\phi = 180°$ are the first and last, respectively, motion state within the gating window. $\phi = 90°$ represents the motion state in the centre of the gating window which is also the position, stationary target irradiations were performed. The black contour indicates the ITV and the 24 white markers show the positions of the pinpoint ionization chambers in the three motion phases.

Table 3.1.: Measured combinations of lateral grid spacing Δs, IES-slice distance Δz, beam focus size (FWHM), ripple filter (RiFi), and residual motion amplitude.

Δs [mm]		Δz [mm]				focus [mm]			RiFi [mm]		Day	residual motion [mm]										
2	3	1	2	3	4	5	8	10	3	2x3		0	1	2	3	4	5	6	7	8	9	10
X			X			X			X		1	X		X		X						X
X			X				X		X		1	X		X		X		X			X	X
X			X					X	X		1	X				X	X	X				X
X				X		X			X		1	X		X		X						X
X				X			X		X		1	X				X		X				X
X				X				X	X		1	X				X		X				X
	X	X						X	X		1	X				X		X				X
	X		X					X	X		1	X				X		X				X
	X			X				X	X		1	X				X		X				X
X			X			X				X	2	X		X		X						X
X			X				X			X	2	X		X		X		X				X
X			X					X		X	2	X				X		X				X
X				X		X				X	2	X		X		X						X
X				X			X			X	2	X				X		X				X
X				X				X		X	2	X				X		X				X
X					X			X		X	2	X				X		X		X		X
	X		X					X		X	2	X				X		X				X
	X			X				X		X	2	X				X		X				X

i) the signal of the additional laser distance sensor (LDS) measuring the main motion component of the robot (x).

ii) the beam status signal generated by the TCS

iii) counts of a Geiger counter positioned next to the water phantom to generate an independent beam status signal

Full information (all six degrees of freedom) of the robot motion was stored to disk using dedicated logging software (see also chapter 4). In addition, log files of the Anzai system were saved which also include beam status information.

To be able to reconstruct the measured dose distributions irradiation protocols are needed comprising information which raster position was irradiated at which time. This information is provided by the treatment control system (TCS) which automatically saves beam records.

In addition, using the HIT irradiation progress monitor which is also an EtherCAT system and provides several treatment and accelerator status signals an independent irradiation protocol was acquired.

3.2.5 Data consistency analysis

Besides monitor calibration prior each measurement day a film was irradiated with a homogeneous square and 15 beam spots corresponding to 3 focus levels for 5 energies ((221, 243, 260, 277, and 294) MeV/u) distributed over the used energy range. The films were registered to ISO-centre by four holes which were pierced into the film at the position of the laser-cross defining the ISO-centre in the treatment room. Using a dedicated film analysis framework [Steidl et al., 2011] the homogeneous square was analysed in respect of film homogeneity index $\mathrm{HI_F}$ which is calculated from the mean and standard deviation (SD) of the optical density (OD) in a region of interest (ROI) of $(50 \times 50)\,\mathrm{mm}^2$ as follows:

$$\mathrm{HI_F} = 1 - \frac{\mathrm{SD}}{\mathrm{Mean}}. \tag{3.4}$$

Furthermore, beam spot positions and sizes were calculated.

To check data consistency the beam records were analysed and results for the two days were compared. Amongst others the actually measured beam focus sizes were extracted from the beam records and compared to the nominal values for all irradiated plans.

Target motion accuracy was investigated using the robot log files. Actually applied amplitudes and trajectory shapes were compared to the planned motion. Furthermore, motion periods and phase shifts were investigated.

3.2.6 Dose reconstruction

Based on the recorded data dose distributions were reconstructed using the 4D version of the GSI treatment planning system TRiP [Bert and Rietzel, 2007; Kraemer et al., 2000; Richter et al., 2010c, 2011]. Dose reconstruction was done as part of the validation of 4DTRiP by Daniel Richter [Richter et al., 2010b] and is only presented here to motivate that the 4D calculation reproduces measured data and can, thus, be used for the simulation study presented below. From the reconstructed dose distributions dose values at the pinpoint positions within the CTV were extracted and compared to the measured doses.

3.2.7 Simulation study

For all measured beam parameter combinations (all 18 irradiation plans) for a GW corresponding to a residual motion of 0 mm to 10 mm in steps of 1 mm dose distributions were calculated for four starting phases ((0, 90, 180, and 270) °). For one parameter combination ($\Delta s = 2\,\text{mm}$, $\Delta z = 3\,\text{mm}$, focus of 10 mm FWHM and 3 mm-RiFi) for residual motion amplitudes of (1, 5, and 10) mm even 30 starting phases were calculated (each 12°). Calculations were based on the ideal target motion trajectory (equation 3.1) segmented into 22 motion states. Beam delivery records were simulated using a dedicated software which links motion trace, desired gating window, irradiation plan, intensity levels which would have been chosen for the corresponding plan at HIT, and realistic beam delivery timing [Naumann, 2011] assuming a rectangular beam extraction profile.

3.2.8 Data analysis

Measured dose values were corrected by a factor of 1.011 due to the way beam monitor calibration was performed (compare section 3.2.2) to enable comparison to calculated dose distributions. As mentioned above only pinpoints located within the CTV were included in data analysis which reduces the number of dose values to 12. The standard deviation of these 12 measured doses was calculated as well as the deviation from the results for corresponding stationary irradiations and the root mean square (RMS) of the deviation.

Simulation results were compared to the measured data as it was done with the reconstructed dose distributions: dose values were extracted from the dose distributions at the pinpoint positions within the CTV and compared to the measurements.

Based on all voxels within the CTV for each case a dose volume histogram (DVH) was calculated. Amongst other parameters homogeneity and conformity was investigated: According to [Wu et al., 2003] a homogeneity index

$$\mathrm{HI_D} = D_2 - D_{98} \tag{3.5}$$

was analysed where D_2 and D_{98} are the minimum doses delivered to 2 % and 98 % of the CTV, respectively. This value represents the steepness of the DVH and is zero in an ideal homogeneous case. Then the fraction of dose delivered to the CTV was estimated by calculating a conformity index

$$\mathrm{CI} = \frac{\int_{\mathrm{CTV}} D(x, y, z)}{\int D(x, y, z)}. \tag{3.6}$$

3.3 Results

3.3.1 Data correction

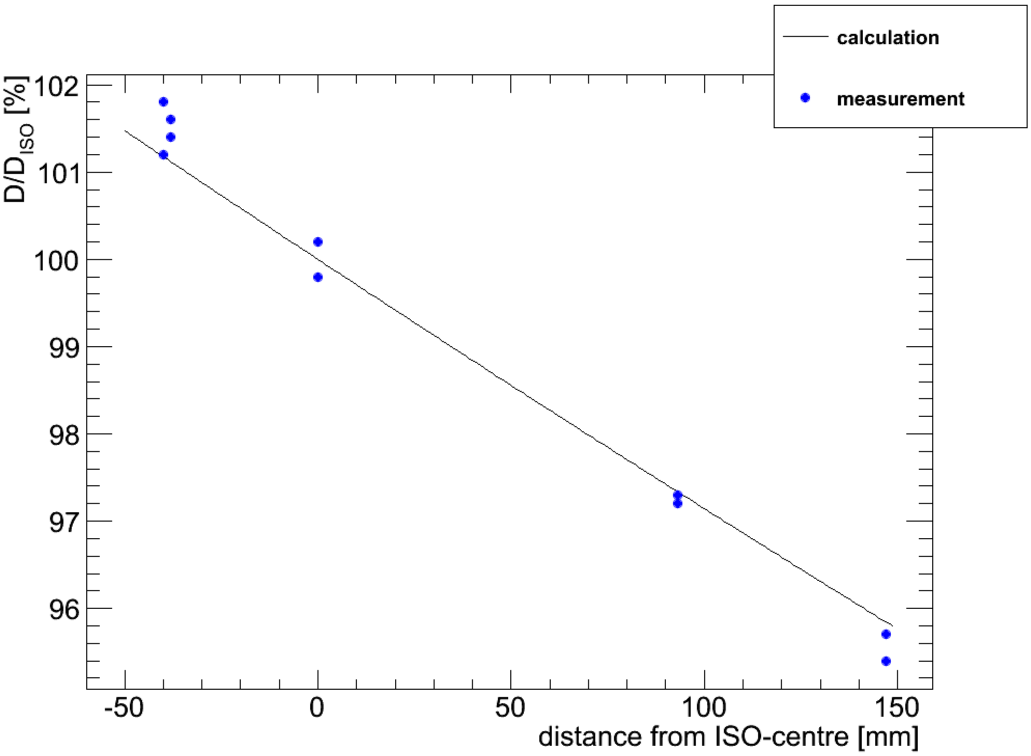

Figure 3.4.: Dose dependency on the distance from ISO-centre. Plotted are measurements performed with the beam monitor calibration setup and a calculation based on equation 3.3.

Figure 3.4 shows the results for the measured doses acquired with the monitor calibration setup for different distances from ISO-centre. The line shows the calculation according to equation 3.3. Based on this investigation a dose correction factor for doing monitor calibration −38 mm in front of the ISO-centre (BEV) was based on calculation determined to be 1.011.

3.3.2 Data consistency analysis

Table 3.2.: Film results of the beam quality check. For each day the film measured FWHM in x and y direction of the beam foci and the $\mathrm{HI_F}$ is given.

Day	focus level 2				focus level 3				focus level 4				$\mathrm{HI_F}$
	FWHM_x		FWHM_y		FWHM_x		FWHM_y		FWHM_x		FWHM_y		
	Mean [mm]	SD [mm]	Mean [mm]	SD [mm]	Mean [mm]	SD [mm]	Mean [mm]	SD [mm]	Mean [mm]	SD [mm]	Mean [mm]	SD [mm]	
1	6.4	0.3	6.5	0.5	8.8	0.5	9.2	0.6	10.8	0.3	11.9	0.8	0.98
2	6.3	0.1	6.4	0.4	8.9	0.6	9.0	0.4	10.7	0.5	11.7	1.1	0.98

Table 3.2 shows the results for beam spot sizes and field homogeneity using film measurements. The mean and standard deviation (SD) of focus sizes in x and y direction as well as the film homogeneity $\mathrm{HI_F}$ are given. Focus level 2 corresponds to a desired value of 5 mm full width at half maximum (FWHM), level 3 to 8 mm FWHM and level 4 to 10 mm FWHM beam focus, respectively.

Results of the focus size analysis based on the beam delivery records are given in figure 3.5. For each irradiated plan of the two days the mean and the standard deviation of the measured FWHM of the beam in x and y direction is plotted.

3.3.3 Dose reconstruction

A comparison of measured versus reconstructed dose distributions is given in figure 3.6: for 53 cases the deviation between measured and reconstructed doses is given. The plot shows the mean and the standard deviation of the differences between doses of 12 pinpoint ionization chambers within the CTV and 12 corresponding dose values extracted from the reconstructed dose distribution. The plot shows a systematic overestimation of the dose by the calculation of 1.5 %.

3.3.4 Lateral overlap: varying grid spacing

Figure 3.7 shows the relative standard deviation of the 12 pinpoint ionization chambers and, respectively, dose extraction points of the measurements, reconstructions and simulations. In

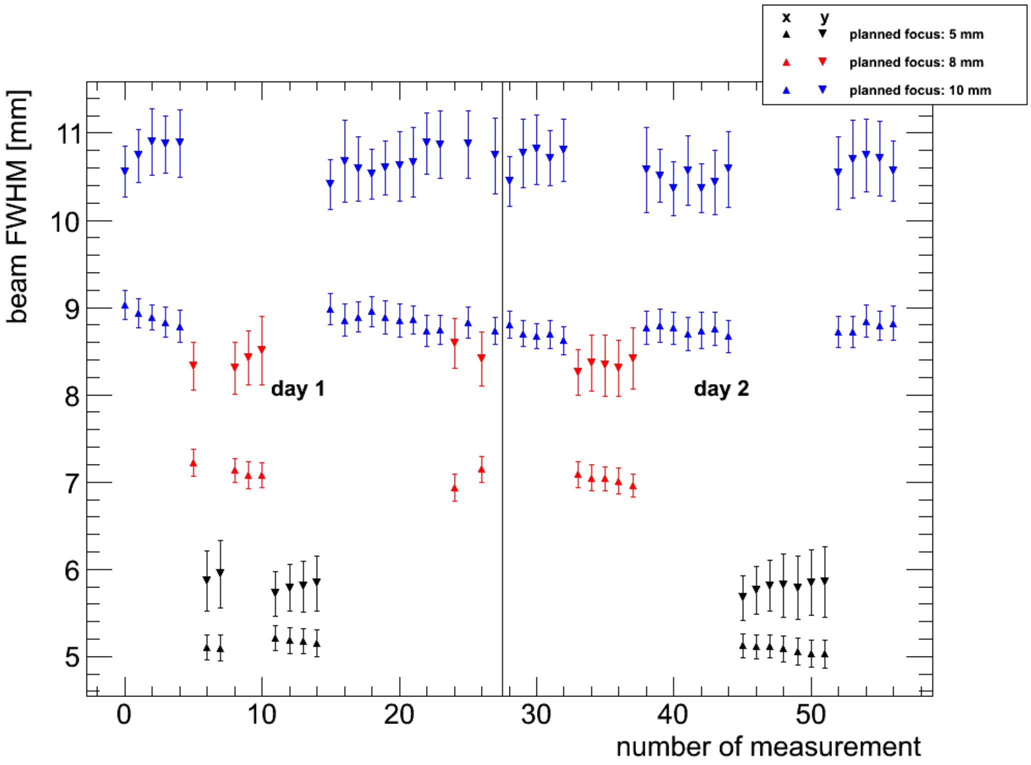

Figure 3.5.: Results of the beam focus analysis based on beam records.

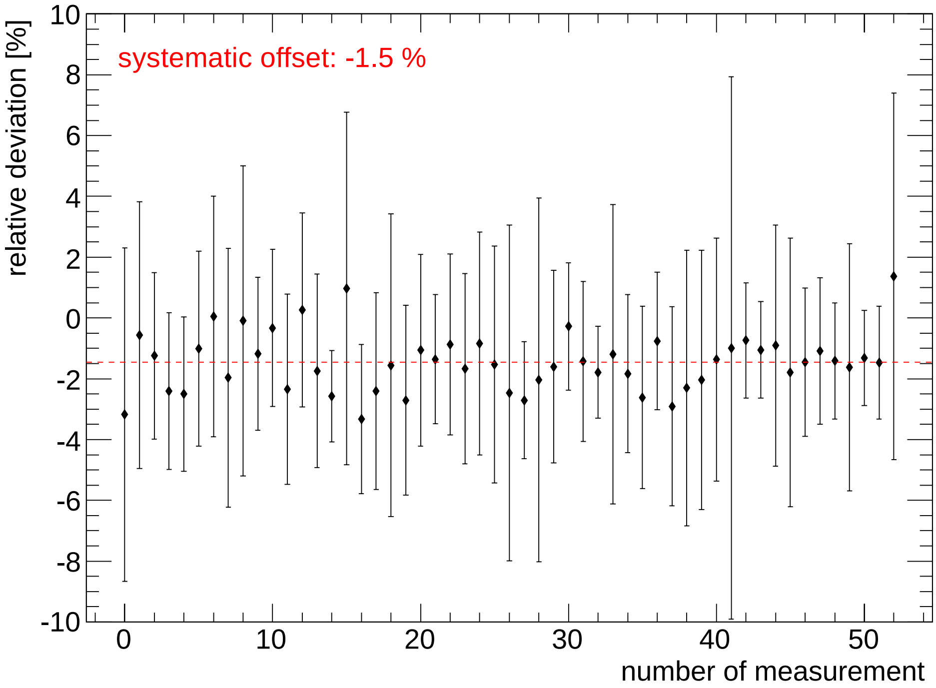

Figure 3.6.: Comparison between measured and reconstructed doses. The red dashed line indicates the mean of the mean deviations resulting in a systematic offset of $1.5\,\%$.

all four cases with respect to a focus of 10 mm results for a lateral grid spacing Δs of 2 mm and 3 mm, respectively, are plotted. In addition, linear fits are included into the graphs.

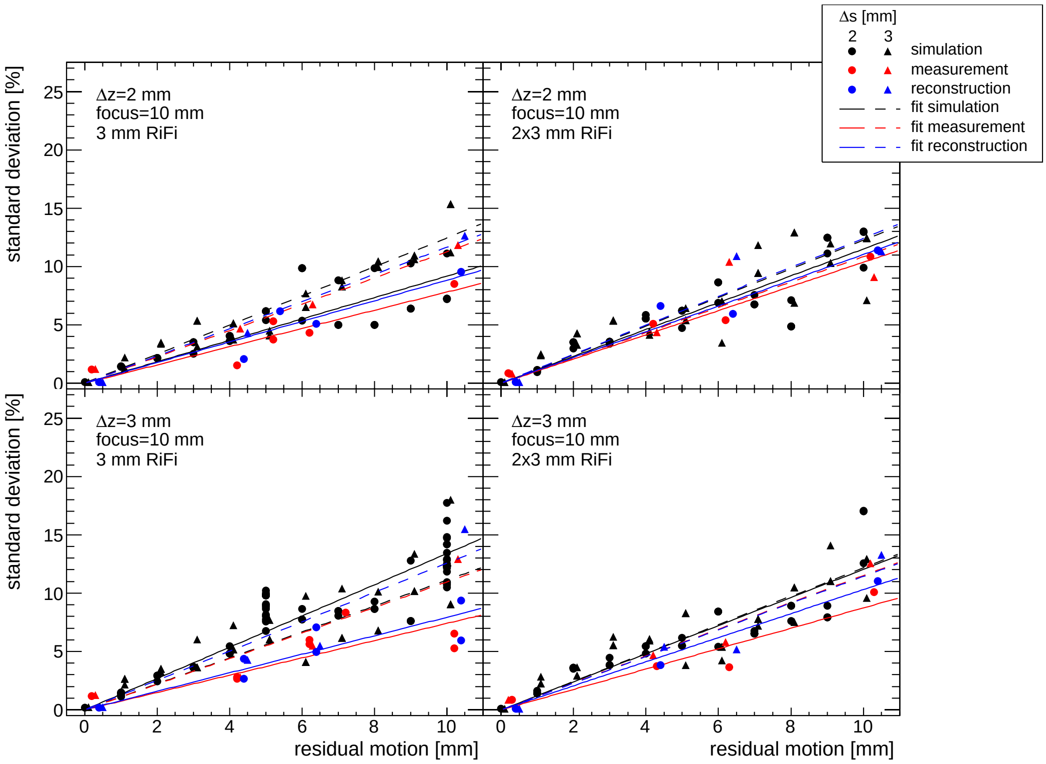

Figure 3.7.: Relative standard deviation for varying lateral grid spacing. More than one data point per residual motion amplitude reflects different starting phases.

Figure 3.8 shows the simulation results in respect of homogeneity index $\mathrm{HI_D}$ based on all voxels within the CTV. Plotted are the same four combinations as described above. Again linear fits are included into the graphs.

In figure 3.9 for all cases with focus size of 10 mm the slope of the linear fit is plotted against the lateral grid spacing Δs.

3.3.5 Lateral overlap: varying beam focus

Results for the relative standard deviation of the 12 pinpoint ionization chambers for increased focus sizes are given in figure 3.10 for the measurements, reconstructions and simulations. Referring to a lateral grid spacing of 2 mm results for a focus size of (5, 8, and 10) mm, respectively, are shown together with corresponding linear fits.

Figure 3.11 shows results of the homogeneity index $\mathrm{HI_D}$ within the whole CTV for the simulations. The figure displays the same four combinations as described above including linear fits for the different parameter combination cases.

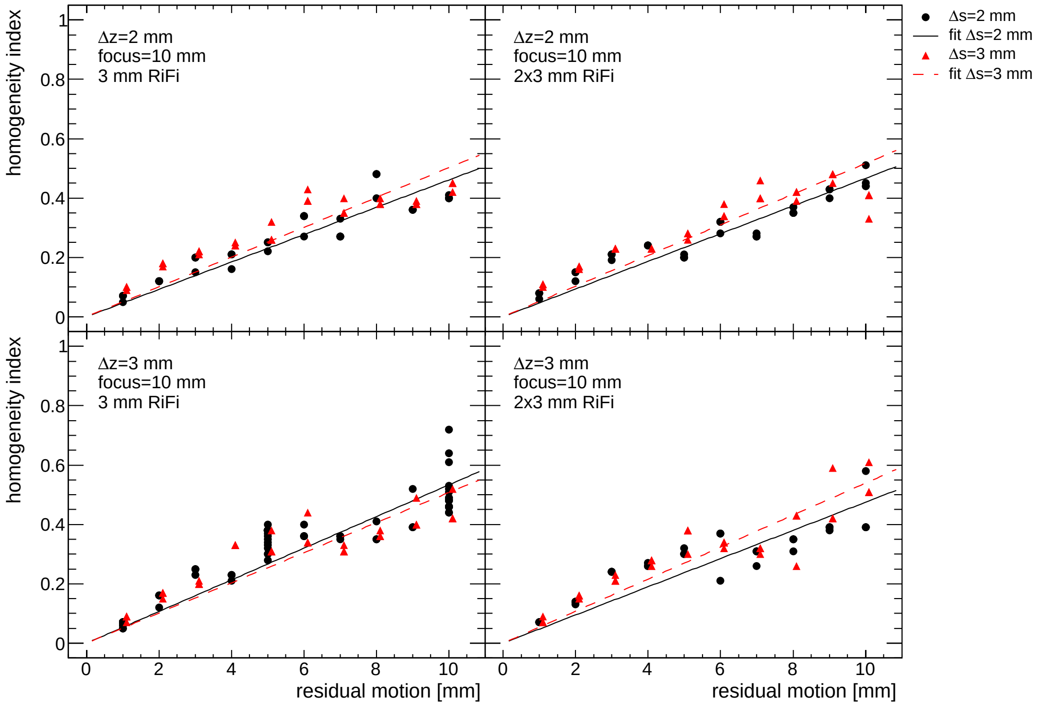

Figure 3.8.: Simulations: Homogeneity index for varying lateral grid spacing. More than one data point per residual motion amplitude reflects different starting phases.

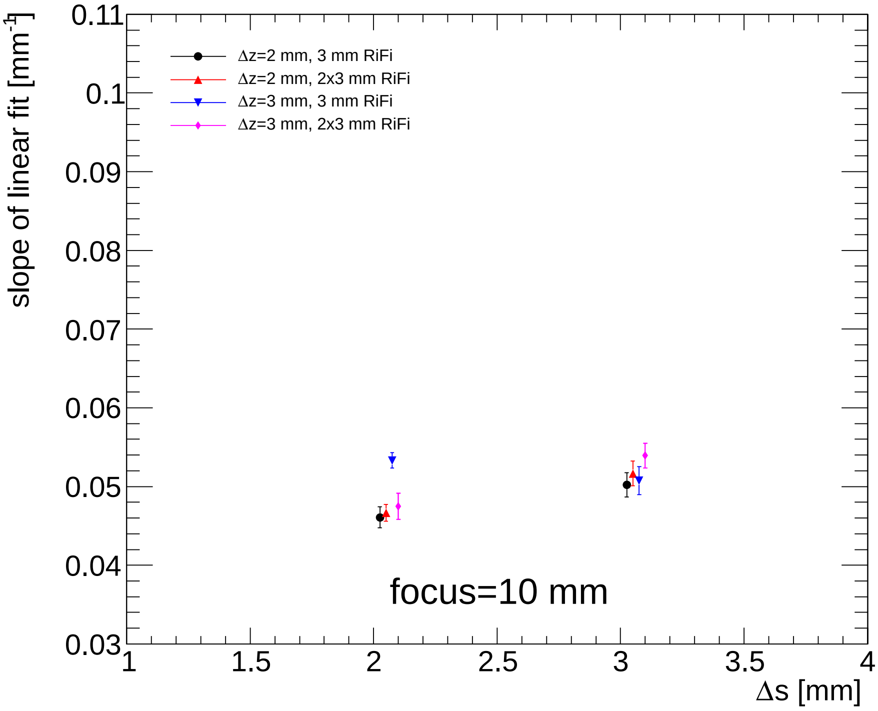

Figure 3.9.: Simulations: Slopes of the linear fitted homogeneity indices for varying lateral grid spacing.

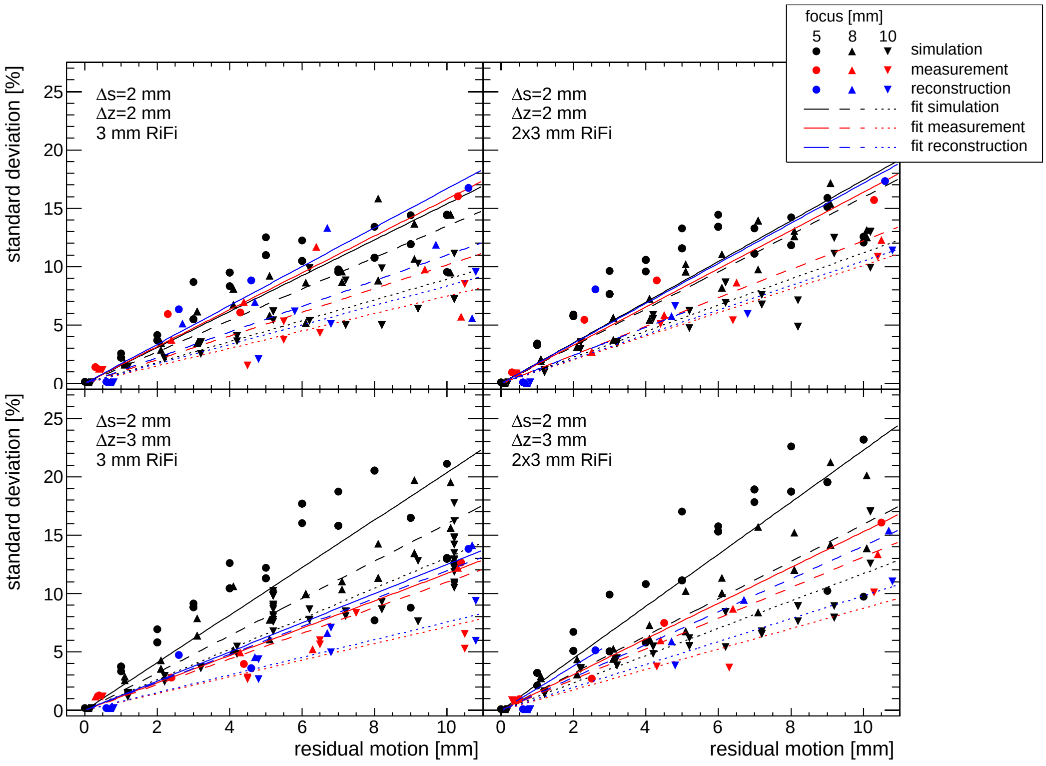

Figure 3.10.: Relative standard deviation for varying beam focus. More than one data point per residual motion amplitude reflects different starting phases.

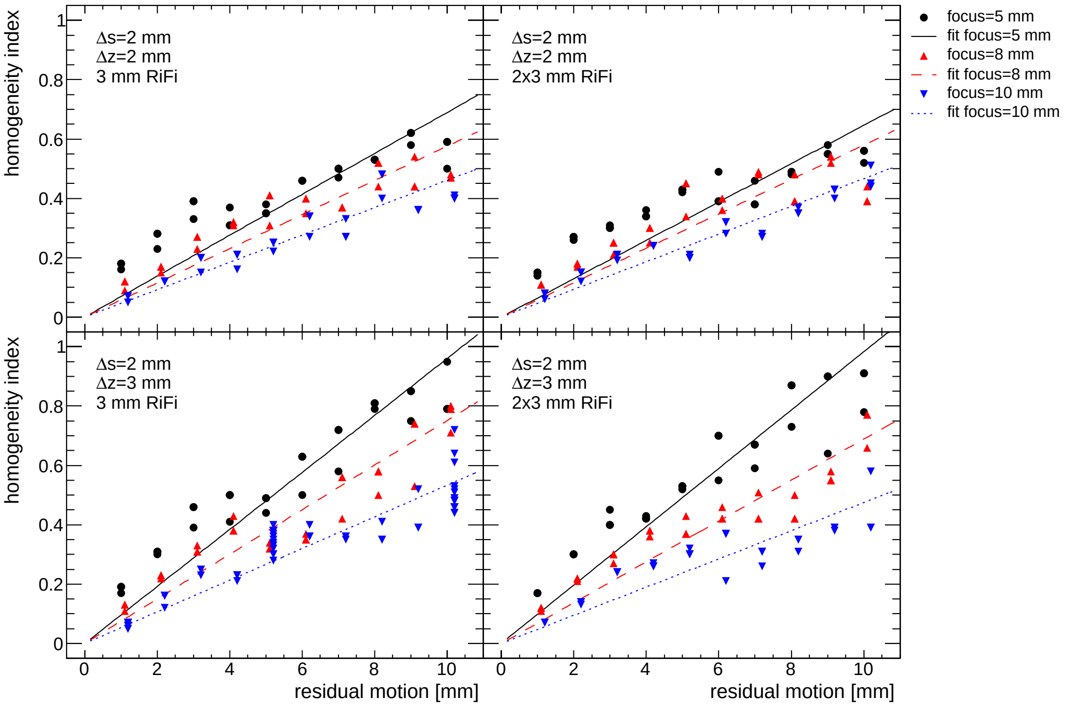

Figure 3.11.: Simulations: Homogeneity index for varying beam focus. More than one data point per residual motion amplitude reflects different starting phases.

As a summary plot the slopes of the linear fits are given in figure 3.12 for all cases with lateral grid spacing of 2 mm for varying focus size.

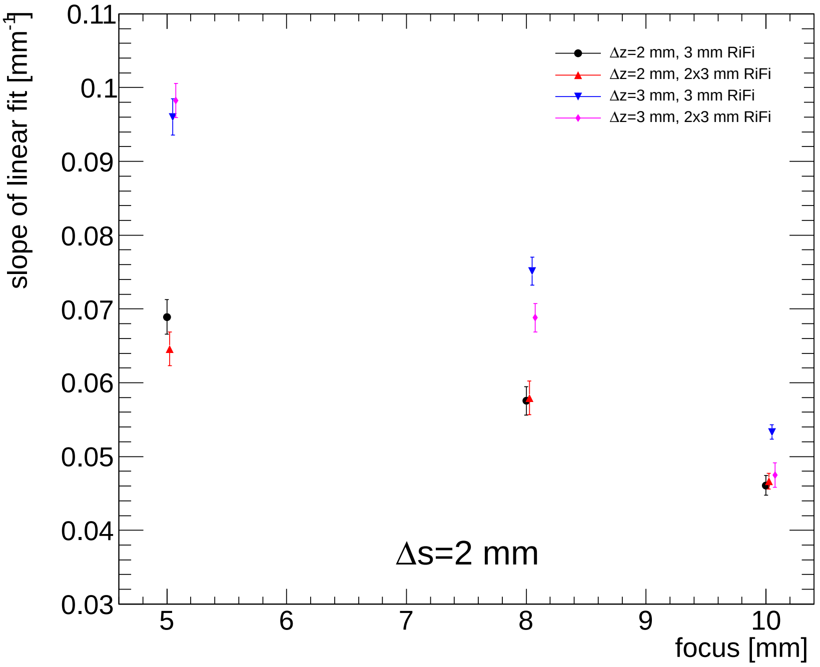

Figure 3.12.: Simulations: Slopes of the linear fitted homogeneity indices for varying beam focus.

3.3.6 Lateral overlap: varying slice distance

Also for varying slice distance in figure 3.13 first the results for the relative standard deviation of the 12 pinpoint ionization chambers are shown with corresponding reconstructions and simulations. In respect of the two used ripple filters results for IES distances Δz of (1, 2, 3, and 4) mm are given including linear fits.

Figure 3.14 shows the homogeneity index $\mathrm{HI_D}$ resulting from the simulations. Besides the values based on the whole CTV linear fits are displayed.

In figure 3.15 for all cases with 3 mm-RiFi and 2x3 mm-RiFi, respectively, the slope of the linear fit is plotted against the IES distance.

3.3.7 Lateral overlap: varying ripple filter

Figure 3.16 shows the relative standard deviation of the 12 dose values extracted from the reconstructed and simulated dose distributions together with the 12 pinpoint measurement results. For the two ripple filters the eight different combinations are given where the ripple filter was varied. Linear fits indicate the slope of the behaviour.

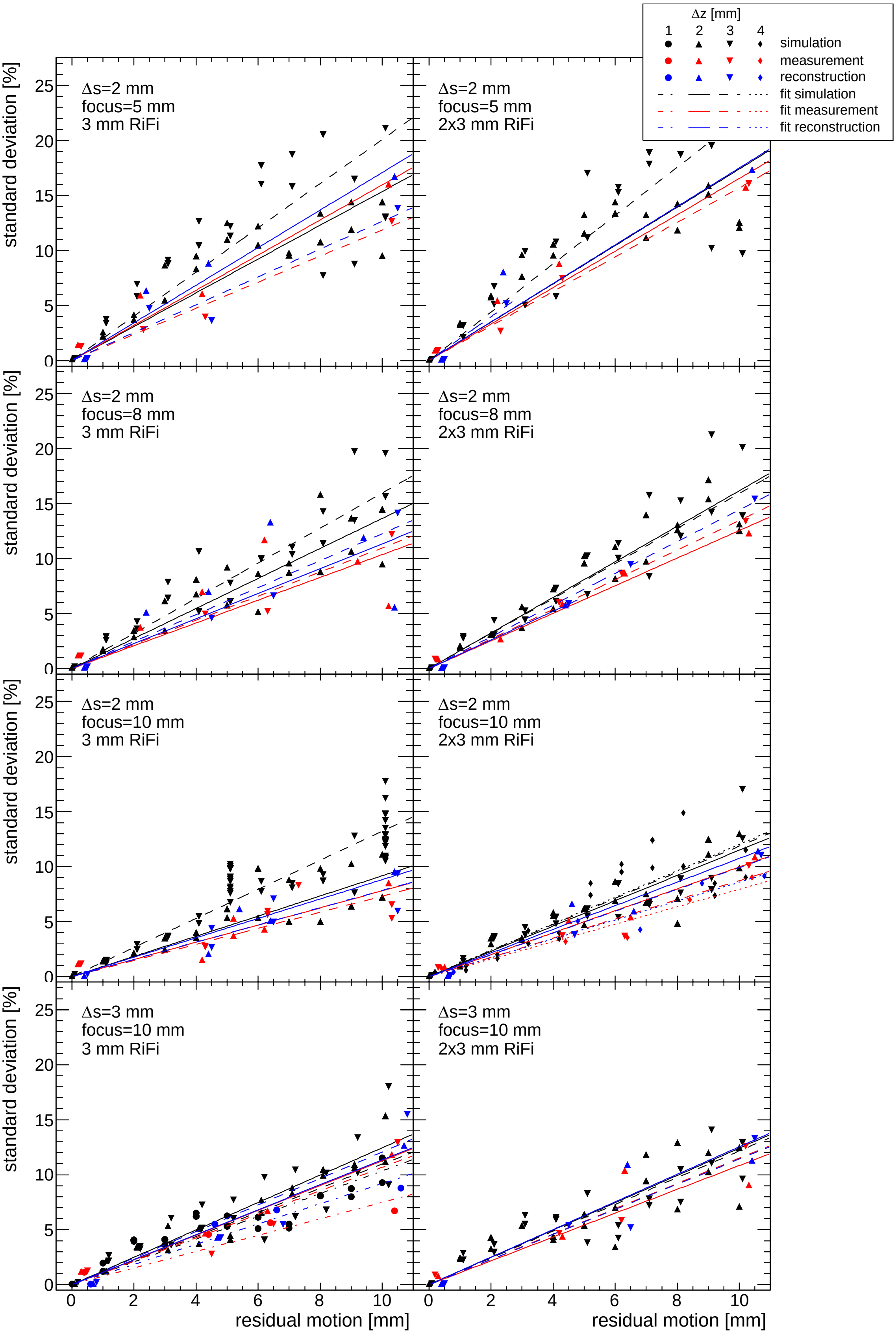

Figure 3.13.: Relative standard deviation for varying slice distance. More than one data point per residual motion amplitude reflects different starting phases.

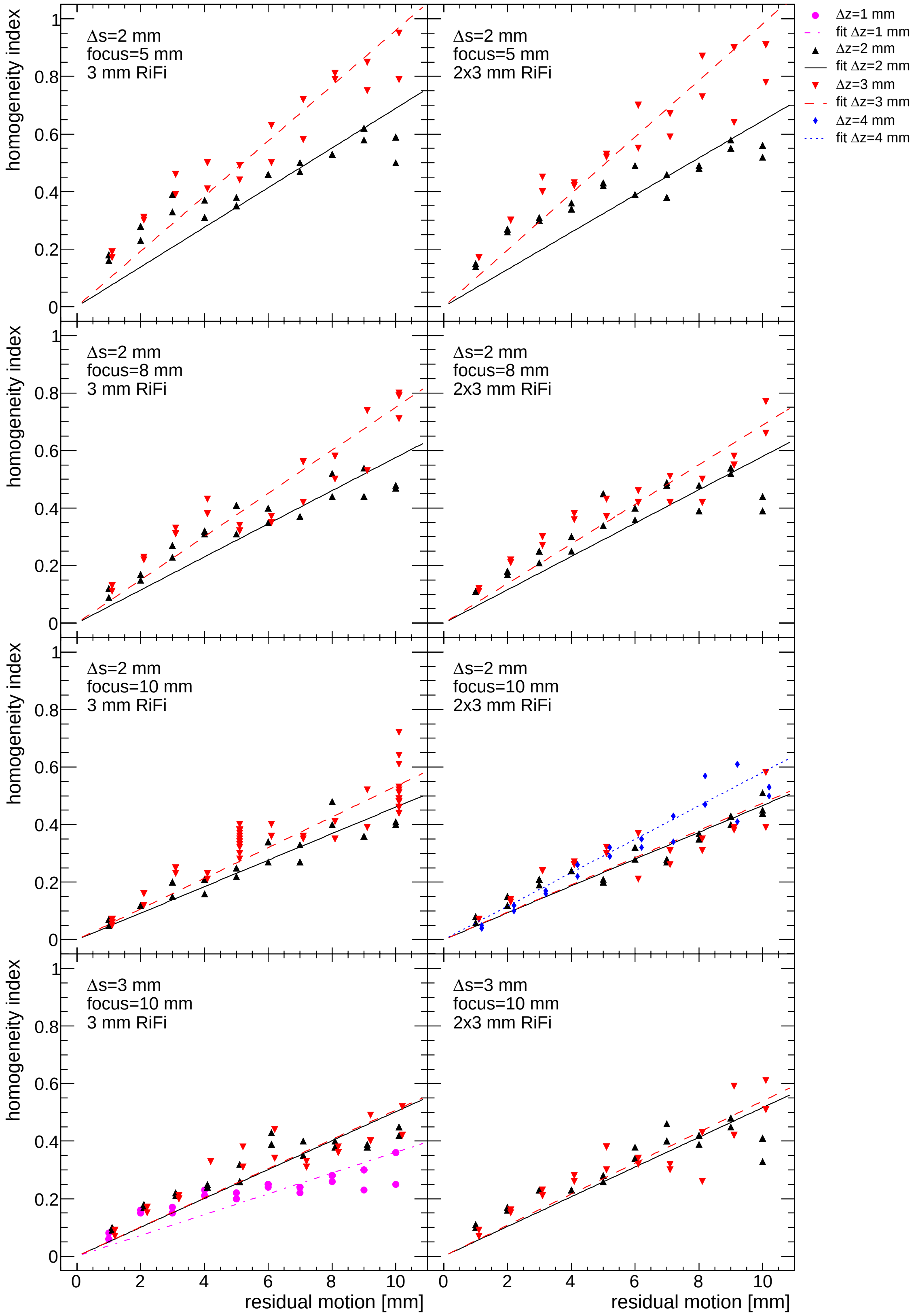

Figure 3.14.: Simulations: Homogeneity index for varying slice distance. More than one data point per residual motion amplitude reflects different starting phases.

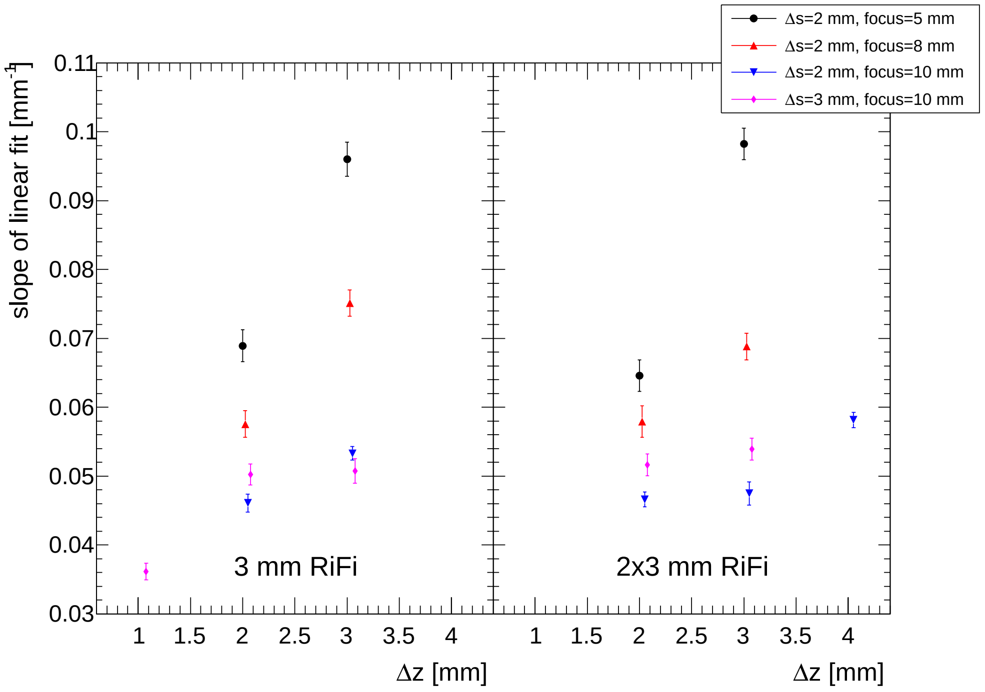

Figure 3.15.: Simulations: Slopes of the linear fitted homogeneity indices for varying slice distance.

Simulation results with respect to the homogeneity index HI_D based on all voxels within the CTV are plotted in figure 3.17. Besides showing the pure values again linear fits are included.

The resulting slopes of the linear fits are given in figure 3.18 for all cases with 3 mm-RiFi and 2x3 mm-RiFi, respectively.

3.3.8 Conformity index

The conformity index CI turned out to be independent on grid spacing and ripple filter. Only changing the focus size leads to differences which are shown in figure 3.19.

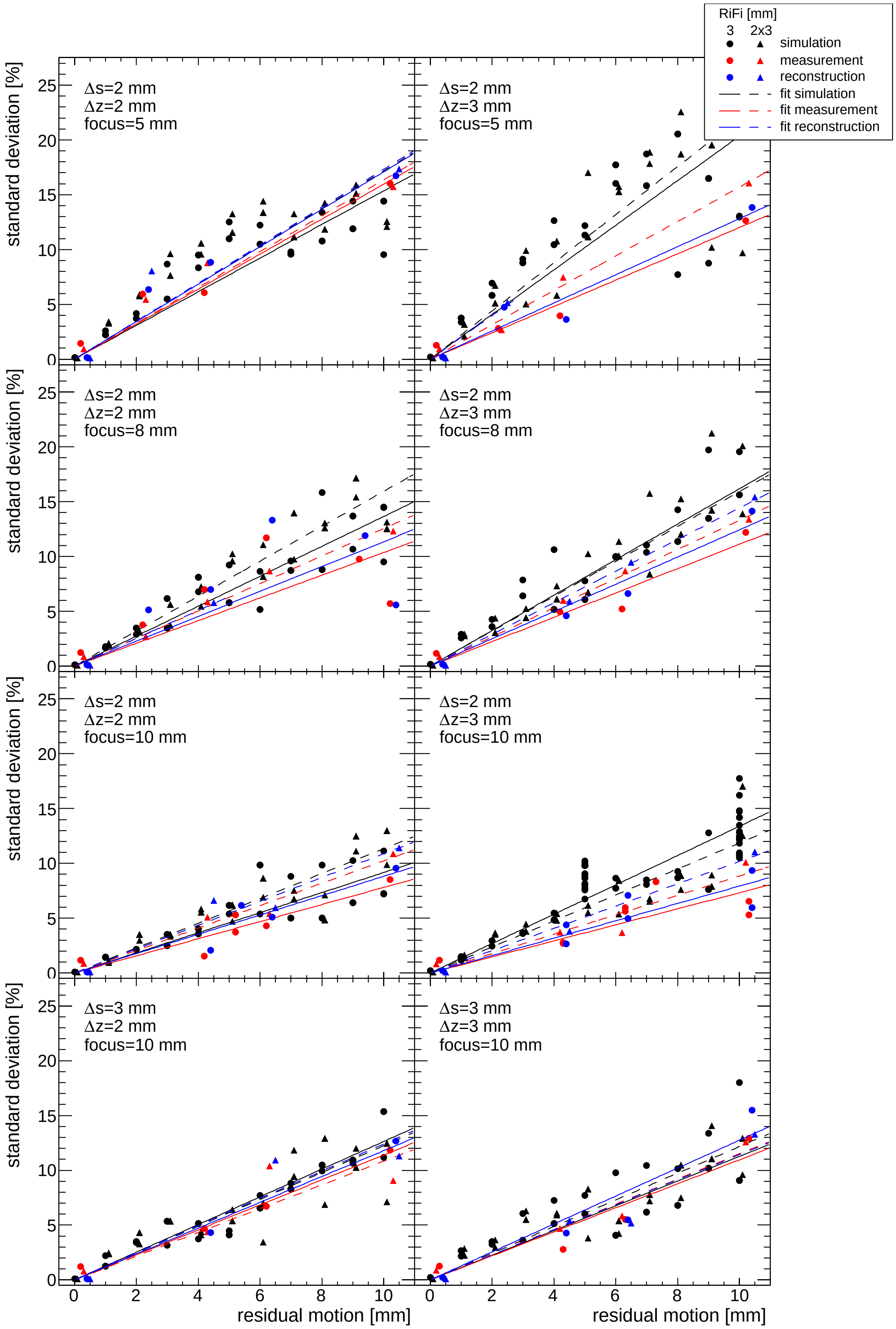

Figure 3.16.: Relative standard deviation for varying ripple filter. More than one data point per residual motion amplitude reflects different starting phases.

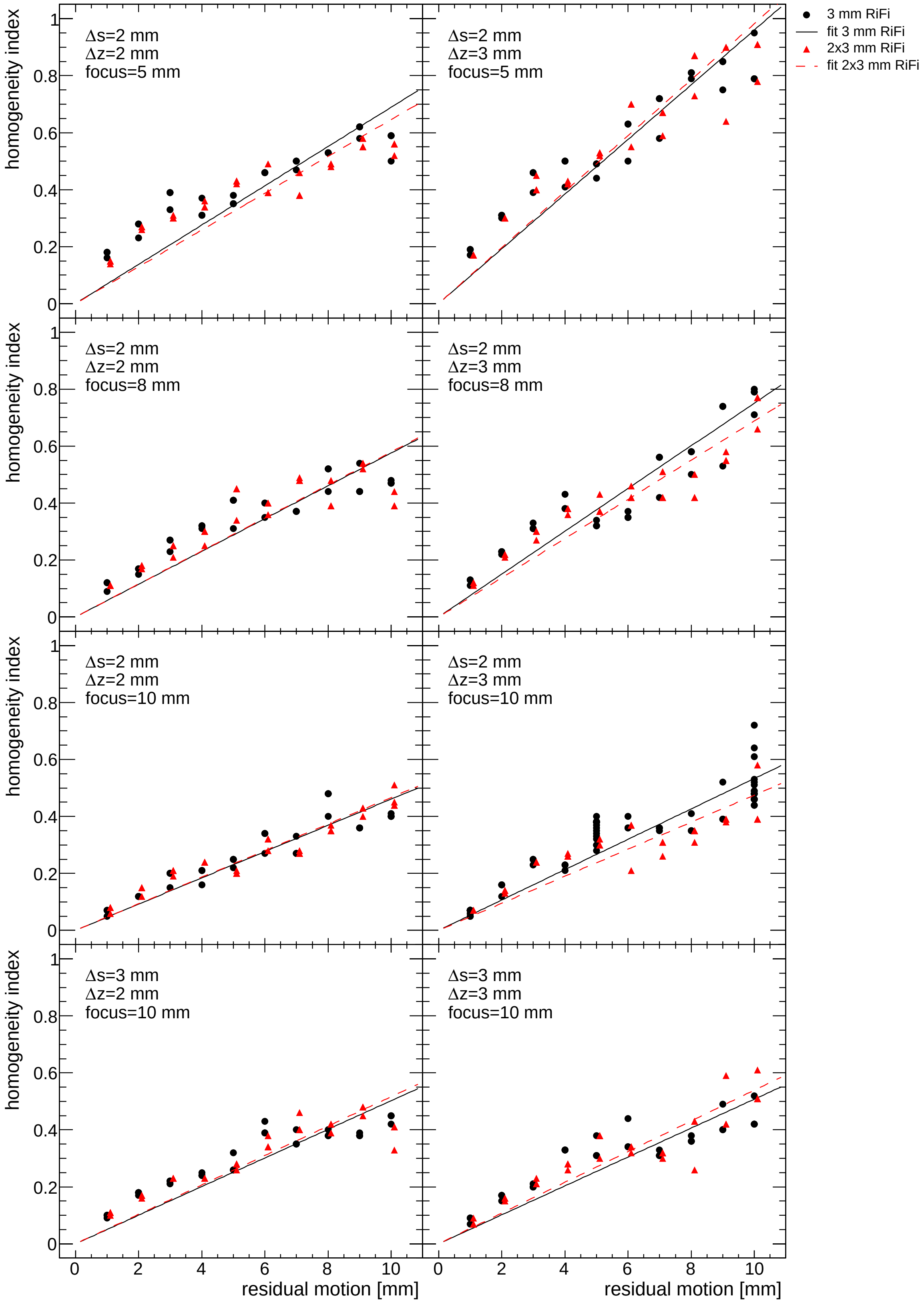

Figure 3.17.: Simulations: Homogeneity index for varying ripple filter. More than one data point per residual motion amplitude reflects different starting phases.

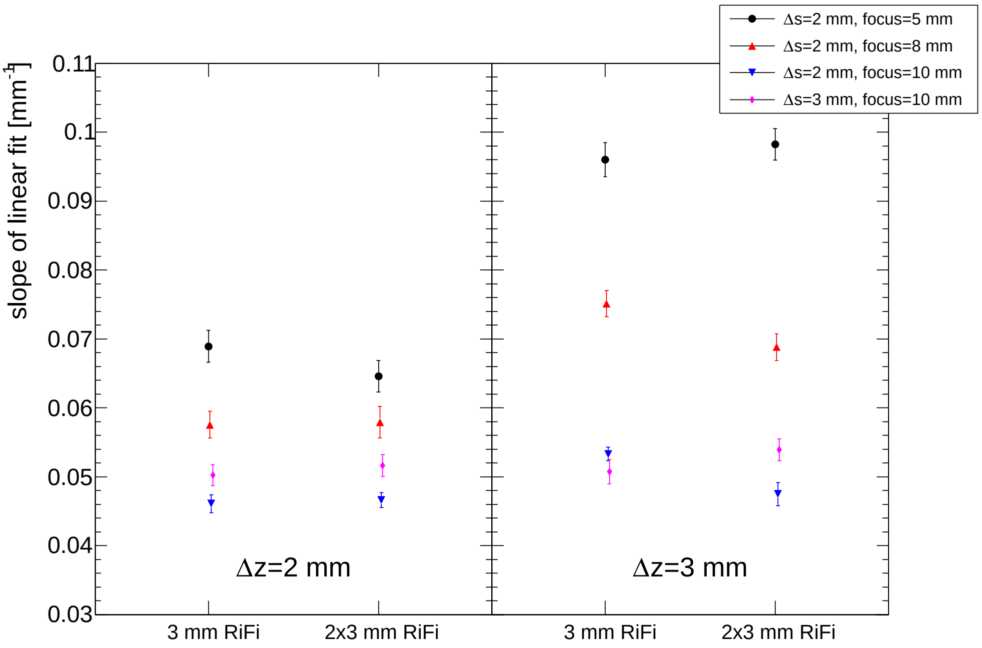

Figure 3.18.: Simulations: Slopes of the linear fitted homogeneity indices for varying ripple filter.

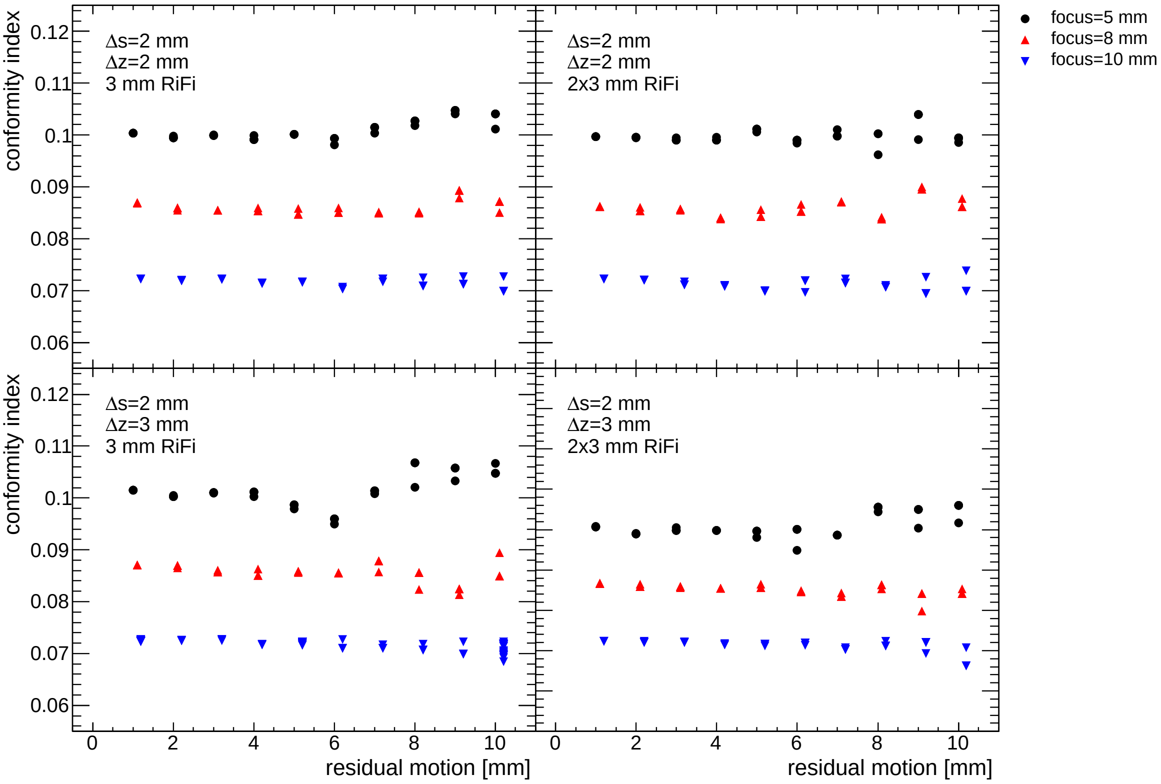

Figure 3.19.: Simulations: Conformity index for varying focus size. More than one data point per residual motion amplitude reflects different starting phases.

3.4 Discussion

Due to the need of performing the beam monitor calibration in front of the ISO-centre (BEV) and because of the divergent beam fewer particles than planned were delivered to the target. The calculated correction factor of 1.011 is slightly lower than the measured one (compare figure 3.4). The slope of the calculated curve differs from the slope of the measured values which may be due to little influence of scattering which is not included into the calculation. This difference may introduce a systematic offset of the measured doses. However, since this difference is far below the expected uncertainty for ion-chamber dosimetry of 3 % [Karger et al., 2010] this effect should be negligible.

Results of the radiographic film irradiated to check the beam quality showed that beam focus size and field homogeneity stayed constant for the two days during which measurements were performed. Differences in FWHM_x and FWHM_y of the beam spots (compare table 3.2) are originated by the beam delivery system at HIT and were characterized by [Parodi et al., 2010]. Measured focus sizes are about 1 mm larger than the planned ones. However, in case of film measurements it is difficult to estimate the real FWHM of the beam since film response is not linear and the total blackening depends on the particle number directed to the spot position.

Differences in x and y direction were also found in the beam monitor measurements extracted from the beam records (compare figure 3.5). For comparison to planned focus sizes one may associate the asymmetric beam spots with the mean width over all values in x and y direction. By doing so for focus level 2 (planned size 5 mm FWHM) a mean of 5.5 mm, for focus level 3 (planned size 8 mm FWHM) a mean of 7.7 mm, and for focus level 4 (planned size 10 mm FWHM) a mean of 9.7 mm results. These values differ from the planned sizes by less than 10 % which is acceptable. Furthermore, the focus sizes stayed constant over all measurements on both days which is even more important. Thus, beam quality turned out to be comparable on the two days which makes a comparison of the measurements possible.

Measured doses and reconstructed dose distributions showed good agreement. The little offset of −1.5 % lies within the expected uncertainty of ion-chamber based dosimetry of 3 % [Karger et al., 2010]. This good agreement validates that the 4D capable version [Bert and Rietzel, 2007; Richter et al., 2010c, 2011] of the GSI's treatment planning software TRiP [Kraemer et al., 2000] can be used to increase the parameter space for the beam parameter study by simulations.

Variation of the lateral grid spacing Δs showed only in some cases the expected result. The standard deviation of the 12 pinpoint ionization chambers turned out to be higher for larger grid spacing only in two of four cases ($\Delta z = 2$ mm, 10 mm focus, both RiFis in figure 3.7). In the other two cases ($\Delta z = 3$ mm, 10 mm focus, both RiFis) the simulations showed even increased standard deviation for lower grid spacing while measurements resulted in the opposite behaviour. This heterogeneous result may occur due to two effects: First reason may be the differing number of values for measurements and reconstructions compared to simulations where more amplitudes and starting phases were calculated. In some cases for measurements and reconstructions dose values may not be representative for a certain amplitude. This is reasonable when considering the large variation of relative standard deviations in respect of different starting phases found for the simulations in larger residual motion amplitudes (compare e. g. figure 3.7, $\Delta s = 3\,\mathrm{mm}$, 10 mm focus, 3 mm-RiFi, 10 mm residual motion). Second reason seems to be the small effect of variation in lateral grid spacing on dose homogeneity which was found in the simulations (compare figure 3.8). Slopes differ only by $3 \times 10^{-3}\,\mathrm{mm}^{-1}$ to $6 \times 10^{-3}\,\mathrm{mm}^{-1}$ (compare figure 3.9) which is much lower than slope differences found e. g. for variation of beam focus size (compare figure 3.12).

Beam focus size turned out to affect dosimetric results substantially. Measurements, reconstructions and simulations showed in all cases lower relative standard deviations of the 12 ionization chamber values and, respectively, dose values extracted from the calculated dose distribution for increased beam focus size (compare figure 3.10). This effect was also found for the homogeneity index (compare figure 3.11) and resulted in differences in the slope of the linear fit by $1.5 \times 10^{-2}\,\mathrm{mm}^{-1}$ to $3 \times 10^{-2}\,\mathrm{mm}^{-1}$ (compare figure 3.12).

Variations in IES distance Δz showed for a beam focus of 8 mm the expected behaviour and good agreement of measurement, reconstruction and simulation (compare figure 3.13). In the other cases of the comparison with respect to relative standard deviation only the simulation resulted in larger values for larger Δz. This may again occur due to less data points measurements and reconstructions are based at. In almost all cases the homogeneity index rises for increased Δz (compare figure 3.14) resulting in slope changes of $0.4 \times 10^{-2}\,\mathrm{mm}^{-1}$ to $3.4 \times 10^{-2}\,\mathrm{mm}^{-1}$ (compare figure 3.15). Only for a focus of 10 mm changes were small and comparable to the ones observed for varying Δs. However, in two of these cases a change to a Δz of 1 mm and 4 mm, respectively, showed again a larger difference. The smaller effect for the large focus size may occur, because the large focus already leads to robustness which can not further be improved by reduction of Δz from 3 mm to 2 mm.

Exchange of the 3 mm-RiFi by a 2x3 mm-RiFi does not seem to gain better results. In most cases for relative standard deviation and homogeneity index observed changes were small (compare figure 3.16 and figure 3.17). Slope changes are lower than $0.5 \times 10^{-2}\,\mathrm{mm}^{-1}$ (compare figure 3.18). This little effect may be due to the small increase of Bragg-peak width gained by the 2x3 mm-RiFi compared to the 3 mm-RiFi (compare figure 3.2).

The results of the conformity index clearly show the drawback of increasing the focus size: the size of the volume where dose is delivered to increases which leads to a smaller conformity index for higher beam focus sizes (compare figure 3.19). If conformity is a criterion for an acceptable dose distribution which is always true in patient irradiations this effect has to be considered when increasing the beam focus size.

In summary the measurements not always showed the same tendencies than the calculations. If the effect of a particular parameter was large in simulations (increased focus, decreased Δz) the same behaviour could be found in measurement results.

It turned out that for lateral beam overlap an increase of the beam focus size seems to be more efficient than reduction of the lateral grid spacing which differs from the observations of [Bert et al., 2009]. They reported assuming a 5 % level of accepted local film blackening deviation for an 8 mm focus size and 2 mm lateral grid spacing (laOF= 4) an acceptable residual motion amplitude of 0.5 mm. Increasing the focus to 10 mm (laOF= 5) gained an acceptable residual motion of about 1.9 mm while decreasing the lateral grid spacing to 1 mm (laOF= 8) resulted in 2 mm allowed motion. In figure 3.10 in the simulations ($\Delta z = 3$ mm, 3 mm-RiFi) for an assumed acceptable standard deviation of 5 % and a lateral grid spacing of 2 mm changing the focus from 8 mm (laOF= 4) to 10 mm (laOF= 5) results in a change in accepted residual motion from 2.5 mm to 4 mm. The resulting acceptable motion values do not match since [Bert et al., 2009] did film measurements which can not generally be compared directly to ionization chamber dosimetry [Spielberger et al., 2003], but the tendency is comparable. In contrast for changing the lateral grid spacing (compare figure 3.7, simulations, $\Delta z = 3$ mm, 3 mm-RiFi) Δs from 3 mm to 2 mm while keeping a focus size of 10 mm (change of laOF from 3.3 to 5) even resulted in a slightly increased accepted residual motion (4 mm for $\Delta s = 3$ versus 4.5 mm for $\Delta s = 2$). Since different beam parameter settings were analyzed not directly the same combinations can be compared. But, anyhow, tendencies clearly seem to differ. Based on the here presented results one can conclude, that the overlap may not be the parameter to enlarge, but the beam focus. However, by doing so the increase of the penumbra has to be taken into account which is caused by a larger focus. This can be relevant in patient irradiations.

Longitudinally a reduction of the IES distance resulted in almost all cases in a more homogeneous dose distribution which was also observed by [Bert et al., 2009]. But in contrast to this work they did not study different ripple filters. However, an increased Bragg-peak width did not show any effect: The resulting slopes of linear fits increased very little compared to improvements which were observed for larger focus sizes in the lateral overlap investigation. Since this may be due to the little change in Bragg-peak width caused by the 2x3 mm-RiFi compared to the 3 mm-RiFi (compare figure 3.2) construction of a really larger ripple filter according to [Weber and Kraft, 1999], e. g. of 6 mm thickness, would be necessary to study effects of Bragg-peak width on motion robustness further.

A reason for the different conclusion compared to [Bert et al., 2009] might be that they separated lateral and longitudinal overlap in different investigations while in our case both effects could interact due to the 3D motion. An indication for that can be found in figure 3.13 where for increased focus not only the homogeneity gets better, but also deviations between homogeneities for different IES distances Δz get smaller.

Thus, the basic effects of the four beam parameters causing overlap were shown. To conclude clinical implications like a suggested gating window for a certain parameter combination treatment planning studies based on real patient data are more reliable. Therefore, these investigations should be continued using patient data to gain more concrete information about clinical recommendations. This is why the used analysis parameters, relative standard deviation and homogeneity index which both indicate homogeneity within the CTV, where chosen: basic focus was put on showing principle effects. In the other observed analysis parameters these were also seen, the homogeneity was affected most clearly.

Besides the here presented method to reduce interplay effects caused by residual motion within the GW other techniques are possible. [Furukawa et al., 2010a] combined gating with rescanning and used the latter technique for mitigation of the interplay effect. They investigated dosimetric influences on their mitigation technique also based on a similar array of pinpoint ionization chambers. Already four rescans showed significant increase of target homogeneity in their dosimetric study.

For both techniques the capability of mitigating residual motion effects was shown. A comparison between these two techniques with respect to under and over dosage as well as target conformity based on patient data would be interesting. Even a combination of both techniques can be a promising solution.

4 A breathing thorax phantom with 6D target motion

4.1 Introduction

As mentioned in chapter 2 for some treatment techniques dealing with moving tumours an appropriate motion monitoring system is mandatory. Since additional patient dose can be high while using fluoroscopy for direct tumour position determination [Shirato et al., 2004] it was proposed to apply surrogate signals to identify the motion state [Evans, 2008].

If a surrogate signal is used one has to ensure that the correlation between internal tumour motion and external motion signal is well known. Several groups compared surrogate signals to the real tumour motion based on patient data [Beddar et al., 2007; Gierga et al., 2005; Hoisak et al., 2006, 2004; Ionascu et al., 2007; Kanoulas et al., 2007; Liu et al., 2004; Otani et al., 2010; Tsunashima et al., 2004]. In some cases a good correlation was found, but some groups reported dependencies on patient, applied surrogate and reference points/marker positions. Phase shifts (time shifts) were observed as well as organ drifts due to muscle relaxation [Sonke et al., 2008; von M. Siebenthal et al., 2007a,b]. Studying patient data is necessary to gain the possibility of judging clinical relevance, but to estimate dosimetric effects of wrong correlation systematically proper phantoms are needed. Such a phantom can be very helpful for treatment plan validation and robustness analysis as well as for testing within technical development of new mitigation techniques or correlation models.

Depending on the studies which shall be done and the aspects which shall be focussed on, we defined criteria for the minimum functionality of the phantom (non-weighted order):

i) Anthropomorphic, breathing, deformable thorax comprising ribs

ii) Capability to perform 6D internal target motion (without deformation) independently from thorax motion

iii) Online adjustable correlation between internal target motion and external thorax motion

iv) Capability to start and stop target and thorax motion in any motion phase

v) Detector head representing the tumour equipped with multiple ionization chambers and films

vi) External motion applicable to surface imaging (e. g. the VisionRT system (Vision RT Ltd, London, UK)) and other systems like the Anzai belt (Anzai Medical Co.,Ltd, Tokyo, Japan) or RPM (Varian Real-time Position Management™ – Varian Medical Systems Inc., Palo Alto, CA)

vii) 4DCT compliance, e. g. no metal

viii) Extendable I/O signal interfaces, e. g. triggered motion start or beam gate output

ix) High flexibility, e. g. exchangeable detector head

Ribs (i) are necessary to have an inhomogeneous target introducing range changes. The phantom should be usable for correlation studies (ii,iii) including static (e. g. phase shift) and dynamic (e. g. baseline drift) correlation mismatches. This introduces the need of changing the correlation during irradiation. In addition, the target should be movable following any trajectory to introduce also real tumour motion taken e. g. from a 4DCT. Starting and stopping of target and thorax motion in any motion state (iv) is necessary to perform irradiation experiments with comparable starting phase or for 4DCT acquisition free of motion artefacts (motion hold in each scanned motion phase). To do dosimetric studies using heavy-ion irradiation volumetric dose measurements are needed to measure the interplay effect. Since films offer a very high spatial resolution, but are not very precise in terms of measuring absolute dose using ions [Spielberger et al., 2003], in addition to films multiple ionization chambers are needed within the moving target volume (v) [Karger et al., 1999, 2010]. Surrogate signals should be applied to the phantom as they would be in patient case (e. g. need of deformable thorax to enable use of the Anzai belt) and the phantom has to be 4DCT compatible in terms of motion detection and material (vi,vii). Finally, to trigger phantom motion e. g. to have a dedicated starting phase or to output a nominal gating signal the phantom should have I/O interfaces which should be as flexible as possible to cover also future needs. More general requirements for a 4D validation phantom were published by [Knopf et al., 2010].

There are a few commercial motion phantoms available e. g. by QRM (Sim4D+Thorax-Phantom – QRM GmbH, Moehrendorf, Germany), MODUS-QA (Qasar respiratory motion phantom – Modus Medical Devices Inc., London, CA), StandardImaging (Respiratory Gating platform – Standard Imaging Inc., Middleton, WI, USA), CIRS (Dynamic Thorax Phantom – CIRS Inc., Norfolk, VA, USA), and RSD (Dynamic Anatomical Respiring Humanoid Phantom – Radiological Support Devices Inc., Long Beach, CA, USA). Only the last two are capable of doing independent internal and external motion, but also these are not matching the requirements mentioned above (e. g. multiple ionization chambers).

This lack of commercial availability causes also other groups to build own phantoms: For example, [Alasti et al., 2006; Dietrich et al., 2005; D'Souza et al., 2005; Ford et al., 2003; Gemmel et al., 2010; Jiang et al., 2003; Keall et al., 2001; Rietzel et al., 2005] used a motion stage or moving arm to move radiopaque objects or detectors. Others went a more complex way by, in addition, introducing anthropomorphic structures or more complex motion [Followill et al., 2007; Kashani et al., 2007; Li et al., 2005; Nioutsikou et al., 2006; Serban et al., 2008; Vinogradskiy et al., 2009]. [Biederer and Heller, 2003] even built an artificial thorax to do breathing motion studies with real animal lungs.

All of these phantoms match one or more of the criteria mentioned above, but there is no phantom which would cover our needs completely. Thus, in the course of this work a phantom was designed, built and validated experimentally which covers the criteria mentioned above.

4.2 Materials and methods

4.2.1 The thorax

Basis of the artificial thorax is a commercial artificial skeleton (Skelett Bruce – Teng Long Trading GmbH & Co KG, St. Pölten, Austria) which consists of polyvinyl chloride (PVC). Everything but the thorax was removed and all metal components used by the manufacturer to connect the plastic bones (screws, wires, rods) were exchanged with plastic. After that the thorax was surrounded by rubber to generate a skin-surface and inter-rib material. Rather than using anthropomorphic materials that are bone/tissue equivalent, we chose to use a dedicated lookup table (LUT) to convert the Hounsfield units (HU) of the CT scan into water-equivalent path lengths (WEPL) for the use with particle irradiation [Jaekel et al., 2001].

4.2.2 The tumour (detector head)

The tumour is represented by a cube consisting of polymethyl methacrylate (PMMA) which provides slots for 20 pinpoint ionization chambers (PTW PinPoint® model 30009/30015 – PTW, Freiburg, Germany) and 5 light proof film cases covering radiographic films (detector head).

We decided to use radiographic films instead of gafchromic films, because the only available EBT2 films turned out to be not useful for homogeneity measurements using ions [Hartmann et al., 2010]. Therefore, light proof cases had to be constructed to cover small radiographic films (Kodak X-Omat V – Kodak GmbH, Stuttgart, Germany). These cases were made of black PVC plates of 1mm thickness. The plates were cut to a size of $(5 \times 7)\,\mathrm{cm}^2$. Then each of these was milled to generate space for a film of $(4.6 \times 6.8)\,\mathrm{cm}^2$ size. After that a second 5x7cm^2 sized plate of the same material was glued on top of the milled one.

The pinpoints are arranged in 4 rows with 5 chambers each, the films are mounted in between, in front of the first and behind the last row (BEV) (Figure 4.1(b)). The film cases can easily be replaced by nonirradiated ones. Reequipping of a set of 5 film cases is doable in less than 10 minutes in a dark room. The films were developed using a standard development machine

(Kodak X-Omat M35 – Kodak GmbH, Stuttgart, Germany; Agfa Curix 60 – Agfa-Gevaert N.V., Mortsel, Belgium).

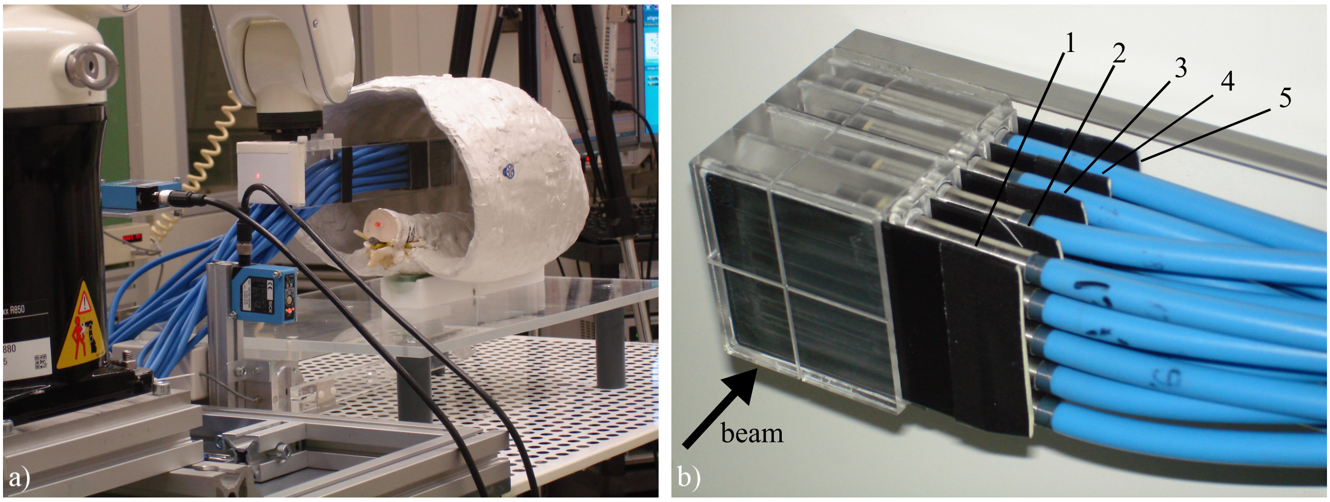

Figure 4.1.: Pictures of the detector head. **(a)** The detector head is shown in irradiation position within the artificial thorax. **(b)** Picture of the fully equipped detector head. 4 rows of pinpoint ionization chambers with 5 chambers per row are used for 3D dosimetry within the target volume. In between the rows, in front of the first and behind the last row light-proof film cases are placed (black plates) covering radiographic films.

By distributing 20 pinpoints within the maximum target volume of $(5 \times 5 \times 5)\,\mathrm{cm}^3$ 3D dose distributions can be measured. To have additional information on e. g. homogeneity with a higher spatial resolution the 5 radiographic films can be used. It has to be noted that films behind a certain pinpoint row are partially covered by the chambers. Therefore, the first film in BEV can be analysed completely while the last film has a much smaller undisturbed area.

4.2.3 Motion control

Thorax motion

A nylon cord which is attached to the sternum is periodically pulled and released by a stepping motor (AS1050 (200 full steps per revolution, micro step factor 64) – Beckhoff Automation GmbH, Frankfurt, Germany) via a lever arm (PMMA). This pulling results in contraction and deformation of the thorax and, therefore, introduces thorax motion. The stepping motor is placed at the edge of the base-plate (PMMA) to avoid having metal in the scanning field of the CT (Figure 4.1(a)).

The motor motion intrinsically is measured by an incremental encoder (1024 increments per revolution) and, in addition, by a laser distance sensor (Model OD100-35P840 – SICK AG, Waldkirch, Germany) which measures the distance to the moving lever arm.

Target motion

Motion of the detector head should be as flexible as possible to be able to simulate complex tumour motion. Therefore, the detector head was mounted to a robotic arm (KUKA KR 5 sixx R850 – KUKA Roboter GmbH, Augsburg, Germany) which was programmed to do motion synchronized to the thorax motion. The motion trajectory is defined by a list of N points $P_i\left(x, y, z, r_x, r_y, r_z\right), i = 1 \dots N$ which is executed periodically.

Target motion is intrinsically measured by the encoders of each robot axis and transformed to a 6D position information in Cartesian coordinates each 2 ms. In addition, the SI-motion (superior inferior) is measured using a second laser distance sensor.

Motion correlation

Thorax and robot motion are both controlled by the robot control system. The stepping motor is connected to a stepper control device which is integrated in a Beckhoff I/O system (extendable, programmable bus terminal system; see section 4.2.4). The stepper controller executes commands given by the robot controller in real time.

Due to technical constraints controlling fixed or defined varying correlations between thorax and target motion is divided into two phases: the pre- and the main-run. During the pre-run target and stepper velocities are calculated and synchronized based on the given P_i and the planned motion period T. In the main-run motion is periodically executed.

Constant phase shifts as well as phase drifts, i. e. an increase of a phase shift during motion, and base-line drifts, i. e. drifts of the target motion in inferior direction (x) during motion, can be performed. In addition, the robot control system can react on connected input signals which can be used to manipulate motion behaviour online (see also section 4.2.4).

4.2.4 I/O interfaces

Motion Logging

The analogue signals of the two laser distance sensors measuring the stepping motor motion and one projection of the target motion are directly provided and can be fed into an analogue to digital converter (ADC) to be logged to file. In our experiments we used a Beckhoff EtherCAT™-system (Beckhoff Automation GmbH, Frankfurt, Germany) in combination with a Windows PC. In addition, each 2 ms a logging data set $L_j(t) = \left(t_j, P_j\left(x,, y, z, r_x, r_y, r_z\right)\right)$ is written to an user datagram protocol (UDP) interface providing the current system clock counter t_j and the current position P_j. Using dedicated software on a Windows PC these position logging data can be written to file.

Remote control

Since entering an irradiation cave always takes time the robot software was implemented in a way that it can be controlled remotely. Remote access is realized using normal TCP/IP network interfaces and control PCs outside the cave. Only the change of film cases causes the need of entering the irradiation cave.

Multiple IO

The I/O device described in section 4.2.3 also provides 4 digital inputs and outputs for 24 V TTL signals and 12 digital inputs and outputs for 5 V TTL signals. These interfaces can be customized and are currently used to trigger motion start or feed status outputs into the data acquisition during measurement. In addition, it can in principle be used to gate the beam.

Figure 4.2 gives an overview how the components work together.

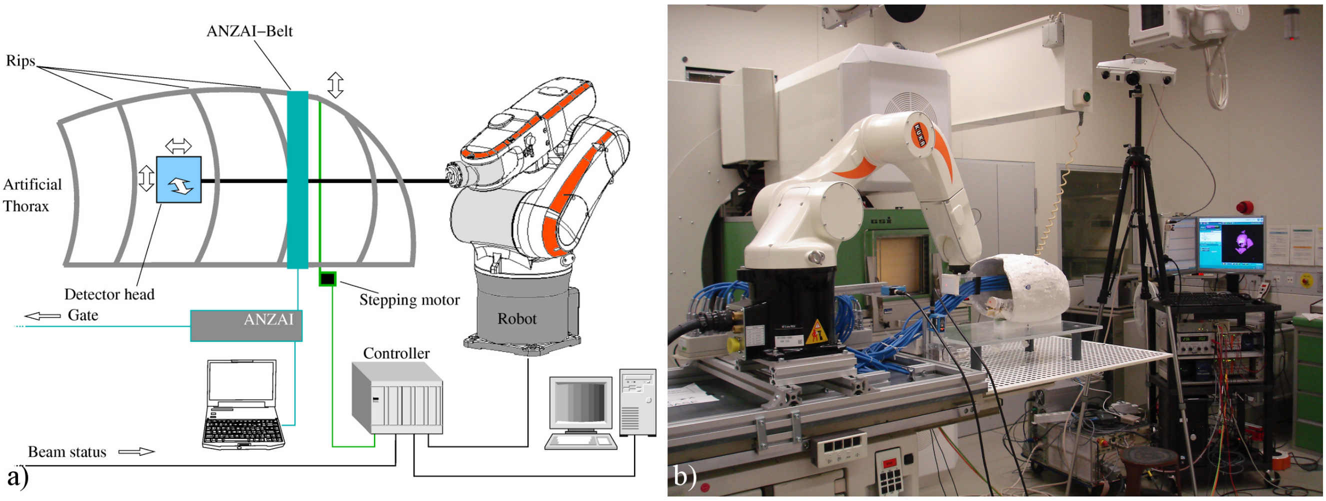

Figure 4.2.: **(a)** Sketch showing an overview of the phantom system: An artificial thorax including rips for generation of range changes is connected to a stepping motor in order to introduce thorax motion. An easily removable detector head is moved using a robotic arm in the right lung area of that thorax. As an example mounting of commercial motion monitoring systems is indicated by showing the ANZAI system in this sketch. **(b)** Photograph of the setup at GSI showing also the VisionRT system.

4.2.5 Validation experiments

Target motion (robot)

146 robot log files have been analyzed to determine precision of the robotic motion. In all these cases the robot was moved following a 3D sinusoidal trajectory defined as follows:

$$
\begin{aligned}
x(t) &= \frac{1}{2} \cdot A_{\mathrm{P}} \cdot \sin\left(\frac{2\pi}{T} t\right) \\
y(t) &= \frac{1}{4} \cdot A_{\mathrm{P}} \cdot \sin\left(\frac{2\pi}{T} t + \frac{\pi}{2}\right) \\
z(t) &= \frac{1}{4} \cdot A_{\mathrm{P}} \cdot \sin\left(\frac{2\pi}{T} t + \frac{\pi}{2}\right)
\end{aligned}
\tag{4.1}
$$

where the peak-to-peak amplitude A_{P} was varied from 2 mm to 20 mm and the period T was set to 3 s.

Based on the information in all motion log-files the 3D motion was compared to the nominal motion amplitudes and shapes.

Thorax motion

Thorax motion was evaluated with the VisionRT system. Since transient effects were expected due to the deformability of the thorax and potential extension of the cord several long-term tests were performed. Thorax motion was monitored for durations between 30 and 60 minutes. Reproducibility was tested by changing behaviour between different motion detection sequences: Motion was just stopped and restarted between two runs or the lever arm was shortly disconnected from the cord and reconnected prior to motion restart. In addition, the time between motion stop and restart was varied. During all these measurements the tracking point of the VisionRT system was set to the sternum.

Dosimetry

To allow treatment planning we performed 18 3D CT scans (Somatom Sensation Open – Siemens AG Healthcare, Erlangen, Germany), one for each motion state every 20 degrees distributed over one thorax motion cycle (The topogram and one axial slice are shown in figure 4.4). Thus we generated a 4DCT free of motion artefacts and a higher number of motion states than normally used for standard 4DCT reconstruction. To ensure having the right HU values we measured the WEPL of material samples using the PTW Peakfinder™ (PTW, Freiburg, Germany) and a 200 MeV/u carbon beam at Heidelberg Ion Therapy Center (HIT).

Figure 4.3 shows the basic principle of WEPL-measurements: Between two ionization chambers a water tank is varied in thickness. For each thickness the relative ionization measured with the two ionization chambers is acquired. Result is a depth-dose-distribution in water (Bragg-curve). This procedure is done with and without a sample in front of the measuring device. Inserting the sample results in a shift of the Bragg-peak (compare figure 4.3(b)). The WEPL is then calculated as follows:

$$\mathrm{WEPL} = \frac{\text{Bragg-peak shift}}{\text{geometrical thickness}} \tag{4.2}$$

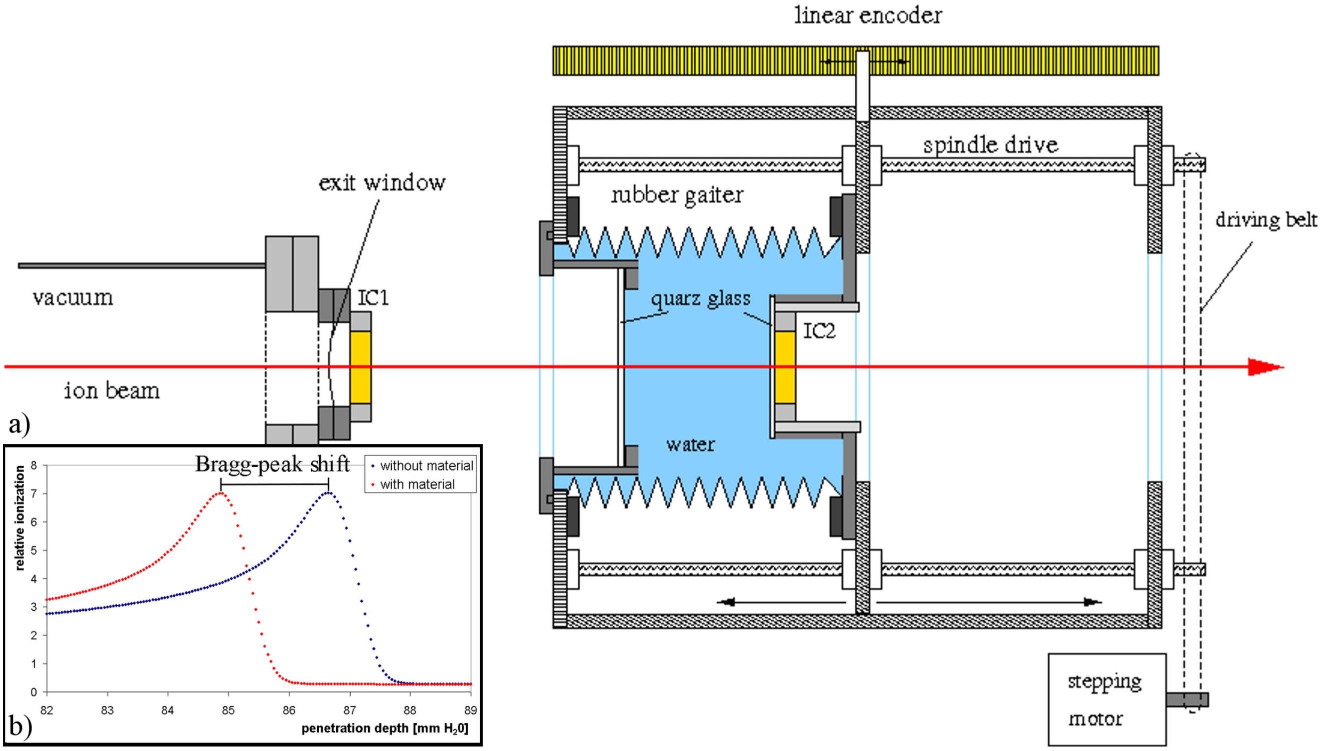

Figure 4.3.: Principle of WEPL-measurements. **(a)** Sketch of the water column of GSI which works comparable to the PTW Peakfinder™. Figure by courtesy of D. Schardt. **(b)** Example of a WEPL measurement: one Bragg-curve with and one without material in front of the measuring device.

To generate a CT appropriate for irradiation planning we replaced the HU values with the ones corresponding to the measured WEPL values [Jaekel et al., 2001].

For the dosimetric test based on the CT a plan was optimized to deliver a homogeneous dose of 1 Gy to a cubic target volume of the size of the detector head (figure 4.5) using a scanned carbon beam. This optimization was done for two plans one for irradiation of the pure detector head in air and one for irradiation of the detector head in the thorax. A bolus of 4 cm PMMA was used to have high enough energies for the optimization. Six types of irradiations were performed to investigate effects of the single components:

i) static detector head in air

ii) moving detector head in air

iii) static detector head in static thorax

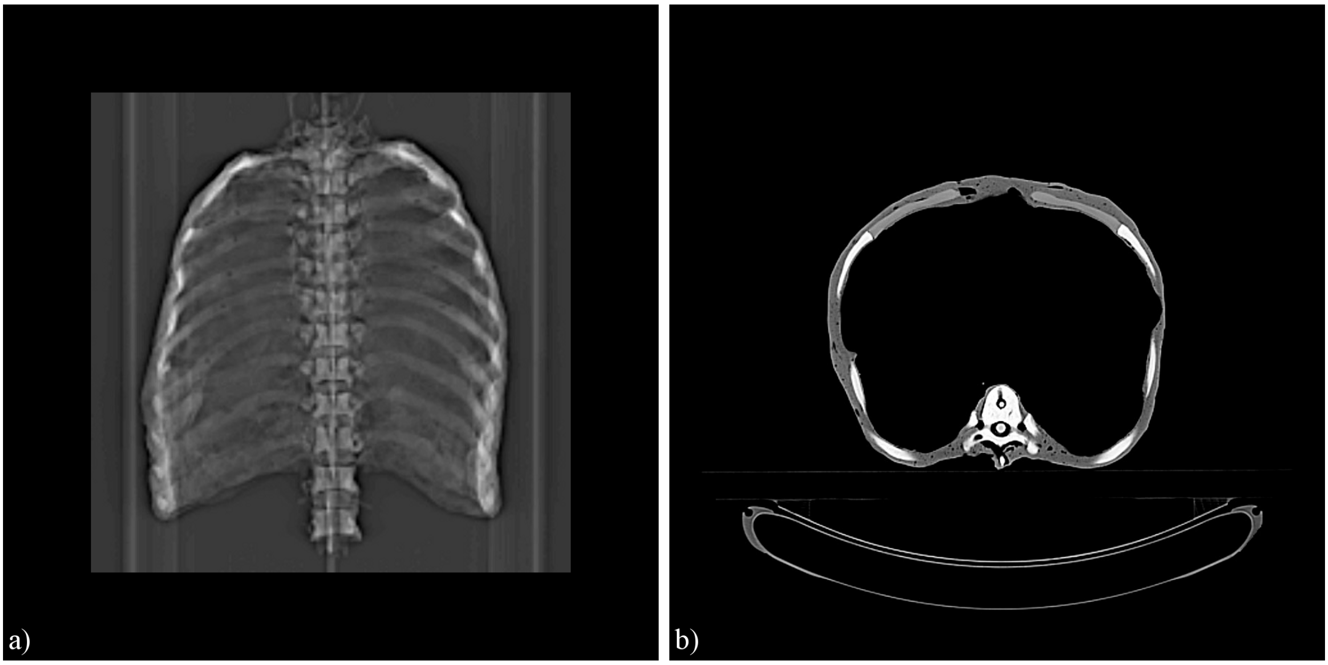

Figure 4.4.: CT scan of the thorax. **(a)** Topogram **(b)** Representative axial slice

iv) static detector head in moving thorax

v) moving detector head in static thorax

vi) moving detector head in moving thorax

The detector head was moved as described in (4.1) using a peak-to-peak amplitude A_P of 10mm and a period T of 3 s.

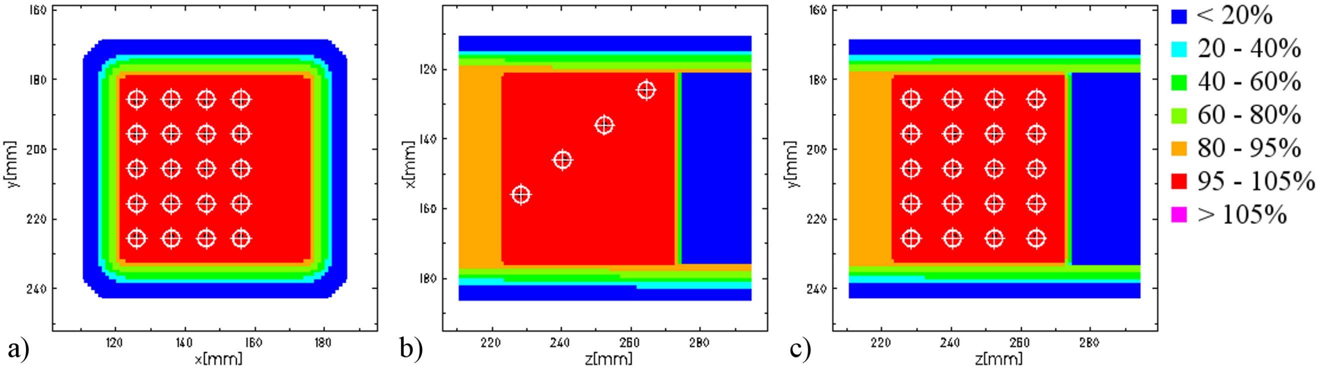

Figure 4.5.: Cuts through the calculated dose distribution of a stationary irradiation. The crosses indicate the measuring positions of the 20 ionization chambers (projected onto the particular cutting plane). **(a)** Beam's eye view, **(b)** view from the right hand side, **(c)** top view. In (b) and (c) the beam comes from the left

Furthermore, gated irradiation was tested using the ANZAI system to show baseline drift and phase shift functionality. The effect of a baseline drift was tested by comparing gated irradiation with $A_\mathrm{P} = 10\,\mathrm{mm}$ peak-to-peak motion and a gating window of 50 % combined with drifts of (0, 0.2, and 0.4) mm per period. In case of phase shift shifts between target motion and thorax motion of 0 and 90 degrees were introduced. Using these shifts a target moving with an peak-to-peak amplitude of $A_\mathrm{P} = 20\,\mathrm{mm}$ was irradiated using gating based on the external motion signal with a gating window of 25 %. The VisionRT system monitored the thorax motion in parallel using the sternum as tracking point location. Whereas the target point in the non-gated irradiations was set to the centre of the 3D motion, in the gating cases it was set to gating window centre (minimum of target motion – BEV most left position).

Measured doses were compared to the doses calculated using our in-house treatment planning system TRiP98 [Kraemer et al., 2000]. To compare also the interplay patterns measured in the moving cases 4D dose distributions were reconstructed based on beam delivery record, 4DCT and motion trace [Bert and Rietzel, 2007; Richter et al., 2010c, 2011]. Therefore, besides the automatically saved machine beam record the laser signals and the beam status signal were recorded using a Beckhoff EtherCAT system with 1 ms acquisition rate to have a temporal correlation between beam and motion. Additional signals (e. g. a Geiger counter output) were also logged in the same system to gather more information than essential to gain redundancy. Comparison was done according to treatment planning verification at GSI [Karger et al., 1999].

Since the dose gradients can be very steep agreement between measured doses and doses extracted from the calculated dose distribution is very sensitive on positioning errors. Therefore, the extraction positions were varied by ±2 mm and ±2°, respectively, in all 6 degrees of freedom around the nominal extraction position to estimate if a potential positioning error occurred. Since pinpoint ionization chambers measuring in high dose gradients can have a high uncertainty, in addition, comparison was also performed by excluding extraction values where the standard deviation of calculated doses within the sensitive volume of a chamber was larger than 2 cGy.

4.3 Results

4.3.1 Motion precision

Target motion (robot)

Figure 4.6 shows a comparison between logged and planned trajectory for two randomly chosen cases taken from the 146 robot log files which have been analyzed. In some small amplitude cases near the turning point small dips were observed (figure 4.6(e)). Results of the amplitude analysis can be found in table 4.1. In all cases the found amplitudes are systematically a little smaller than the planned ones which is due to the way the robot calculates its motion path in turning points. This deviation is less then 2 % in all measured cases. To check the shape of the logged trajectories each period of each log data was compared to sinusoidal curves with

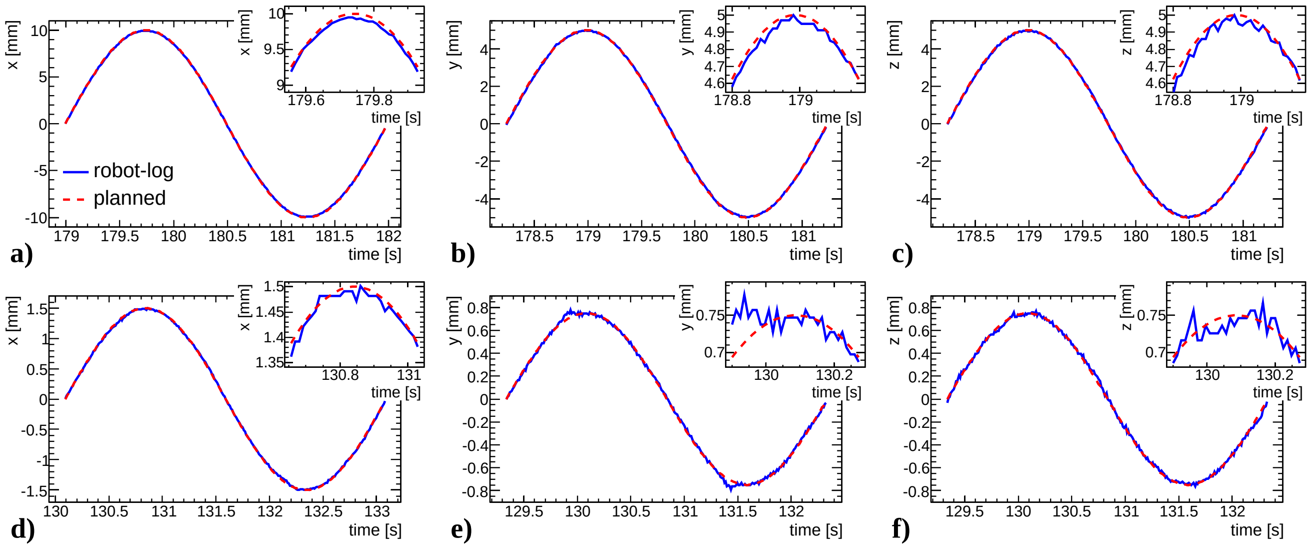

Figure 4.6.: Plots of two randomly chosen cases at random time for a small and a large amplitude. Shown is the planned (red line) and the logged (blue line) trajectory for one period in x, y and z. In the right top area of each plot a zoomed view to the maximum area is shown. **(a-c)**: $A_P = 20\,\text{mm}$ peak-to-peak motion in x. **(d-f)**: $A_P = 3\,\text{mm}$ peak-to-peak motion in x.

amplitudes adjusted to the measured ones. It was found that in all cases the logged trajectories differ from a perfect sine by $(0.00 \pm 0.09)\,\text{mm}$.

The periods derived from the maxima positions in all log files were found to be (3000±3) ms.

Thorax motion

VisionRT data showed in some cases a transient effect in the thorax motion. Depending on the time the thorax was not moved before starting a new measurement this effect which results in a shift of signal base line lasts between a few seconds up to about 500 s. By then thorax motion turned out to be very constant.

Figure 4.7 shows as an example a comparison of VisioNRT measurements of the thorax motion after a very long (12 h) and a very short (10 s) pause between two thorax motions. One can see the much longer base line drift after a long pause. The spikes at the beginning and the end of the measured trajectories are due to slight wobbling of the camera tripod which was caused by entering and leaving the room, respectively. For realistic pauses of a few minutes (in our dosimetry tests) we observed a signal drift of up to 20 % (relative to tracking point motion amplitudes of about 2 mm). After up to 60 s the thorax motion stayed stable.

Table 4.1.: Results of the amplitude analysis. For each planned pea-to-peak amplitude A_P the number of cases N, the mean measured amplitude $A^{\mathrm{mean}}_{\mathrm{M},i}$ and the maximum deviation between measured and planned amplitude $\Delta A^{\mathrm{max}}_{\mathrm{P-M},i}$ is given for all three translation directions $i = x, y, z$. The measured amplitudes $A_{\mathrm{M},i}$ were compared to the actual planned amplitudes $A_{\mathrm{P},i}$ which result from (4.1): $A_{\mathrm{P},x} = A_\mathrm{P}$, $A_{\mathrm{P},y} = A_{\mathrm{P},z} = \frac{1}{2} \cdot A_\mathrm{P}$.

A_P	N	$A^{\mathrm{mean}}_{\mathrm{M},x}$	$\Delta A^{\mathrm{max}}_{\mathrm{P-M},x}$		$A^{\mathrm{mean}}_{\mathrm{M},y}$	$\Delta A^{\mathrm{max}}_{\mathrm{P-M},y}$		$A^{\mathrm{mean}}_{\mathrm{M},y}$	$\Delta A^{\mathrm{max}}_{\mathrm{P-M},z}$	
[mm]		[mm]	[mm]	[%]	[mm]	[mm]	[%]	[mm]	[mm]	[%]
2	4	1.991	0.01	0.5	1.013	−0.02	−2.0	0.983	0.02	2.0
3	16	2.983	0.02	0.7	1.496	0.01	0.7	1.491	0.02	1.3
4	5	3.984	0.03	0.8	1.994	0.01	0.5	1.986	0.03	1.5
5	15	4.975	0.03	0.6	2.485	0.02	0.8	2.470	0.04	1.6
6	5	5.966	0.04	0.7	2.990	0.01	0.3	2.972	0.03	1.0
7	14	6.964	0.05	0.7	3.470	0.03	0.9	3.468	0.04	1.1
8	2	7.960	0.04	0.5	3.955	0.05	1.25	3.960	0.04	1.0
10	19	9.943	0.06	0.6	4.978	0.03	0.6	4.972	0.05	1.0
20	69	19.878	0.14	0.7	9.960	0.06	0.6	9.953	0.08	0.8

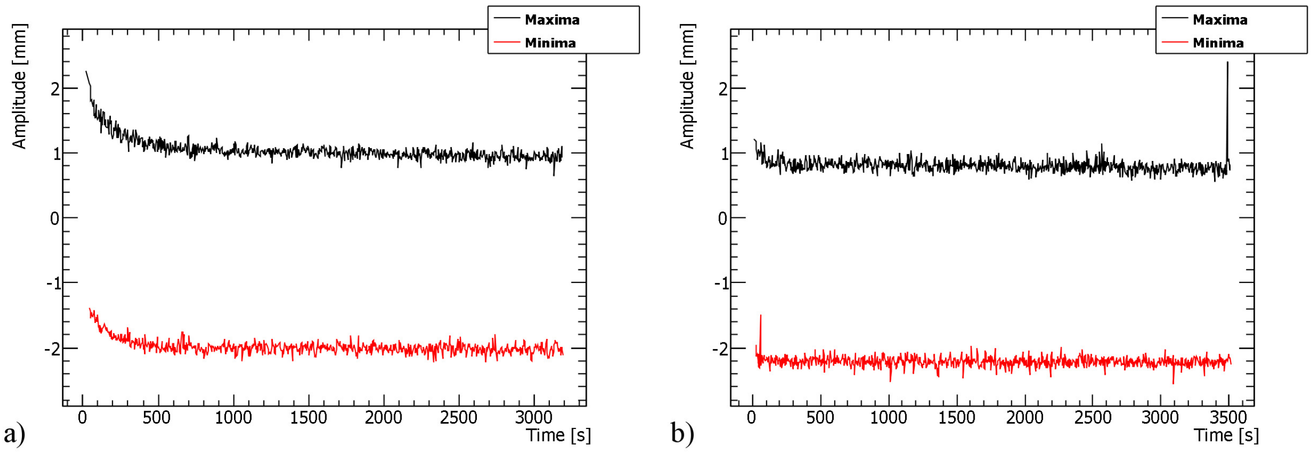

Figure 4.7.: Long term VisionRT measurements of the thorax motion. The detected maxima (black line) and minima (red line) of the measured trajectories are plotted over time. **(a)** Motion has been started 12h after the last one was stopped. **(b)** Motion has been started right after the last one was stopped.

4.3.2 Irradiation experiments

WEPL results

Table 4.2 gives the results for the measured WEPL of four used materials: the PVC bones are made of, rubber which was used to build the inter-rib material, a different PVC the film-cases consist of, and a radiographic film.

Table 4.2.: Results of water-equivalent path length (WEPL) measurements of phantom material.

Material	WEPL	
	Value	Uncertainty
PVC: bony anatomy	1.00	0.02
Rubber: inter-rib material	1.06	0.02
PVC: film cases	1.25	0.09
Kodak X-Omat V film	1.60	0.71

In table 4.3 Bragg-peak shifts of equipped and empty film cases are given. For comparison also the thickness of one film is written. Even if only 5 film cases are inserted into the detector head, more cases were built to be able to exchange them fast during measurements. The number in the first column corresponds to the ID of the measured film case.

Table 4.3.: Results for measured Bragg-peak shifts of empty and equipped film cases. In addition, the value for one Kodak X-Omat-V film is given.

Film case ID	Content	Bragg-peak shift [mm]	
		Value	Uncertainty
#2	equipped	2.03	0.07
#5	equipped	1.96	0.07
#12	equipped	2.02	0.07
#16	equipped	1.92	0.07
#15	empty	1.82	0.07
#17	empty	1.77	0.07
#23	empty	1.78	0.07
#25	empty	1.75	0.07
Kodak X-Omat V film		0.24	0.07

Film results

Figure 4.8 shows as an example two sets of irradiated films which were put into the detector head during the dosimetric test experiments. The upper row shows a static case the lower row a moving case. The films are numbered as they were placed in the detector head in beam direction. The static case shows a very homogeneous blackening while an interplay pattern can

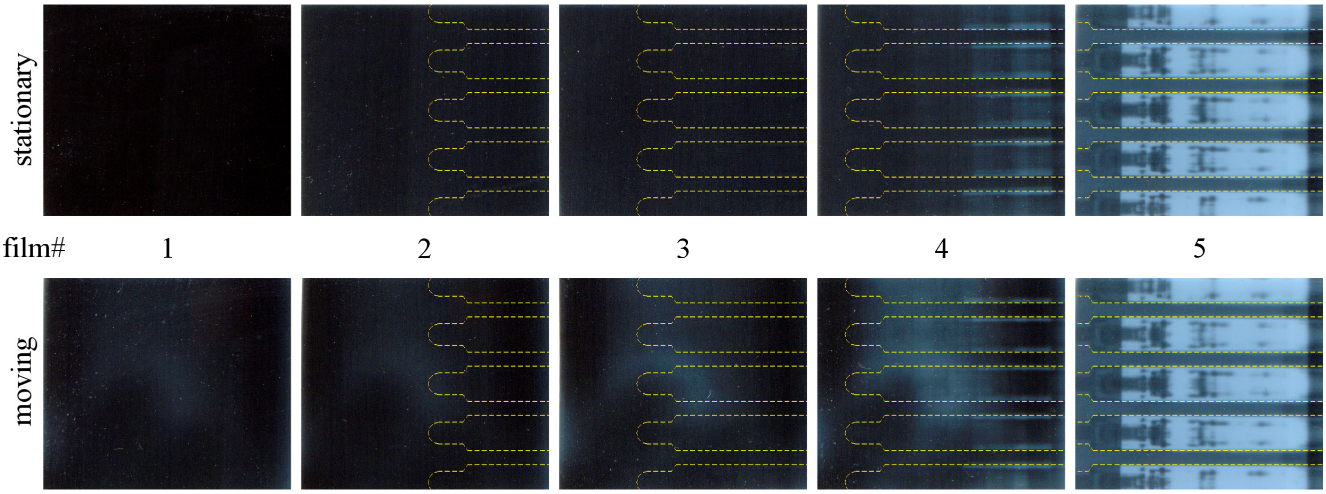

Figure 4.8.: Two film sets irradiated using a scanned carbon beam within the detector head. Upper row: stationary case showing very homogeneous blackening. Lower row: moving case showing an interplay pattern. The film number specifies the position in the detector head (compare figure 4.1(b)). The yellow contours indicate the pinpoint positions of the row in front of a certain film. The shadow of the pinpoint ionization chambers can be seen in the more distant films.

be seen in the moving case. Because the films are in part covered by the pinpoint ionization chambers one can see shadows of the chambers on the more distal positioned films.

Dose results

As an example figure 4.9 shows a recalculated interplay pattern. It confirms the assumption mentioned above. Sharp gradients at least in left-right direction (x) can be seen causing high sensitivity of dose agreement between measurement and calculation on setup errors. Shifting and rotating of the extraction position within the calculated dose distribution resulted in a clear minimum in dose deviation only for a shift in x and for two angles (rotation around y and z axis) ($\Delta x = 1.1\,\mathrm{mm}$, $\Delta r_y = 0.2°$, $\Delta r_z = -0.2°$). In table 4.4 the measured doses and the deviations from the planned dose are given. Table 4.5 shows the results for comparison between measured and calculated doses relative to the measured doses.

Base line drift

An overview of all the measured signals using the Beckhoff EtherCAT system can be seen in figure 4.10. The target motion drifts to lower values (corresponding to the beam's eye view right direction) while the thorax motion stays constant. It can also be seen that within a certain "beam available gate" the beam is delivered in pulses (slope of Geiger counter signal) within the gating windows only.

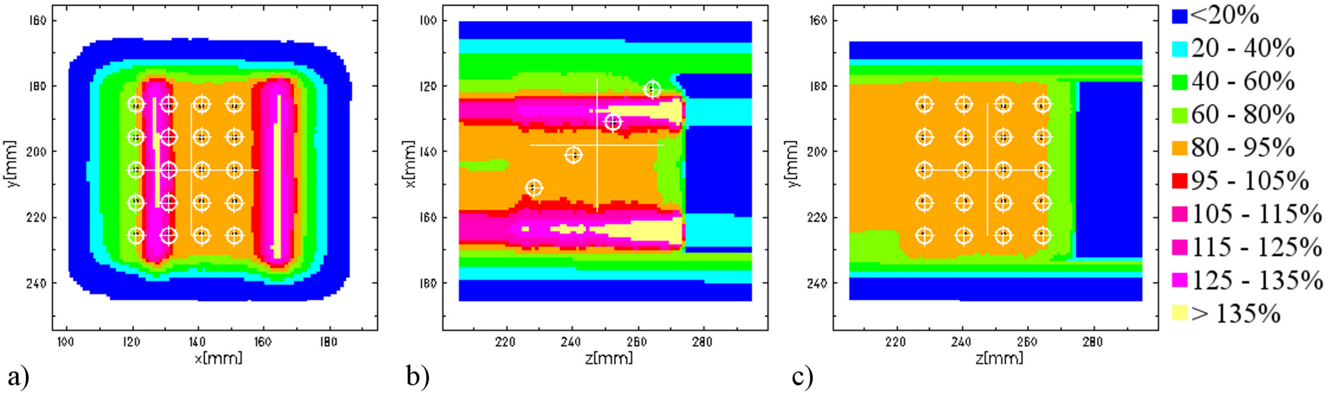

Figure 4.9.: Exemplary plot of cuts through the recalculated dose distribution of an interplay (case #2 in table 4.5). The crosses indicate the measuring positions of the 20 ionization chambers (projected onto the particular cutting plane). **(a)** Beam's eye view, **(b)** view from the right hand side, **(c)** top view. In (b) and (c) the beam comes from the left. The interplay pattern shows sharp gradients in x (left-right) direction.

Table 4.4.: Results of measured doses compared to planned dose of 1 Gy.

#	Setup	Target	Thorax	D_M [Gy]		$D_\mathrm{M-P}$ [%]	
				Mean	SD	Mean	SD
1	Detector head only	Static	–	0.99	0.01	−0.9	0.8
2	Detector head only	Moved	–	0.93	0.05	−7.5	5.4
3	Phantom	Static	Static	0.99	0.01	−1.2	0.9
4	Phantom	Static	Moved	0.99	0.01	−1.3	1.0
5	Phantom	Moved	Static	0.99	0.10	−0.7	10.0
6	Phantom	Moved	Moved	0.90	0.18	−10.5	17.7

Table 4.5.: Results of measured doses compared to extracted ones from calculated dose distributions (mean ± standard deviation). Columns 5 and 6 show results extracted at the nominal position while in columns 7 and 8 results with shifted/rotated extraction point are reported ($\Delta x = 1.1\,\mathrm{mm}$, $\Delta r_y = 0.2°$, $\Delta r_z = -0.2°$). For the results in column 6 and 8, in addition, only extracted values were considered having less than $2\,\mathrm{cGy}$ standard deviation of dose within the sensitive volume.

#	Setup	Target	Thorax	Relative deviations from calculations [%]							
				Nominal position				Corrected position			
						$SD_\mathrm{D} \leq 2\,\mathrm{cGy}$				$SD_\mathrm{D} \leq 2\,\mathrm{cGy}$	
				Mean	SD	Mean	SD	Mean	SD	Mean	SD
1	Detector head only	Static	–	1.0	1.0	1.0	1.0	0.9	0.9	0.9	0.9
2	Detector head only	Moved	–	−4.4	9.9	−0.4	1.8	1.6	3.3	−1.3	2.6
3	Phantom	Static	Static	1.3	1.0	1.3	1.0	1.2	1.0	1.2	1.0
4	Phantom	Static	Moved	0.6	1.4	1.1	1.2	1.0	1.0	1.0	1.0
5	Phantom	Moved	Static	1.7	7.9	1.0	7.6	1.2	5.8	0.0	4.7
6	Phantom	Moved	Moved	0.8	7.0	0.8	7.0	1.2	5.1	0.6	4.5

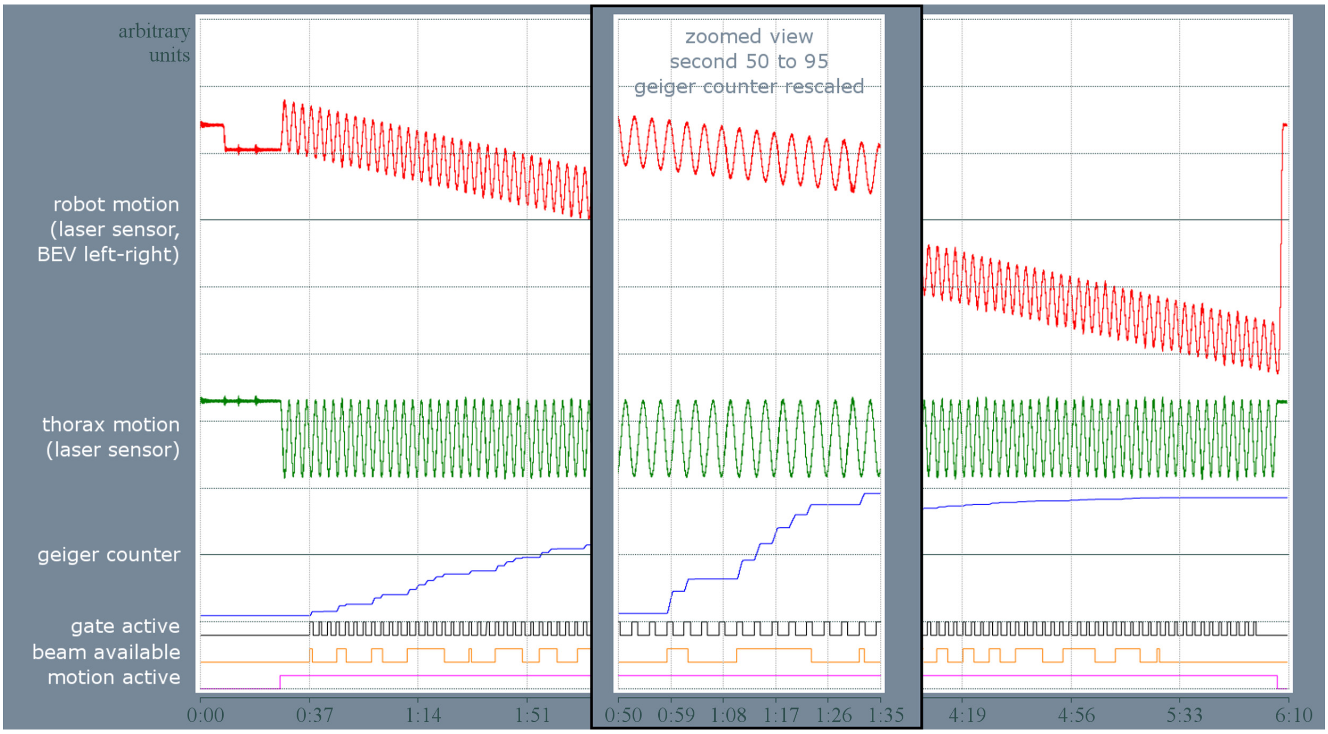

Figure 4.10.: Measured signals using the Beckhoff EtherCAT system.

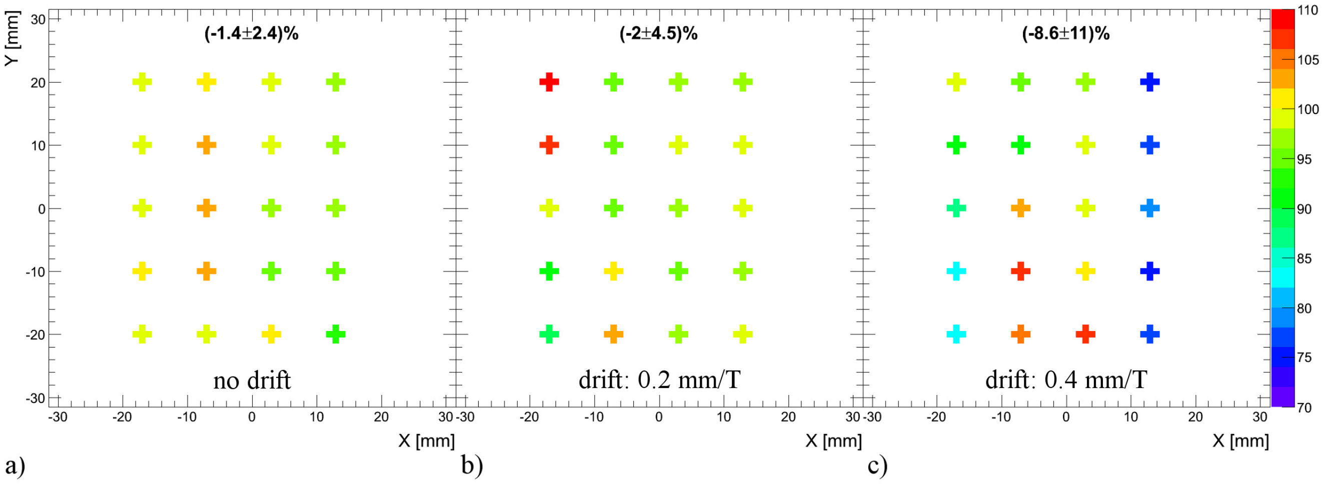

Figure 4.11.: Measured doses of the 20 pinpoint ionization chambers in beam's eye view (BEV) projection. Values are normalized to the doses measured in the stationary case. In the top centre of each plot the mean deviation and its standard deviation are listed. **(a)** Interplay without drift. **(b)** Base line drift with 0.2 mm per period. **(c)** Base line drift with 0.4 mm per period. Drift direction was BEV to the right (x).

Figure 4.11 shows exemplarily the results of the doses for the base line drift measurements. It can be seen that in case of a large base line drift the dose in the chambers placed at the most right leave at some point the target volume and get less dose.

Phase shift

Analysis of the measurements done using the Beckhoff EtherCAT-system (see also figure 4.10) showed that the phantom was able to perform shifts between thorax and target motion. For the two applied phase shifts dose deviations of $(2.4 \pm 4.0)\,\%$ (0° phase shift) and $(2.7 \pm 3.3)\,\%$ (90° phase shift) relative to the stationary measurements were found.

4.4 Discussion

4.4.1 Phantom construction

The presented phantom has anthropomorphic structure in terms of bony anatomy and water equivalent inter-rib material and thoracic shape as done by some groups found in literature. While in our phantom the lungs are filled with air, [Nioutsikou et al., 2006] and [Vinogradskiy et al., 2009] introduced sponges to represent lung equivalent material. [Serban et al., 2008], in addition, modelled substructure like bifurcations into the lung sponge. [Biederer and Heller, 2003] even used a real lung. Usage of real organs is not very handy for systematic studies which may take longer time since durability is limited and exchange of the organ results in the need of a new 4DCT. Realistic substructures and tumour composition also makes usage for 3D dosimetry and complex tumour motion difficult. Therefore, we reduced complexity for the inner thorax structure to a minimum to focus on correlation and complex target motion. Introduction of sponge as a lung tissue may be done in a second, improved version of the phantom.

In contrast, bony anatomy which only exists in a few phantoms in literature is important for our needs to have range changes. [Kashani et al., 2007] combined realistic bony structure and internal composition, but the thorax can not breath which is important to enable usage of external motion sensors like the ANZAI belt as they would be used in patient case. There is one commercial phantom capable of doing thorax deformation according to breathing: the Dynamic Anatomical Respiring Humanoid Phantom by RSD (Radiological Support Devices Inc., Long Beach, CA, US) uses compressed air for breathing and target motion, but it is only capable of doing 1D motion.

Most phantoms used are only capable to do 1D or 2D target motion. [Serban et al., 2008] and [Nioutsikou et al., 2006] introduce a 3D motion to their target (tumour) by pushing an artificial diaphragm. This motion is reproducible, but not predictable/adjustable. [Nioutsikou et al., 2006] constructed a phantom capable of 3D motion following regular or even irregular trajectories, but target rotations can not be incorporated to the motion trajectories and the phantom is not able to perform external thorax motion which both can be done with the presented phantom. There are two commercially available systems providing 3D internal and 1D external motion: the Qasar Respiratory Motion Phantom (Modus Medical Devices Inc., London, CA) and the Dynamic Thorax Phantom (CIRS Inc., Norfolk, VA, USA). Only the last one can perform the motion independently, but the use of e. g. an ANZAI belt is not possible since external motion is realized by an up-and-down moving platform (Only the ANZAI laser could be used or e. g. the Varian RPM) and, thus, is not patient like. In addition, the correlation can not be adjusted during measurement and 3D dosimetry using multiple ionization chambers is not possible with these two systems.

Dosimetry in reported phantoms is done using thermo luminescent dosimeters (TLDs), radiographic or radio chromic films or ionization chambers. TLDs can not be used for precise interplay measurements since their dose response depends on LET [Avila et al., 1999; Horowitz, 1990; Horowitz and Stern, 1990] and energy [Besserer et al., 2001; Bilski et al., 1997]. In addition, they have to be analysed offline. Films are used by several groups. [Nioutsikou et al., 2006] even used several films to measure the 3D dose distribution within the target, but without incorporating ionization chambers. If ionization chambers are used only one chamber is placed in the moving target which is not enough to measure interplay patterns using ions. Ionization chamber stacks are reported by [Karger et al., 1999] and [Lomax et al., 2004] in conjunction with static dose verification measurements at GSI, HIT and Paul Scherrer Institute (PSI, Villigen, Switzerland). In these cases the pinpoint ionization chambers are put into water while in our case they are tight surrounded by PMMA.

Thus, the phantom presented here differs from all commercial available phantoms and those presented in literature mainly in two characteristics: Correlation of deformable breathing thorax with a target movable in six degrees of freedom and usage of a combination of multiple ionization chambers and multiple films for target dose measurements. In addition, it is capable of triggering external systems (like gating the beam) or being triggered to start moving in a certain motion state.

4.4.2 Validation experiments

Target motion turned out to be very precise in both timing and positioning. Reproducibility is better than reported by [Serban et al., 2008] and [Kashani et al., 2007] which is not surprising if using a robotic system. Trajectory amplitudes are about 2% less than the planned ones but since this is a systematic and reproducible behaviour by planning for a little larger amplitude than the aimed one even higher precision can be gained.

Thorax motion showed base line drifts directly after motion start due to transient effects. Since this effect is dependent on the time between two motion sequences, it can easily be overcome by ensuring that the motion pauses in between two measurements are short and motion is started prior to the measurement according to the pause. For usual pauses of a few minutes between two irradiation experiments we found that it is sufficient to start motion 60 seconds prior to the irradiation. However, for some experiments it may be necessary to start motion in a certain motion phase synchronously with the irradiation. In this case the base line drift of thorax motion can be minimized by keeping pauses between irradiations short. In addition, effects of that base line drift on the dose result are expected to be small: Results for case number 4 (moved thorax, static target) in table 4.4 are in good agreement with the results of the two stationary cases number 1 and 3. Thus, motion of the thorax does not have an effect on dose measured in a static target at least for the chosen target volume. Due to the thorax motion adaption the thorax gets compressed in anterior-posterior direction. Therefore, the inhomogeneous material in front of the target moves mainly in the beam's direction. In addition, motion is small (sternum moves a few millimetre). Therefore, dosimetric effects of thorax motion only were expected to be small. In addition, the target volume compared to the ionization chamber positions is not very sensitive for small range changing motion. Dosimetric effects of thorax motion only may be larger once foam is introduced as lung material.

Up to now thorax motion shape can not be changed. To introduce more realistic signals for external motion sensors it is planned to exchange the controller of the Beckhoff I/O device by a more intelligent one which then may take over parts of the stepper motion control triggered by the robot control system.

WEPL results of bone-PVC and inter-rib material turned out to be comparable to water. Since ribs were introduced to generate range changes a higher WEPL compared to the inter-rib material would be better. Since rubber is also covering the ribs and, therefore, the absolute thickness of the phantom wall is higher at a rib compared to an inter-rib region, the desired effect of introducing range changes is yet accomplished. In addition, Bragg-peak shifts of empty and equipped film cases differ by the shift resulting from one film which is reasonable.

Comparison of measured and calculated doses show very good agreement at least for position corrected dose extraction. Setup errors based on positioning lasers of 1.1 mm lateral and 0.2° in two angles reasonable. The found deviations are acceptable since [Karger et al., 2010] reported expected uncertainties of up to 3 % for static dose measurements which can be even higher if inhomogeneous material comes into play. Ignoring ionization chambers within high dose gradients is common practise in dose verification experiments but there is no threshold or recommendation published. The results show that ignoring pinpoint ionization chambers based on a gradient criterion gains better agreement between calculation and measurement. Since this agreement is also acceptable for the results where all 20 pinpoints were included into the comparison the phantom turns out to be usable for dosimetric studies.

Base line drift results show consistently that the phantom is able to shift the target during irradiation. For the larger of the both measured drift velocities the target finally leaves the target volume. This is why results show a clear under dosage in the most right ionization chamber row.

Phase shift results showed that the phantom is able to apply shifts between thorax and target motion. Dosimetric results get worse for an applied shift of 90 degrees compared to a shift of 0 degrees which is reasonable.

5 Evaluation of two respiratory motion sensors

5.1 Introduction

Essential for motion synchronized irradiation is obviously knowledge about the current target position. Therefore, appropriate motion monitoring systems have to be used which are able to detect the current tumour position in real-time.

One possibility is to monitor internal motion directly using fluoroscopy [Shirato et al., 2000a,b], ultrasound [Kolen et al., 2004] or electro-magnetic tracking of internal markers [Seiler et al., 2000]. Fluoroscopy introduces additional dose to the patient [Shirato et al., 2004]. Ultrasound is for some sites not usable as a direct motion monitor (e. g. lung due to total reflection) and it needs high skilled interpretation [Evans, 2008]. Finally, internal markers are highly invasive and introduce uncertainties for treatment planning and beam delivery using intensity modulated particle therapy (IMPT) [Bert and Durante, 2011]. Because of these drawbacks several groups investigated methods to monitor target motion indirectly with the aid of a surrogate signal correlated to breathing motion [Evans, 2008].

Several types of surrogate signals have been under investigation: ultrasound monitoring e. g. the diaphragm [Xu and Hamilton, 2006], spirometry [Zhang et al., 2003], infra-red reflecting markers [Keall et al., 2006], infra-red emitting markers [Schweikard et al., 2004], a laser distance sensors [Tsunashima et al., 2004], breath temperature [Kubo and Hill, 1996], a strain gauge [Lu et al., 2006b], a pressure sensor [Li et al., 2006] or surface imaging [Hughes et al., 2009].

Commercially available realizations of the last two types are available at the University Clinic Heidelberg (UCHD): the Anzai system (RGS AZ-733V – Anzai Medical Co.,Ltd, Tokyo, Japan) and the VisionRT system (AlignRT®/GateRT®– VisionRT Ltd., London, UK). The Anzai system consists of a gating control system (GCS) which can be used with a belt comprising a pressure sensor or a LDS as motion detection system. The VisionRT system uses a stereoscopic camera measuring the thorax surface motion in 3D based on image reconstruction by dedicated software (AlignRT® or GateRT®). A region of interest (ROI) at a certain tracking point can be tracked to get the motion signal on which gating can be based (using GateRT®). The signal quantifies surface motion along the normal vector of the ROI.

Aim of this work was to determine which of these two (external) motion monitoring systems would be "better" with respect to applicability for gated patient irradiations at HIT. [Kubo and Hill, 1996] phrased how the "better" sensor has to be characterized when they evaluated different motion sensors with respect to their usability for gating. This work focuses on two important characteristics mentioned by [Kubo and Hill, 1996]: processing speed and reliability. Thus, we defined two criteria the comparison of the Anzai system and the VisionRT system should be based on:

i) Gating delays (potentially shifts of the planned gating window)

ii) Correlation of internal motion and motion surrogate

Delays of the actually sent gating window compared to the planned one (i) result in an unwanted phase shift with potential bad implications on the dose distribution. To our knowledge there is no publication on gating delays of the two systems. Only in the newest manual by Anzai a maximum delay of 175 ms is reported [Anzai, 2011]. Such a delay can cause shifts of a gating window by e. g. 21° assuming a breathing period of 3 s. Observed tumour motion periods vary between 2.7 s and 6.6 s [Neicu et al., 2003; Seppenwoolde et al., 2002; von M. Siebenthal et al., 2007a].

A good correlation between an external motion detection system and internal tumour motion (ii) is essential if the external system shall be used as surrogate for the internal motion. Different groups studied this correlation for different systems: [Koch et al., 2004; Liu et al., 2004] and [Gierga et al., 2005] evaluated the correlation of skin motion to internal target motion. [Koch et al., 2004; Liu et al., 2004] based their study on magnetic resonance imaging (MRI) while [Gierga et al., 2005] tracked radiopaque markers with kV-fluoroscopy. [Beddar et al., 2007; Ionascu et al., 2007; Kanoulas et al., 2007] and [Tsunashima et al., 2004] compared one commercial external motion sensor against internal motion using 4DCT [Beddar et al., 2007] and kV-fluoroscopy, respectively. [Ionascu et al., 2007] used a laser distance sensor (LDS) (LB-300, KEYENCE Corporation, Osaka, Japan), [Kanoulas et al., 2007] and [Tsunashima et al., 2004] investigated the Anzai system (laser) and [Beddar et al., 2007] analyzed the Real-time Position Management™ (RPM) system (Varian Medical Systems Inc., Palo Alto, CA). Two groups compared two different motion sensors. [Hoisak et al., 2006, 2004] evaluated the correlation of the signals of a spirometer and an electro-magnetic tracking system (Ascension Technologies, Burlington, VT, USA) against target motion acquired with kV-fluoroscopy. [Otani et al., 2010] compared the RPM system with the Anzai system with respect to correlation based on 4DCT data.

The method for internal motion detection in most cases is kV-fluoroscopy. Since this introduces additional dose to the patient [Shirato et al., 2004] we decided to use the irradiation exiting the patient during conventional photon therapy detected with an electronic portal imaging device (EPID) (MV-fluoroscopy) even if a drawback has to be taken into account:

MV-fluoroscopy data shows inferior image quality compared to kV-fluoroscopy. Especially the contrast is worse because for photon energies commenly used for MV-fluoroscopy the photon absorption coefficient of dissimilar tissues differs less than for lower energies. However, [Meyer et al., 2006; Richter et al., 2010a; Wilbert et al., 2008] showed that it is possible to track tumour motion based on MV imaging.

To our knowledge there is no publication comparing the Anzai system against the VisionRT system. The Anzai system has been used by several groups. For instance, [Li et al., 2006] compared this system to the RPM system based on the correlation score. Amongst others the same quantity was used by [Hughes et al., 2009] to compare the VisionRT system against spirometry, which is the only paper so far investigating the VisionRT system with respect to gating.

5.2 Material and methods

5.2.1 Gating delays

For both motion monitoring systems gating measurements have been performed. Both systems were configured to send a gate signal based on motion of the robotic arm which is described in more detail in chapter 4 for a gating window GW of 50 %. Two series of measurements have been done, one for each motion monitoring system. The setups for the two cases are shown in figure 5.1.

In case of the Anzai system the robot was moved along a 3D trajectory which can be parameterized as follows:

$$\begin{aligned} x(t) &= \frac{1}{2} \cdot A \cdot \sin\left(\frac{2\pi}{T_t} t\right) \\ y(t) &= \frac{1}{4} \cdot A \cdot \sin\left(\frac{2\pi}{T_t} t + \frac{\pi}{2}\right) \\ z(t) &= \frac{1}{4} \cdot A \cdot \sin\left(\frac{2\pi}{T_t} t + \frac{\pi}{2}\right) \end{aligned} \tag{5.1}$$

with a peak-to-peak amplitude A of 20 mm and a period T_t of 3 s. A reflective plate was mounted at the robotic arm. The motion of the plate (x-direction) was measured using the laser of the Anzai system and with an additional LDS (Model OD100-35P840 – SICK AG, Waldkirch, Germany; acquisition rate: 1 kHz). 13 measurements have been performed with a duration of 3 min to 6 min (59 to 105 gates amplitude based). The Anzai system was asked to output a gate signal between 50 % exhale and 50 % inhale.

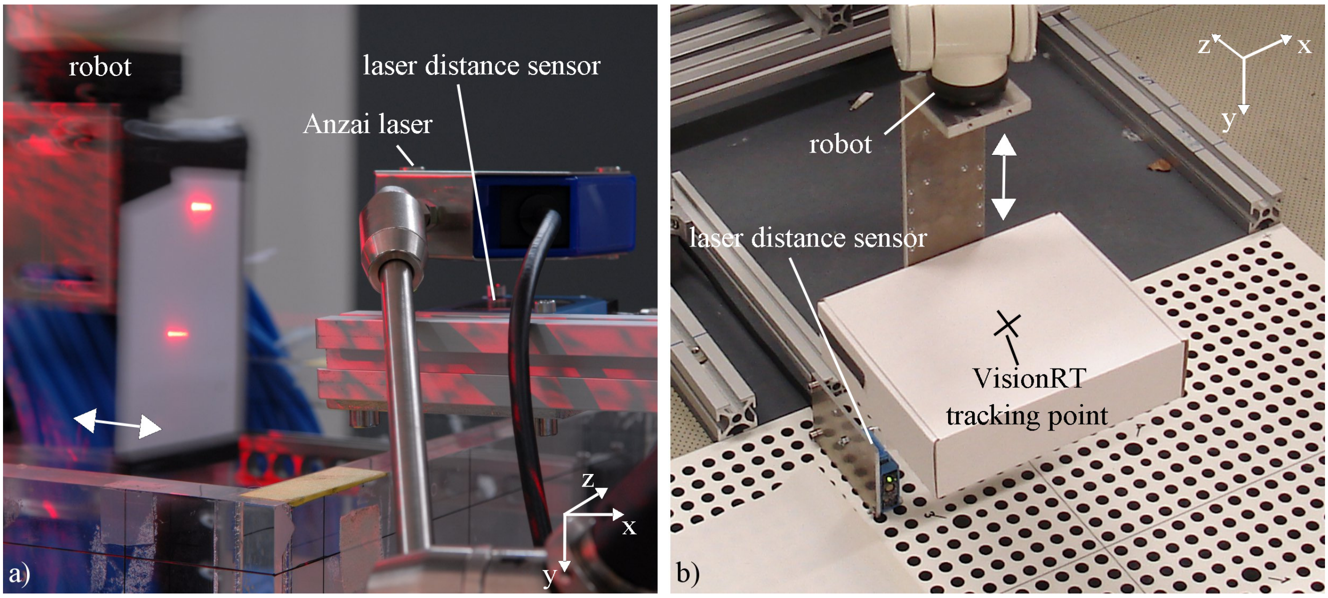

Figure 5.1.: **(a)** Setup for delay measurements of the Anzai system. One can see the Anzai laser and an additional LDS measuring the distance to a reflective plate which was moved in left-right (x) direction using the robot. **(b)** Setup for the measurements using the VisionRT system. In this case a horizontal reflective plane (white box) was moved in up-down direction. The top surface of the box was tracked using the VisionRT system. In addition a LDS measured its motion from the bottom.

In case of the VisionRT system robot motion was different since the motion signal generated by that system is based on the anterior-posterior (AP)-motion of the tracking point corresponding to the y-direction. Thus, a 1D sinusoidal motion was used

$$y(t) = \frac{1}{2} \cdot A \cdot \sin\left(\frac{2\pi}{T_t} t\right) \tag{5.2}$$

also with $A = 20\,\mathrm{mm}$ and $T_t = 3\,\mathrm{s}$. Motion of a horizontal surface mounted at the robotic arm was tracked by the VisionRT system. The same motion was, in addition, measured using a LDS. 49 measurements distributed over 5 days have been performed (4 min to 6 min – 81 to 120 gates). Each day prior to the first measurement the camera system was calibrated, the tracking point was set and in a pre-run the GW was defined according to the minimum and maximum amplitude to achieve also a gate between 50 % exhale and 50 % inhale.

The resulting gate signal as well as the signal of the additional LDS were recorded by a Beckhoff EtherCAT-system (see also figure 4.10) with a temporal resolution of 1 ms.

Based on the measured motion signals and the set gating levels the planned gates were calculated and compared with the measured ones. For each gate a start and a stop delay was evaluated which were defined as follows:

$$\begin{aligned}\Delta t_{\mathrm{Start}} &= t_{\mathrm{M}}^{\mathrm{ON}} - t_{\mathrm{P}}^{\mathrm{ON}} \\ \Delta t_{\mathrm{Stop}} &= t_{\mathrm{M}}^{\mathrm{OFF}} - t_{\mathrm{P}}^{\mathrm{OFF}}\end{aligned} \tag{5.3}$$

where t_{M} is the measured and t_{P} the planned time of each gate signal's rising edge (ON) and falling edge (OFF), respectively.

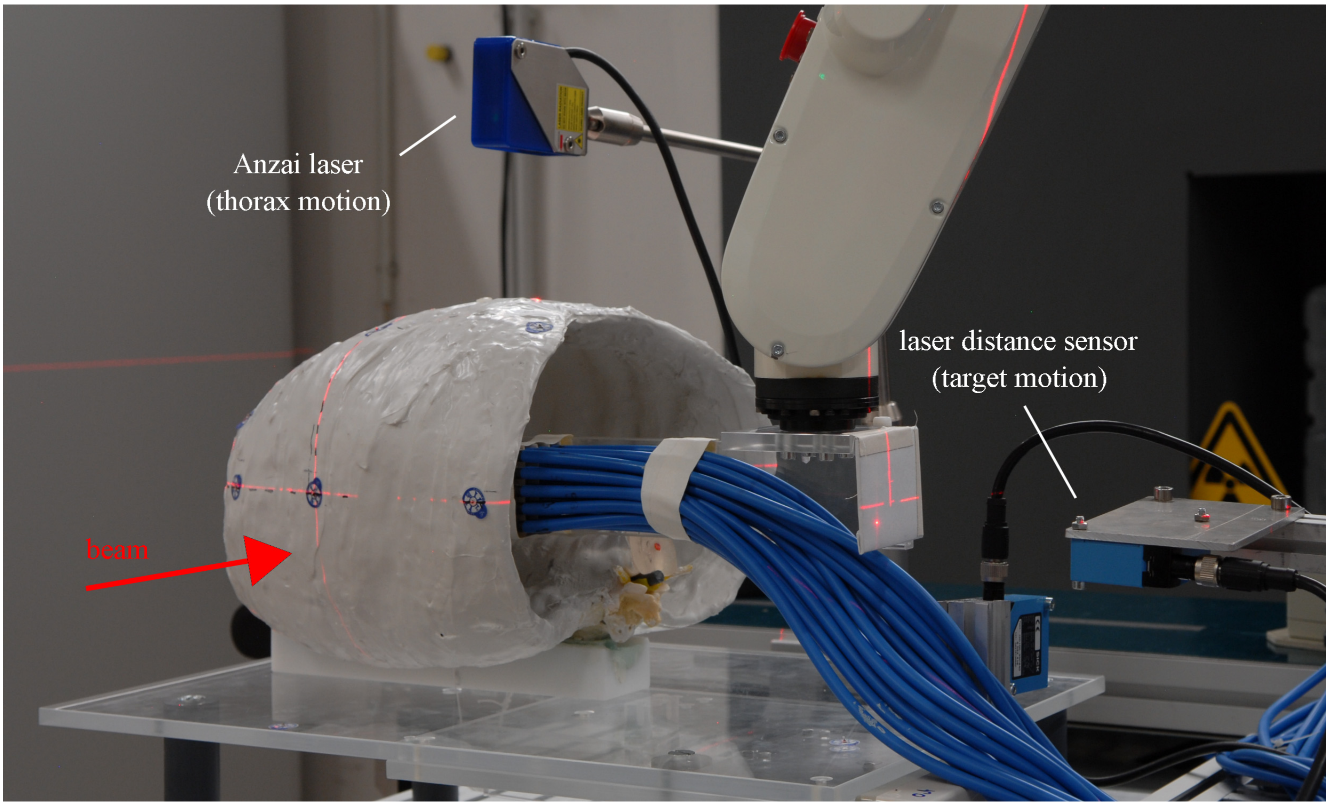

Figure 5.2.: Setup for the dosimetric phase shift analysis. More details on the used phantom can be found in chapter 4.

To investigate dosimetric effects of gating delays using the phantom presented in chapter 4 gating experiments were performed at HIT. The setup is shown in figure 5.2. The target comprising 20 pinpoint ionization chambers was moved as described in equation 5.1 with $A = 20\,\mathrm{mm}$ and $T_t = 3\,\mathrm{s}$. A PTV of the size of the detector head was irradiated with a homogeneous dose of 1 Gy using a scanned carbon beam. Gating was based on the laser of the Anzai system measuring the thorax motion. Besides a stationary measurement 11 gated irradiations (GW= 25 % amplitude based) were performed, each with a different phase shift between target and thorax motion. Phase shifts within an interval of $-30°$ to $10°$ with an increment of $5°$ and, in addition, shifts of 90° and 180° were measured.

To support the results, simulations were performed with the aid of 4DTRiP [Bert and Rietzel, 2007; Richter et al., 2010c, 2011]. Based on the data used for treatment delivery dose distributions were calculated with phase shifts of 0° to 360°. Within the intervals of $-50°$ to 10°, 70° to 90°, and 160° to 180° shifts were varied using a step size of 1°. In all other intervals a 5° increment was used. Simulations were done without accounting for a potential motion monitor delay.

To be able to compare simulations to measurements it has to be taken into account that measurements were biased by an Anzai gating delay. Therefore, the RMS of the deviations of all measured phase shifts from the corresponding calculated ones for delays $\Delta\phi_l$ of 0° to 20° (0 ms to 167 ms) was calculated as follows:

$$\mathrm{RMS}_{\Delta\phi_l} = \sqrt{\frac{1}{N}\sum_{k=1}^{N}\left(SD^{\mathrm{M}}_{\phi_k} - SD^{\mathrm{C}}_{\phi_k-\Delta\phi_l}\right)^2} \tag{5.4}$$

where $N = 11$ is the number of measured phase shifts, $SD^{\mathrm{M}}_{\phi_k}$ is the standard deviation of the mean measured doses of the 20 pinpoint ionization chambers and $SD^{\mathrm{C}}_{\phi_k-\Delta\phi_l}$ is the standard deviation of the mean calculated doses of 20 extraction positions corresponding to the pinpoint measurement positions within the dose distribution. The delay $\Delta\phi_l$ for which the RMS was smallest was assumed to be the occurred gating delay.

5.2.2 Correlation

Preparation experiments

The second part of the sensor comparison was based on a correlation study. MV-fluoroscopy was used to gather motion trajectories from tumours temporally synchronized to the motion traces acquired with the Anzai system and the VisionRT system. At UCHD in one treatment room a Anzai system and a VisionRT system are available. In addition, the linear accelerator (LINAC) (Artiste® (Siemens AG, Erlangen, Germany)) which is installed in that room provides functionality to record MV-fluoroscopy based on the treatment beam.

Prior to patient measurements temporal correlation and fluoroscopy frame rate was investigated using a sliding table comprising radiopaque markers (screws), a moving reflective surface for the VisionRT system and a spring generating a pressure signal on the load cell of the Anzai system during phantom motion. The phantom is shown in figure 5.3. Motion was tracked with the VisionRT system, the Anzai system, fluoroscopy, and an additional LDS. Temporal synchronization was done using the beam status output of the LINAC which was fed into the VisionRT system and Anzai system. The LDS measurement was temporally synchronized by means of a Geiger counter.

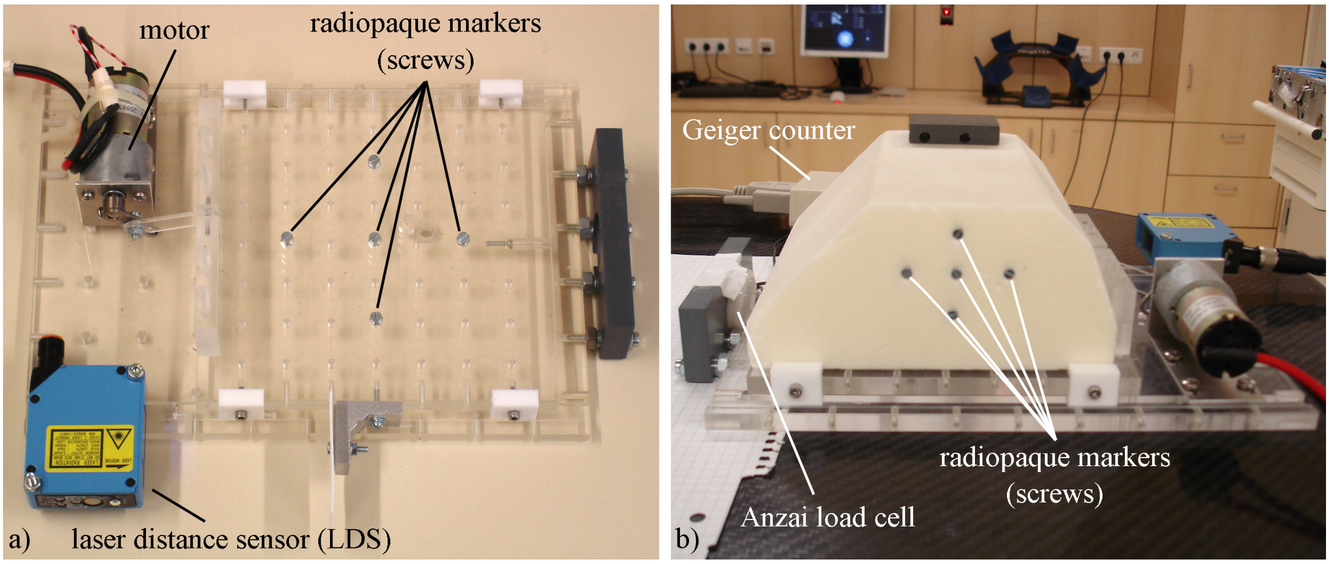

Figure 5.3.: Sliding table phantom. **(a)** On a base plate a movable plate is mounted (both made of PMMA) which can perform sinusoidal motion driven by an electric motor. Five screws are positioned in the middle of the moving plate representing radiopaque markers. On the right hand side a holder for the Anzai load cell is mounted. During motion a spring applies pressure on the load cell. Motion is measured using the LDS. **(b)** Sliding table in setup position with mounted reflective surface which is tracked by the VisionRT system. In the background the Geiger-counter is visible. At the left side the mounted Anzai load cell can be seen.

Four different voltages were applied to the driving motor resulting in four periods. In addition, two amplitudes ((26.0, and 17.8) mm) were chosen. In all cases the irradiation time was identical (150 MU using a dose rate of 300 MU/min).

An analysis software was implemented which extracted the marker motion from the fluoroscopy sequences and compared the resulting trajectory to the three sensor signals [Steidl et al., 2010]. Frame rates were calculated based on extracted periods and general data acquisition (DAQ)-functionality was tested.

Patient study

After this DAQ-test patient measurements could be started. Criteria for including patients into the study were defined as follows:

i) isolated tumour in the lung

ii) sufficient tumour motion judged by the physician

iii) treatment at the Artiste® in 1 to 5 fractions

Criterion (i) was necessary to increase the chance of tracking the tumour in the MV-fluoroscopy sequences. It was expected that an isolated tumour surrounded by low-density lung tissue might be clearer visible in MV-images compared to a tumour surrounded by high-density tissue (e. g. liver tumours). Criterion (ii) originates from the opinion that correlation analysis does only make sense if sufficient motion is present. With criterion (iii) normal fractionation and IMRT was explicitly excluded to get fluoroscopy sequences of a reasonable duration (several breathing cycles). Within the last two years of the here presented work five patients could be included into the correlation study. Additionally to the normal treatment the Anzai-belt was used following the standard protocol: the belt was put around the abdomen except for patient three (see also table 5.1) where due to an applied abdominal compression the belt was adopted around the breast. Furthermore, the VisionRT system tracked the motion of the sternum and the EPID recorded MV-fluoroscopic sequences. The number of fractions and fields as well as the number of acquired data sets are listed in table 5.1.

The number of data sets differs significantly from the theoretical number which would be the fraction number multiplied by the field number. This results from problems which occurred during data acquisition: In some cases the EPID could not be used due to safety issues which reduces the number of fluoroscopic sequences. For some fields the VisionRT system's field of view was covered by the gantry. Thus, it was not able to monitor the patient in these cases. In addition, the VisionRT system and the Anzai system in some cases due to software and hardware failures did not save the beam status signal which makes a temporal correlation impossible. The remaining number of correlated data sets is given in the last three columns of table 5.1. The

Table 5.1.: List of the acquired patient data. For each patient the number of fractions, fields per fraction, fluoroscopy sequences (F), Anzai data sets (A) and VisionRT data sets (V) are given. In addition the number of correlated sets per patient are shown in the three last columns (Fluoroscopy versus Anzai (F/A), Fluoroscopy versus VisionRT (F/V) and Anzai versus VisionRT (A/V)). The number in parentheses includes cases with no beam status signal.

ID	Fractions	Fields	Anzai (A)	Fluoro (F)	VisionRT (V)	A/V	A/F	V/F
1	3	6	15	3	15	15	3	3
2	1	7	1	1	0 (1)	0 (1)	1	0 (1)
3	5	7	29	29	0 (19)	0 (19)	29	0 (19)
4	3	7	4	2	2	2	2	0
5	3	6	3	3	0 (1)	0 (1)	3	0 (1)

numbers in parentheses include cases of the VisionRT system without beam status signal which have been analysed anyhow (see below).

Prior to analysing the correlation of the three motion signals tumour motion had to be extracted from the fluoroscopy sequences. Therefore, the software which was implemented for the phantom study presented above [Steidl et al., 2010] was extended to handle also patient data. The implementation was performed during the diploma thesis of Romain Brevet [Brevet, 2011] which was supervised in the course of the here presented work. [Brevet, 2011] also analyzed correlation scores of the VisionRT system and Anzai system with respect to the extracted tumour motion. Since this analysis showed phase shifts which were not incorporated into the analysis, phase shift investigation and correlation analysis was redone based on the previously extracted tumour motion traces. According to [Lu et al., 2006a] minima and maxima were estimated for all three types of data. Based on these extrema the phase shifts ϕ_{MM} where calculated. For the pure signals which were only matched by the beam status signal and for the signals which were additionally corrected for the phase shifts ϕ_{MM} the correlation coefficient

$$\mathrm{CC}\left(f(t),g(t)\right)=\frac{\sum_{k=1}^{N}\left[\left(f(t_k)-\frac{1}{N}\sum_{l=1}^{N}f(t_l)\right)\left(g(t_k)-\frac{1}{N}\sum_{l=1}^{N}g(t_l)\right)\right]}{\sqrt{\sum_{k=1}^{N}\left(f(t_k)-\frac{1}{N}\sum_{l=1}^{N}f(t_l)\right)^2\cdot\sum_{k=1}^{N}\left(g(t_k)-\frac{1}{N}\sum_{l=1}^{N}g(t_l)\right)^2}} \tag{5.5}$$

was calculated where $f(t)$ and $g(t)$ are two signals to compare.

Since in one case the correlation coefficient (CC) drops significantly after applying the phase shift ϕ_{MM} phase shifts were optimized to investigate for all cases if the extrema based determination of ϕ_{MM} leaded to the right shift. To do so for phase shifts of $\pm 1/4$ of the maximum observed breathing period ($\pm 1700\,\mathrm{ms}$) around ϕ_{MM} a maximum search of CC was performed.

The resulting optimum phase shift ϕ_{CC} corresponding to the maximum CC was estimated. Besides phase shifts in some signals base line drifts and jumps were observed. To estimate their implication on the resulting CC the signals were normalized period by period to the local amplitude range as defined by [Lu et al., 2006a] and the CC for these normalized signals was calculated, too.

To increase the number of comparable cases also the VisionRT data without beam status signal was analysed. For cases where Anzai with beam status and fluoroscopy were available the VisionRT signal was shifted against the two other signals with a resolution of 1 ms and the CC of VisionRT versus Anzai and VisionRT versus fluoroscopy, respectively, were calculated. The phase shift between Anzai and fluoroscopy was set to ϕ_{MM}. Three global shifts $\phi_{\mathrm{CC}}^{\mathrm{NB}}$ where estimated: One for a maximum $\mathrm{CC}_{\mathrm{V\ vs.\ A}}$, one for a minimum $\mathrm{CC}_{\mathrm{V\ vs.\ F}}$ (minimum because it is anti-correlated), and one for the maximum of $\mathrm{CC}_{\mathrm{V\ vs.\ A}} + |\mathrm{CC}_{\mathrm{V\ vs.\ F}}|$.

5.3 Results

5.3.1 Gating delays

As a summary the mean and the SD of the 13 measured cases as well as the total minimum and maximum delay of all investigated GW is given in table 5.2 for $\Delta t_{\mathrm{Start}}$ and Δt_{Stop}, respectively.

Table 5.2.: Measured gating delays of the Anzai system. Besides the total number of measured cases N_{M} the number of gating windows N_{GW}, the sampling interval (SaI) and for start and stop delay ($\Delta t_{\mathrm{Start}}$ and Δt_{Stop}, respectively) the minimum, maximum and mean of the delay is given.

N_{M}	N_{GW}	SaI	$\Delta t_{\mathrm{Start}}$				Δt_{Stop}			
			Mean	SD	Min	Max	Mean	SD	Min	Max
		[ms]	[ms]	[ms]	[ms]	[ms]	[ms]	[ms]	[ms]	[ms]
13	59–105	25	100	24	44	165	103	23	42	152

Since in case of VisionRT results turned out to be day specific for each day they are summarized in table 5.3. The total maximum delay of all analyzed GW was 265 ms ($\Delta t_{\mathrm{Start}}$) and 260 ($\Delta t_{\mathrm{Stop}}$), respectively.

Detailed results of gating delays for Anzai and VisionRT can be found in the appendix (section A.1 and section A.2).

Figure 5.4 shows the results for the phase shift measurements and simulations. In figure 5.4(a) the measured doses of the 20 pinpoint ionization chambers relative to the stationary measurement are plotted over the applied phase shifts. The measured phase shift of 90° turned out to be the worst case while the result of a phase shift of 180° is comparable to the results for

Table 5.3.: Measured gating delays of the VisionRT system. For each day the number of measurements N_{M}, the number of gating windows N_{GW}, the sampling interval (SaI) and the mean, minimum and maximum start ($\Delta t_{\mathrm{Start}}$) and stop ($\Delta t_{\mathrm{Stop}}$) delay, respectively, is listed.

Day	N_{M}	N_{GW}	SaI		$\Delta t_{\mathrm{Start}}$				Δt_{Stop}			
			Mean [ms]	SD [ms]	Mean [ms]	SD [ms]	Min [ms]	Max [ms]	Mean [ms]	SD [ms]	Min [ms]	Max [ms]
1	10	90–120	80	1	162	6	93	265	144	14	75	260
2	9	90–117	74	1	119	12	54	188	124	16	63	201
3	8	81–112	74	0	118	10	59	170	105	9	45	155
4	11	93–119	74	0	133	7	77	195	126	6	72	196
5	11	87–112	79	1	129	7	66	230	149	8	81	256

phase shifts around 0°. In figure 5.4(b) the SD of the measured doses are plotted together with the results from the phase shift simulations. Simulation results are additionally shifted by $-11°$ since for a gating delay of $\Delta\phi_l = 11°$ the resulting RMS was smallest.

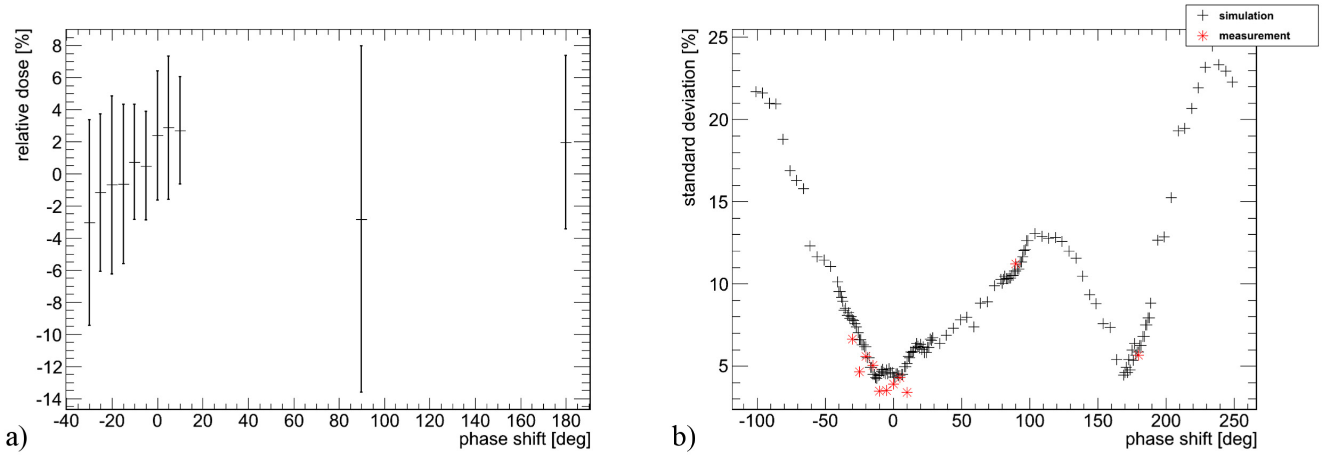

Figure 5.4.: Results of the measured and simulated phase shifts. **(a)** Measured doses of the 20 pinpoint ionization chambers relative to the stationary case. **(b)** Measured and simulated standard deviations of the 20 pinpoint ionization chambers. Simulations are additionally shifted by $-11°$.

5.3.2 Correlation

Preparation experiments

Tracking of the radiopaque marker and, thus, phantom motion extraction from the MV-fluoroscopy sequences worked very well. The resulting periods of Anzai system, VisionRT system, LDS, and fluoroscopy are given in table 5.4.

Table 5.4.: Results of preparation measurements of the correlation study. Shown are the mean and standard deviation (SD) of the resulting periods in seconds and in case of fluoroscopy in frames (f).

#	Motor voltage	Amplitude	Anzai		VisionRT		LDS		Fluoroscopy	
			Mean	SD	Mean	SD	Mean	SD	Mean	SD
	[V]	[mm]	[s]	[s]	[s]	[s]	[s]	[s]	[f]	[f]
1	5	26.0	5.37	0.01	5.37	0.01	5.37	0.01	67.1	0.2
2	5	17.8	5.41	0.01	5.40	0.01	5.41	0.02	67.5	0.7
3	5	17.8	5.40	0.01	5.41	0.02	5.40	0.04	67.6	0.1
4	7	26.0	3.75	0.01	3.76	0.01	3.74	0.05	46.9	0.3
5	7	17.8	3.67	0.04	3.67	0.01	3.66	0.02	45.8	0.2
6	9	26.0	2.75	0.01	2.75	0.02	2.75	0.01	34.4	0.1
7	9	17.8	2.76	0.06	2.76	0.01	2.76	0.05	34.5	0.1
8	12	26.0	2.02	0.04	2.02	0.04	2.02	0.02	25.1	0.0
9	12	17.8	2.01	0.01	2.02	0.01	2.01	0.01	25.2	0.1

Based on these periods frame rates of the fluoroscopy sequences were found to be $(12.5 \pm 0.2)\,\mathrm{fps}$. The motion amplitude extracted from the fluoroscopy sequences was plotted together with the other three signals for visually inspection. As an example figure 5.5 shows the plot of measurement #7 which is representative for all cases.

Patient study

Figure 5.6 shows as an example results for the extrema detection within the patient breathing motion traces. Positions of minima and maxima and the mean local amplitude are plotted (red line). Extrema were nicely detected by the algorithm reported by [Lu et al., 2006a] in all cases. The resulting phase shifts ϕ_{MM} are given in table 5.5 for each patient separately since phase shifts turned out to differ from patient to patient.

Table 5.5.: Phase shifts ϕ_{MM} estimated according to [Lu et al., 2006a] for Anzai versus VisionRT ($\phi_{\mathrm{MM}}^{\mathrm{AV}}$), Anzai versus fluoroscopy ($\phi_{\mathrm{MM}}^{\mathrm{AF}}$), and VisionRT versus fluoroscopy ($\phi_{\mathrm{MM}}^{\mathrm{VF}}$).

ID	Cases	$\phi_{\mathrm{MM}}^{\mathrm{AV}}$ [ms]			$\phi_{\mathrm{MM}}^{\mathrm{AF}}$ [ms]			$\phi_{\mathrm{MM}}^{\mathrm{VF}}$ [ms]		
		Min	Max	Mean	Min	Max	Mean	Min	Max	Mean
1	15	−865	−99	−500	29	137	77	503	984	691
2	1				−49	−49	−49			
3	29				−321	383	−22			
4	4	64	85	75	4	12	8			
5	3				53	119	77			

In several motion trajectories base-line drifts were observed which incidence was also patient specific. While Anzai showed in most cases constant signals and, except for one case, only drifts

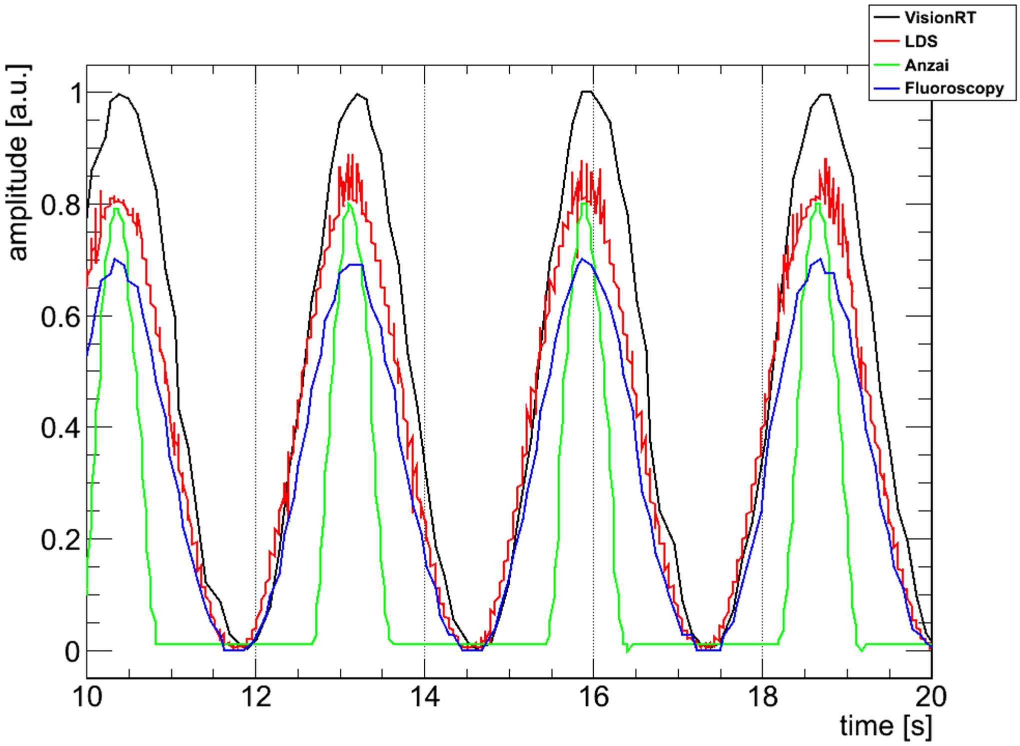

Figure 5.5.: Representative plot of measured and extracted motion traces. Time scale of fluoroscopy data is scaled based on a frame rate of 12.5 fps. Amplitudes are scaled differently to be able to distinguish between the four graphs.

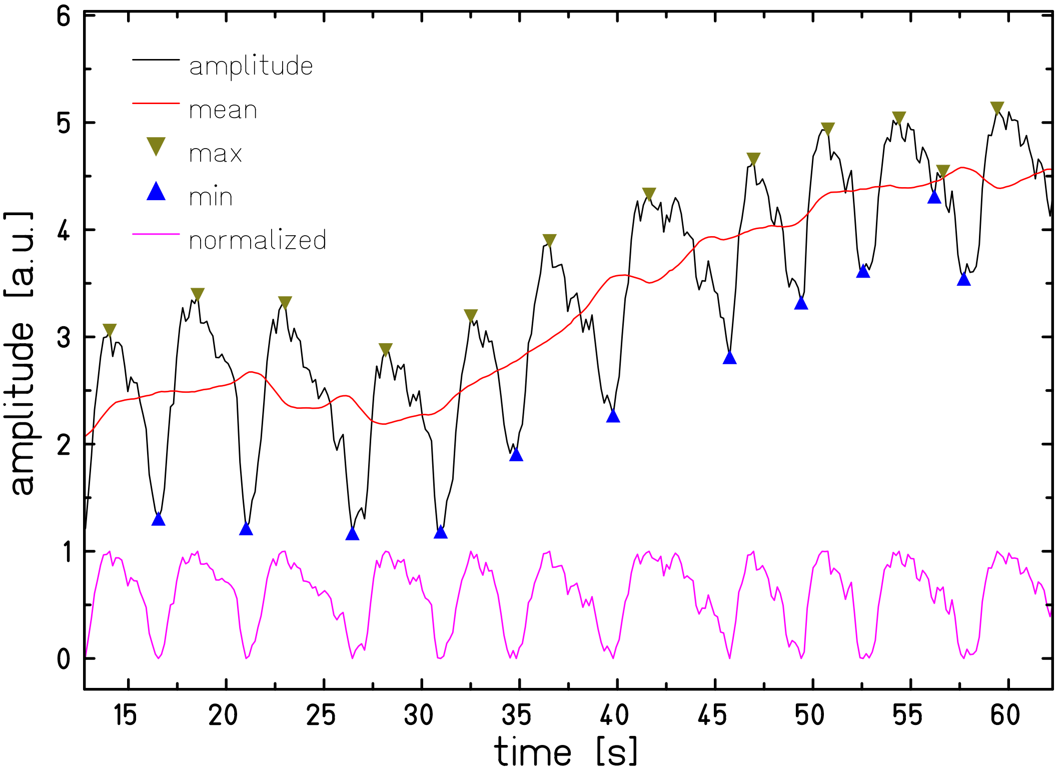

Figure 5.6.: Exemplary results for the extrema evaluation. The plot shows one VisionRT trajectory overlaid with markers at the detected minima and maxima positions. The red line represents the mean local amplitude and the purple line the resulting base-line drift corrected (normalized) trajectory.

and jumps when other signals also drifted or jumped, for VisionRT and fluoroscopy base line drifts or jumps could be observed while corresponding signals stayed constant. As an example in figure 5.7 jumps are shown for Anzai, VisionRT and fluoroscopy.

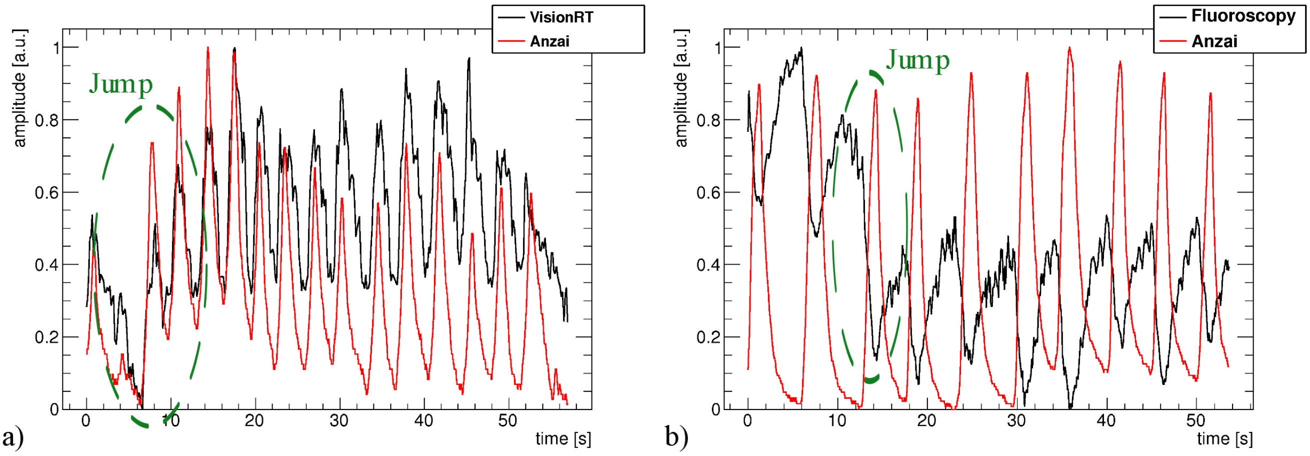

Figure 5.7.: Examples for cases with sudden jumps. **(a)** Jump in VisionRT and Anzai signal. **(b)** Jump only in fluoroscopy signal while Anzai signal stays constant.

Base-line drifts or jumps could be successfully removed by normalizing trajectories with respect to local amplitude. In figure 5.6 besides the already mentioned indicators for minima, maxima and mean amplitude the normalized trajectory is plotted.

For the same case in figure 5.8 normalized and original trajectories are shown uncorrected, corrected by the phase shifts determined based on minima and maxima ϕ_{MM} and corrected by the phase shift resulting for a maximum CC between the two signals ϕ_{CC}. As in figure 5.8, in all cases correction by ϕ_{MM} leads to a good matching of the extrema of the different trajectories. In almost all cases ϕ_{CC} differs from ϕ_{MM} by less than 250 ms which indicates that the phase shift estimation based on the minima and maxima worked very well.

For the analysis of VisionRT signals without beam status information in all cases the correlation coefficient of VisionRT versus Anzai $\mathrm{CC}^{\text{NB-A}}$ showed a global maximum while for the CC of VisionRT versus fluoroscopy $\mathrm{CC}^{\text{NB-F}}$ a global minimum could be found. In most cases the corresponding shifts between VisionRT and the two other signals, $\phi_{\mathrm{CC}}^{\text{NB-A}}$ and $\phi_{\mathrm{CC}}^{\text{NB-F}}$, differed by less than 410 ms. This indicates that the found shift $\phi_{\mathrm{CC}}^{\text{NB-AF}}$ based on the best correlation in respect of both signals (maximum of $\mathrm{CC}^{\text{NB-A}} + |\mathrm{CC}^{\text{NB-F}}|$) represents a clear matching position. Such a distinct case is exemplarily shown in figure 5.9 in the upper row: in (a) the two correlation coefficients $\mathrm{CC}^{\text{NB-A}}$ and $\mathrm{CC}^{\text{NB-F}}$ are plotted showing a global maximum in the former case and a global minimum in the latter case which are located at the same position. (b) shows the correspondingly shifted trajectories which lie upon each other due to the little differing shifts $\phi_{\mathrm{CC}}^{\text{NB-A}}$, $\phi_{\mathrm{CC}}^{\text{NB-F}}$, and $\phi_{\mathrm{CC}}^{\text{NB-AF}}$.

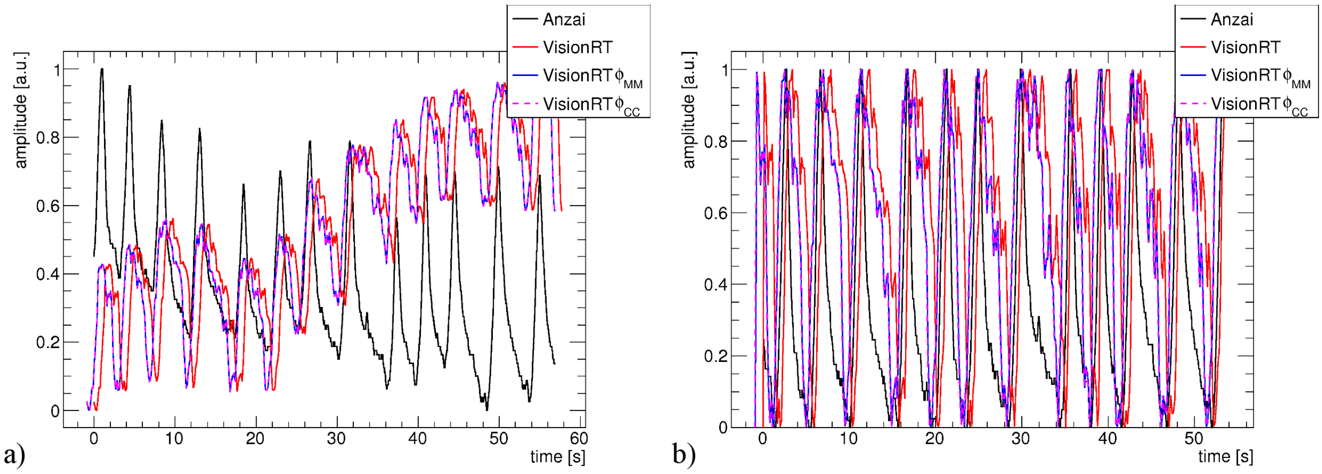

Figure 5.8.: Phase shift corrected breathing signals. The VisionRT signal is plotted at original position as well as shifted by ϕ_{MM} and ϕ_{CC}. Since the difference between the two shifts is very low (-9 ms in **(a)** and 46 ms in **(b)**) the two latter plots (blue and purple graphs) are lying upon each other. **(a)** Original motion traces. **(b)** Normalized signals.

In three cases $\phi_{\text{CC}}^{\text{NB-A}}$ and $\phi_{\text{CC}}^{\text{NB-F}}$ differ more than 2 s. The worst case in this context is shown in figure 5.9 in the lower row: In (c) again the two correlation coefficients are plotted showing a difference of 28.8 s between $\phi_{\text{CC}}^{\text{NB-A}}$ and $\phi_{\text{CC}}^{\text{NB-F}}$. Since at the position of $\phi_{\text{CC}}^{\text{NB-A}}$ the second largest minimum of $\text{CC}^{\text{NB-F}}$ is located and the maximum of $\text{CC}^{\text{NB-A}}$ at $\phi_{\text{CC}}^{\text{NB-A}}$ is much larger than the maximum of the same CC at $\text{CC}^{\text{NB-F}}$ also $\phi_{\text{CC}}^{\text{NB-AF}}$ results at the same position as $\phi_{\text{CC}}^{\text{NB-A}}$. The plot of the motion traces shifted by $\phi_{\text{CC}}^{\text{NB-A}}$, $\phi_{\text{CC}}^{\text{NB-F}}$, and $\phi_{\text{CC}}^{\text{NB-AF}}$ in figure 5.9(d) shows that a shift of $\phi_{\text{CC}}^{\text{NB-AF}}$ results in a well matching trajectory.

The resulting correlation coefficients for uncorrected, phase shift corrected, and base line corrected trajectories are summarized in table 5.6. Detailed results for each patient can be found in the appendix (section A.3).

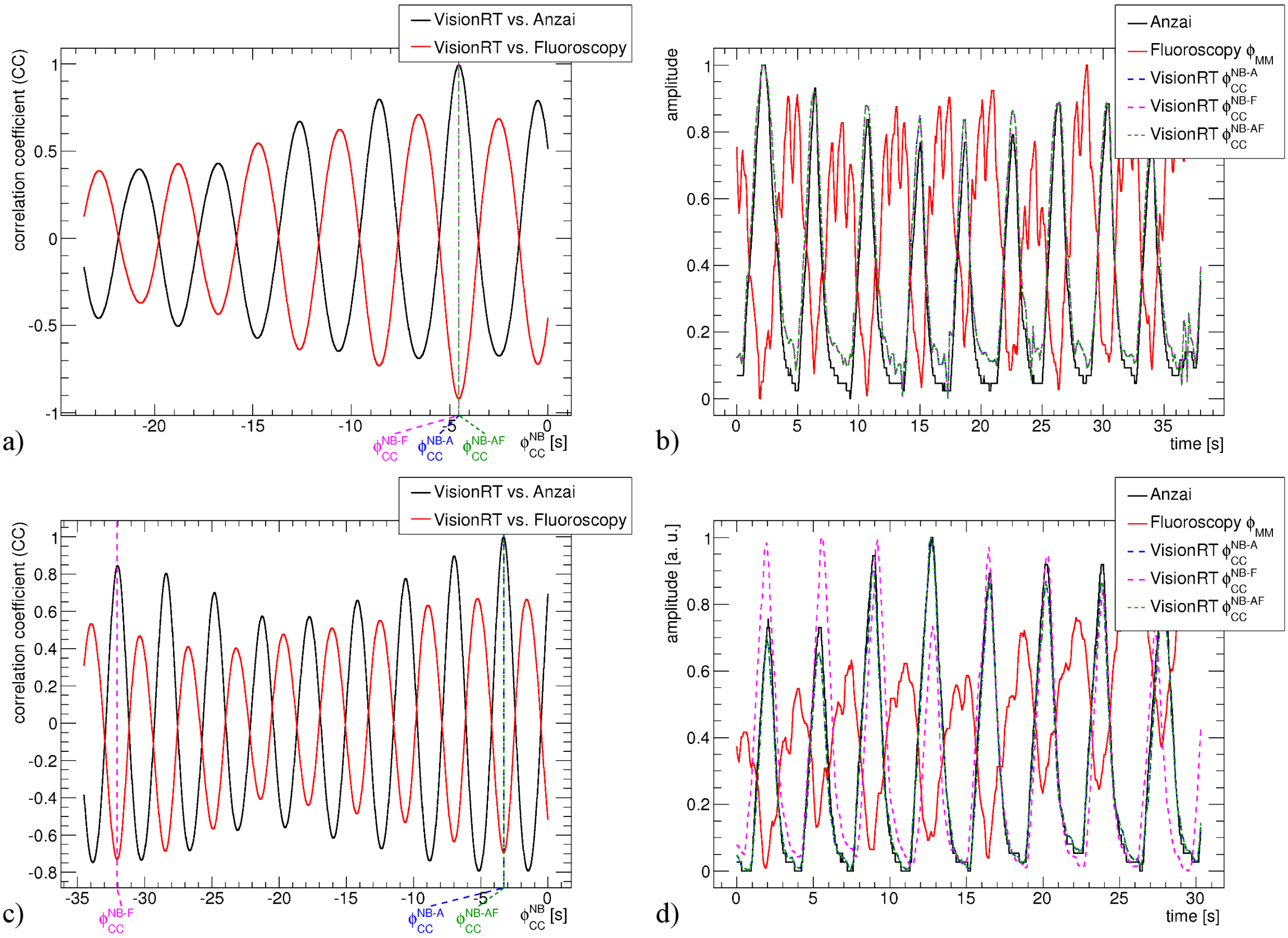

Figure 5.9.: Matching result for VisionRT cases without beam status for a clearly matching case (upper row) and the case with largest difference between $\phi_{CC}^{NB\text{-}A}$ and $\phi_{CC}^{NB\text{-}F}$ (upper row). **(a)** Correlation coefficients of VisionRT versus Anzai and VisionRT versus fluoroscopy. $\phi_{CC}^{NB\text{-}A}$,$\phi_{CC}^{NB\text{-}F}$ and $\phi_{CC}^{NB\text{-}AF}$ are almost equal (differences below $50\,\mathrm{ms}$). **(b)** Motion traces shifted by the corresponding values shown in (a). The three motion traces of VisionRT are lying upon each other. **(c)** Correlation coefficients for the worst matching case: $\phi_{CC}^{NB\text{-}A}$ and $\phi_{CC}^{NB\text{-}F}$ differ by $28.8\,\mathrm{s}$. **(d)** Shifted motion signals for the worst matching case. The purple trajectory differs from the blue and green curves resulting from the large differences between the corresponding shifts.

Table 5.6.: Summary of the correlation results. For each type of correlation the number of available cases is given. The numbers in parentheses include also cases where no beam status was available in the VisionRT system, but matching based on the CC worked. For normalized and non-normalized motion traces the CC as well as the phase shift corrected CCs based on ϕ_{MM} and ϕ_{CC} are given. $|CC|_{CC}^{NB}$ represents the correlation results for VisionRT cases without beam status.

Type	Cases		$\|CC\|$	$\|CC\|_{MM}$	$\|CC\|_{CC}$	$\|CC\|_{CC}^{NB}$	$\|CC\|_{MM}^{Norm}$	$\|CC\|_{CC}^{Norm}$
A vs. V	17 (38)	Min	0.01	0.01	0.04	0.58	0.64	0.67
		Max	0.97	0.98	0.98	1.00	0.96	0.99
		Mean	0.43	0.64	0.65	0.96	0.81	0.83
A vs. F	38	Min	0.36	0.37	0.48		0.48	0.75
		Max	0.95	0.95	0.95		0.97	0.98
		Mean	0.73	0.73	0.78		0.89	0.92
V vs. F	3 (24)	Min	0.19	0.35	0.49	0.29	0.73	0.76
		Max	0.47	0.80	0.82	0.92	0.81	0.84
		Mean	0.29	0.57	0.57	0.71	0.78	0.81

5.4 Discussion

5.4.1 Gating delays

In two experiments gating delays of the VisionRT system and the Anzai system were performed showing clear differences in the results. Measured gating delays of the VisionRT system turned out to be higher than for the Anzai system (45 ms to 265 ms for VisionRT compared to 42 ms to 165 ms for Anzai – compare table 5.3 and table 5.2). This behaviour was expected since the sampling intervals of the two systems differ (74 ms to 80 ms for VisionRT compared to 25 ms for Anzai). But the difference between the mean delays is lower than the difference between the sampling intervals. This may be due to a faster processing of the acquired data by the VisionRT system. Behaviour of the VisionRT system, in addition, turned out to be calibration dependent. A change of the sampling intervals was observed after redoing calibration and tracking point definition. Thus, calibration has to be done carefully. The maximum measured gating delay of the VisionRT system is 100 ms larger than the maximum delay measured using the Anzai system. However, even a mean delay of about 100 ms (corresponding to 12° for a period of 3 s) resulting for the Anzai system can change the dosimetric outcome as the dosimetric phase shift measurements show.

These results seem to differ from expectations. In case of gating the beam is switched on when the target is within the target volume. For a phase shift of 180° between motion signal and actual motion, the beam is switched on when the target centre is maximum distant from the target volume centre. If the target volume is small compared to the motion, this would result in a worst dose distribution for a phase shift of 180°. In our case the target motion of 20 mm peak-to-peak was small compared to the target volume size of $(50 \times 50 \times 50)\,\mathrm{mm}^3$. In addition, the sensitive volumes of the pinpoints were distributed in the left 2/3 of the target. Therefore, also for a phase shift of 180° all 20 pinpoints stay within the target volume during motion. Thus, dosimetric results vary based on the interplay effect caused by the effective residual motion. The gating window size in terms of motion phases was equal for all phase shift measurements. Since depending on the applied phase shift, the velocity within the gating window changes, the resulting residual motion amplitude changes, too. Therefore, the largest effective residual motion is reached for a phase shift of 90° (and, of course, 270°). This is why the dose results show the worst interplay pattern for a phase shift of 90° and the result for 180° is comparable to the ones around 0°.

Gating delay estimation based on the measured phase shifts by comparison to simulations resulted in a delay of 11° corresponding to 92 ms which is reasonable compared to the mean Anzai delays of about 100 ms. Taking this shift into account measurements and calculations match very well.

For patient irradiations a correction for gating delays can be done based on the mean breathing period. Since breathing behaviour of a patient can easily change during a treatment session an online adaptation of the GW to correct for gating delays may be a better solution which is, however, not possible with both systems.

5.4.2 Correlation

Preparation experiments for the correlation study showed that temporal correlation of the signals is doable and the frame rate could successfully be analyzed since motion extraction worked for the phantom.

Correlation analysis of patient data showed very heterogeneous results. Correlation coefficients differ depending on patient, fraction and field number which was also found by other groups [Hoisak et al., 2004; Ionascu et al., 2007]. Two reasons for that could be identified by the analysis shown above:

Since extrema determination worked very well phase shifts could be successfully estimated. These phase shifts turned out to be very patient specific. Especially for patient 1 large shifts up to 1 s occurred between VisionRT and the Anzai system while for patient 4 this shift was significantly lower. Also the phase shift between the Anzai system and fluoroscopy varied depending on the patient. Observed phase shifts match to values for comparison of other motion sensors found in the literature [Ionascu et al., 2007; Otani et al., 2010; Tsunashima et al., 2004]. A reason for these shifts may be the position of data acquisition. In this study the area around the sternum was the basis for motion tracking using the VisionRT system while the Anzai belt for patient 1,2,4, and 5 was measuring at the abdominal region. In case of patient 3 due to the used abdominal compression the Anzai belt also measured breast motion. It is reasonable that during breathing a phase shift between breast breathing and abdominal respiration can occur and that internal motion may higher correlate to the abdominal motion since the diaphragm is mainly causing the lung motion. For the five patients phase shifts of the Anzai system were small in case of measuring abdominal motion and large in case of measuring breast motion. For the VisionRT system phase shifts were large for one patient and low for the second one (patient 4) where beam status information was available. This difference can also be seen for the Anzai belt where phase shifts were smallest for patient 4.

Base line drifts were found in all types of observed signals. The Anzai system showed the smallest drifts even when internal motion showed large ones. Base line drifts may be caused by muscle relaxation which e. g. was reported by [von M. Siebenthal et al., 2007b].

Correction of the signals with respect to base line drifts worked also very well and the resulting increased correlation coefficients show that a base line drift also influences the correlation.

Correlation coefficients of Anzai versus VisionRT ranged from 0.01 to 0.97 (table 5.6; $|CC|$) in the uncorrected calculation which strongly depends on patient, but also phase shift and base-line drift. If signals are corrected for both influences ($|CC|_{MM}^{Norm}$) the correlation coefficient rises significantly in most cases. Also the comparison of the Anzai signals with the VisionRT signals without beam status showed that there seem to be a high correlation in almost all cases ($|CC|_{CC}^{NB}$). This data can not be compared directly to reported data from the literature. But there are two publications comparing the Anzai system and the VisionRT system, respectively, to the RPM system. [Otani et al., 2010] found CCs ranging from 0.94 to 0.99 for Anzai versus RPM and [Hughes et al., 2009] reported a CC of 0.62 to 0.96 for VisionRT versus RPM.

For VisionRT versus fluoroscopy only three cases were measured with beam status signal and a low CC was found (0.19 to 0.47). Also here a strong dependency on phase shift and base-line drift can be seen which indicates also a dependency on the tracking point position as mentioned above. Since the VisionRT system so far was not investigated with respect to correlation to internal motion, results may be compared to correlation coefficients published by [Koch et al., 2004] who studied correlation of surface motion to internal motion based on MRI. They found a CC ranging from 0.58 to 0.9 with strong dependence on the chosen surface marker which corresponds to the tracking point position on the thorax surface.

The Anzai system correlates a little better with the internal motion than the VisionRT system. CCs ranging from 0.36 to 0.95 were found (table 5.6) which are comparable to the results of [Ionascu et al., 2007] who computed the correlation of the Anzai system to kV-fluoroscopy and reported a CC of 0.77 to 0.88. However, they used the Anzai laser while we used the pressure belt which may have implications on the result. If signals are corrected for phase shifts and base-line drifts only slightly higher CCs remain for the Anzai versus fluoroscopy compared to VisionRT versus fluoroscopy. This also indicates that the correlation may have something to do with differences in breast breathing and abdominal respiration which may cause these shifts and drifts and may have more effect on the VisionRT system if the tracking point is set to the sternum region.

In summary, the Anzai system showed lower gating delays than the VisionRT system which is reasonable due to the lower sampling interval. But according to that interval even smaller delays would have been expected for the Anzai system. All found delays are too little to affect geometrical mismatch of the tumour but it was shown that the dose interplay pattern may change due to a change residual motion. If a maximum short gating delay has highest priority the Anzai system would be the preferred system.

With respect to correlation coefficients no clear judgement can be made. It was shown that differences between the correlation of Anzai versus fluoroscopy and VisionRT versus fluoroscopy may mainly be caused by phase shifts and base-line drifts. Both effects seem to correlate more to the abdominal motion. The position of the skin area used for motion tracking appears to be important for both systems to gain a good internal-external correlation.

Since the VisionRT system offers more complex functionality than the Anzai system it is more sensitive to external influences. Therefore, calibration has to be done accurately and an appropriate tracking point has to be chosen which optimal position has to be investigated in the future. Both systems can show very short gating delays as well as very high correlation coefficients. Especially the correlation coefficients of Anzai versus VisionRT were high in most (at least phase shift corrected) cases. Therefore, differences between the two systems can be small if they are used appropriate.

6 Comprehensive discussion and future prospects

Gating will most likely be the first technique used for the treatment of liver patients at Heidelberg Ion-Beam Therapy Center (HIT). However, several issues have to be clarified before starting patient treatment with gated irradiation using a scanned ion-beam.

One of these aspects is the problem of residual motion. Gating implies an extension of the treatment time by up to a factor of 5 [Tsunashima et al., 2008]. Longer treatment time can result in lower treatment precision [von M. Siebenthal et al., 2007a,b] and is less comfortable for the patient. Furthermore, the total number of per day treatable patients shrinks which leads to an undesirable lower cost-efficiency. Therefore, the increase of treatment time due to gating should be as small as possible which implies a reasonably large gating window (GW). Motion within the GW is reduced, but not vanished. Since even small motion can lead to severe under and over dosage in the target volume due to the interplay effect [Bert et al., 2008; Groezinger et al., 2006; Lambert et al., 2005; Phillips et al., 1992] appropriate techniques to mitigate motion effects within the GW are needed.

According to [Bert et al., 2009] an increased overlap of the single beam spots, laterally and longitudinally, can be a solution for this problem at least for a 1D motion and with respect to film dosimetry. To bring this approach closer to clinical application more complex motion and a larger number of beam parameters which lead to the overlap of the single beam spots had to be studied. In addition, 3D absolute dosimetry had to be investigated, an instrument usually used for treatment plan verification in radiation therapy [Karger et al., 1999].

This study was performed in the course of this work (chapter 3): Lateral grid spacing, beam focus size, iso-energy slice (IES) distance, and Bragg-peak width (via different ripple filters [Weber and Kraft, 1999]) were varied and the dosimetric effects on a target moving in 3D depending on the residual motion amplitude (corresponding to a certain GW) were investigated. Since the parameter space was very large and the measurement time limited simulations were performed introducing more residual motion amplitudes and motion starting phases.

Results showed that for the lateral overlap increasing the beam focus lead to very good mitigation of residual motion consequences in terms of homogeneity while decreasing the lateral grid spacing resulted only in little effects. Thus, increasing the beam focus is more efficient than decreasing the lateral grid spacing. However, when increasing the focus size one has to be aware of the larger penumbra resulting in a higher dose to normal tissue. Reducing the IES distance also proved to be an effective possibility to gain better homogeneity while variation of the ripple filter does not show significant effect. The latter finding may be due to the little difference between the two used filters.

In parts the results were already used for patient irradiations: in the non-gated treatments of liver patients at HIT which were started this year a larger focus size was used to mitigate effects of tumours with small motion. Beyond that the results may show the possibility of reducing the treatment time: Irradiation time strongly depends on the number of IES since for each slice the particles have to be accelerated to the desired energy which at HIT takes a few seconds. In addition, irradiation time of a certain slice depends on the number of raster points. Since the beam focus size turned out to be more important than the overlap, a larger focus in combination with larger grid spacing may lead to sufficient results. Larger grid spacing results in a lower number of raster points which usually reduces the irradiation time. Thus, besides mitigating residual motion effects the results from this study may help to reduce treatment time. However, these effects should be validated in treatment plan studies based on real patient data. Furthermore, the timing implications are only true for synchrotron based treatment sites like GSI or HIT. For systems with passive energy variation irradiation time does not depend so much on the number of IES due to the much faster energy variation capability [Pedroni et al., 2004]. In addition, there is one synchrotron based scanning system at National Institute of Radiological Sciences (NIRS) which is capable of applying dose so fast [Furukawa et al., 2010b] that a reduced raster position number may not have any effect. Anyhow, for the patient treatments at HIT and similar facilities improvements can be made based on the results.

But only adapting beam parameters with the aim to mitigate residual motion effects is not sufficient to result in a satisfactory dose distribution. It has to be ensured that the target is within the target volume when the beam is switched on. Therefore, an appropriate motion monitoring system is necessary to be able to gate the beam depending on the target's position. To avoid additional dose to the patient by using direct monitoring via fluoroscopy [Shirato et al., 2004] application of surrogate signals (e. g. thorax motion) were proposed [Evans, 2008]. But if a surrogate is used it is important that the surrogate motion correlates with the actual target motion. Unfortunately, this correlation depends on the patient and can change even for one patient within one treatment session [Hoisak et al., 2004; Ionascu et al., 2007; Koch et al., 2004]. Therefore, systematic phantom studies of miscorrelations are necessary to determine dosimetric effects of base-line drifts, phase shifts and irregular motion.

In the course of this work a phantom was designed, built and validated. Initially the phantom was constructed for dosimetric correlation studies using a scanned ion beam. Therefore, amongst other parameters it should be capable to perform independent internal and external motion with fixed or variable dedicated correlation as patient realistic as possible. The built phantom consists of a breathing thorax including ribs and a target which can be moved independently in all six degrees of freedom (3 translation, 3 rotation) by a robotic arm while correlation between these two motions is adjustable. Validation experiments showed that the phantom can be used for dosimetry studies based on 20 ionization chambers distributed over the moving target volume. Furthermore, radiographic films offer the possibility to measure target dose homogeneity with a higher spatial resolution compared to the ionization chamber array. The phantom was successfully tested in several experiments and used in the third part of this work for investigating dosimetric effects of dedicated phase shifts between internal and external correlation. However, there is some room for improvement where two major aspects shall be mentioned: The first affects the intra-lung material. At the moment the lung is filled with air which results in a non-realistic density. Appropriate foam (e. g. polyurethane (PU)) might be inserted to introduce tissue equivalent range changes within the lung. The second improvement can be done on the thorax motion control. So far only the target can do irregular motion. Using a new more elaborate motion controller more realistic breathing motion trajectories may be introduced to also get closer to realistic patient breathing signals.

Thus, a very flexible complex motion phantom is now available which is the basis of future correlation studies for gated irradiations. But beyond that, more possible fields of application exist. Focussing on ion irradiation there are also other motion mitigation techniques which rely on motion monitoring and/or could also be tested in a more complex phantom than the water phantom which is used in our group. Beam tracking [Groezinger et al., 2004] and its new implementations [Lüchtenborg et al., 2011] can be candidates as well as implementations of breathing synchronized flavours of rescanning [Furukawa et al., 2010a]. The phantom was designed for the use with carbon ions, but it can also be used for photon or proton irradiations. Testing of new techniques for beam tracking using photons [Schweikard et al., 2004] may be a field of application as well as dosimetric validation of motion prediction techniques [Hoisak et al., 2006; Kanoulas et al., 2007; Schweikard et al., 2004; Spadea et al., 2010]. Baroni et al. are currently using the phantom for testing their prediction methods during a beam time at GSI. Furthermore, ideas came up to use the phantom for 4D imaging validation purposes. Usage with magnetic resonance imaging (MRI) is not possible due to the metal components, but validation experiments for 4D position emission tomography (PET) which can be used for verification of treatment delivery in ion therapy [Parodi et al., 2005, 2007] are performable using the phantom. The target holder can easily be equipped with a target appropriate for PET. This flexibility in respect of target detector implies that the phantom can also be used for biological experiments such as cell survival measurements as performed by [Gemmel et al., 2010].

One further application of such a phantom can be the investigation of different motion monitoring systems. Plenty of sensors are commercially available monitoring different surrogate quantities. Two of such sensors are available at the university clinic Heidelberg where HIT belongs to. When introducing new beam delivery techniques for patient treatments where a motion monitoring system is mandatory, the question arises which motion monitoring system has optimal performance. Thus, two sensors, the VisionRT system (AlignRT®/GateRT®– VisionRT Ltd., London, UK) and the Anzai system (RGS AZ-733V – Anzai Medical Co.,Ltd, Tokyo, Japan), were investigated in the course of this work (chapter 5).

Besides estimation of gating delays caused by the signal processing of the two systems patient data was analysed in respect of correlation of the systems to internal tumour motion. This internal motion was acquired using MV-fluoroscopy during normal photon treatment to avoid introduction of additional dose to the patient. Results showed that gating delays of the VisionRT system are larger than for the Anzai system which is reasonable due to the larger sampling interval. In the patient data both systems showed phase shifts, base line drifts or even sudden jumps in the motion signal leading to lower correlation coefficients. Both systems showed in some cases very good correlation to the internal motion while in other cases the situation turned out to be worse. Results gave the impression that phase shifts may depend on the position where the external motion signal is acquired: Breast motion seems to be phase shifted from abdominal motion. In general no difference between the two systems related to correlation can be derived from the results. However, results are only based on the data of 5 patients. More data would be necessary to generalize the conclusions drawn from these results. The VisionRT system offers much more flexibility compared to the Anzai system e. g. in terms of tracking point selection. Therefore, it is necessary to use this flexibility in the right way to take advantages from that. In this context an investigation of the dependencies of the VisionRT tracking point on correlation results may be interesting to investigate. The current version of the phantom which was developed, built and validated in the course of this work offers the possibility to further investigate motion sensors. At HIT the Anzai system will be used for patient irradiations, but there are also plans to install a VisionRT system in the treatment rooms since it is also capable of assisting in patient setup.

7 Summary

About 50 % of cancer patients are treated with radiation therapy. A special flavour of this treatment type is particle therapy which offers the potential of higher biological effectiveness and increased sparing of normal tissue due to better target conformity. The latter advantage can further be increased by using a special delivery technique: the 3D pencil beam scanning. In this technique numerous beam spots overlap laterally and Bragg-peaks overlap longitudinally to a homogeneous dose distribution if beam parameters are set appropriately. For stationary tumours patient treatment using particle therapy was very successful. However, if tumours are located in organs affected by motion (e. g. due to respiration) the situation gets more complicated. In addition to the geometrical displacement range changes and the interplay effect (in case of scanned beams) have to be taken into account to accomplish satisfactory dose distributions.

One technique to mitigate target motion effects is gating which means pausing the irradiation while the tumour is outside the target volume. This approach increases treatment time, but decreases the effective motion amplitude. However, even for a small residual motion the interplay effect can cause inhomogeneous dose distributions. To mitigate this a beam parameter study was performed in the course of this work to investigate how changes of beam parameters effect the resulting dose distribution. In measurements and simulations 18 beam parameter combinations for up to 10 residual motion amplitudes and several starting phases were investigated. Results show that increased beam focus size highly increase homogeneity of the target dose while reduction of the distance between the beam spots doesn't. Thus, beam focus size is more important than the actual overlap. Longitudinally using smaller distances between the overlapping Bragg-peaks also increased homogeneity in the target volume.

To ensure that the tumour is within the target volume while the dose is delivered appropriate motion monitoring systems are needed. Often surrogates are used for which a correlation to the actual motion is essential. To provide a setup to investigate dosimetric effects of miscorrelation in this work a complex moving thorax phantom was designed, constructed and validated. 6D tumour motion can be performed independently from thorax motion. The phantom comprises ribs to generate range changes and an ionization chamber array as well as multiple films for target dose measurements. Basic functionality and capability of absolute dose measurements were successfully validated.

As mentioned above correlation of surrogate and internal motion is important and, furthermore, short reaction times are needed to ensure that the beam is gated correctly synchronized to the target motion. To investigate these issues two commercially available motion monitoring systems, the VisionRT system and the Anzai system were compared in the third part of this work.

Gating delays were estimated experimentally and for 5 patients correlation between surrogate motion and internal tumour motion was studied. Gating delays of the VisionRT system turned out to be higher than for the Anzai system. In respect of correlation no basic difference between the two systems can be concluded. The VisionRT system is more complex than the Anzai system which increases the application possibilities, but also the requirements to the user.

In summary in this work several aspects were investigated and knowledge was gained to get closer to the first gated patient treatment at HIT. First patient treatments of liver tumours that were motion constrained by abdominal compression were performed at HIT using knowledge gained from the beam parameter study. At first the Anzai system will be used for gating, but there are plans to also install a VisionRT system in the treatment rooms. Furthermore, due to the new phantom now an instrument is available which can be used in various fields of application in conjunction with moving target irradiation or imaging. The phantom was already used in the course of this work. Moreover first studies of internal and external groups are planned or in progress using the new phantom.

A Supplementary details on the sensor evaluation results

A.1 Gating delays of the Anzai system

Table A.1.: Measured gating delays of the Anzai system. Besides the number of gating windows (N_{GW}) which were analysed per measurement the mean, standard deviation (SD), minimum and maximum of the start delay Δt_{Start} and the stop delay Δt_{Stop}, respectively, are given.

#	N_{GW}	Δt_{Start} Mean [ms]	SD [ms]	Min [ms]	Max [ms]	Δt_{Stop} Mean [ms]	SD [ms]	Min [ms]	Max [ms]
1	68	68	8	46	78	74	10	58	87
2	91	137	14	117	156	90	11	75	126
3	105	103	12	82	131	104	9	91	143
4	87	119	11	107	146	136	10	102	152
5	90	108	10	92	124	119	8	108	138
6	95	109	6	92	131	119	10	103	135
7	63	138	7	131	165	142	5	117	149
8	66	99	6	91	114	102	10	89	121
9	87	59	10	44	77	59	10	42	75
10	85	80	6	63	102	93	10	76	112
11	63	99	9	80	112	102	8	93	122
12	59	89	11	78	112	104	5	81	113
13	61	84	8	76	105	89	8	81	113

A.2 Gating delays of the VisionRT system

Table A.2.: For each day and measurement the number of gating windows (N_{GW}), the mean and standard deviation (SD) of the sampling interval (SaI) and the mean, the standard deviation (SD), the maximum and minimum start Δt_{Start} and the stop delay Δt_{Stop}, respectively, is listed.

Day	#	N_{GW}	SaI		Δt_{Start}				Δt_{Stop}			
			Mean [ms]	SD [ms]	Mean [ms]	SD [ms]	Min [ms]	Max [ms]	Mean [ms]	SD [ms]	Min [ms]	Max [ms]
1	1	116	78	10	165	26	108	250	181	30	125	260
1	2	120	80	11	160	31	93	256	136	28	82	229
1	3	99	81	12	153	31	100	245	136	24	89	180
1	4	113	80	11	174	33	112	265	152	25	100	236
1	5	102	81	12	166	28	112	251	147	26	91	226
1	6	90	81	12	152	31	93	240	130	27	75	223
1	7	99	81	12	164	30	109	253	143	28	86	216
1	8	101	80	11	162	27	102	249	140	28	83	220
1	9	100	81	12	162	27	109	250	136	26	87	195
1	10	98	81	12	164	32	111	259	139	28	89	227
2	1	97	74	2	112	23	70	158	100	21	63	136
2	2	100	74	2	115	23	75	174	100	21	63	138
2	3	103	74	2	117	22	71	164	128	22	88	165
2	4	113	75	3	134	24	89	188	141	24	98	201
2	5	90	75	5	130	25	77	182	138	22	98	176
2	6	99	75	6	136	25	87	188	144	23	102	190
2	7	99	75	5	117	23	71	177	124	23	80	168
2	8	108	74	4	110	23	60	165	123	22	82	163
2	9	117	74	2	101	23	54	148	118	22	77	155
3	1	112	74	2	125	22	81	168	115	22	76	153
3	2	81	74	2	117	22	79	156	105	22	67	147
3	3	98	74	3	127	22	84	170	113	21	74	151
3	4	94	74	3	112	22	72	158	103	21	65	143
3	5	85	74	2	128	22	88	168	115	22	76	155
3	6	87	74	1	99	22	59	139	87	22	45	127
3	7	84	74	3	115	22	73	156	102	22	63	144

Continued on next page

Table A.2 – continued from previous page

Day	#	N_{GW}	SaI		$\Delta t_{\mathrm{Start}}$				Δt_{Stop}			
			Mean [ms]	SD [ms]	Mean [ms]	SD [ms]	Min [ms]	Max [ms]	Mean [ms]	SD [ms]	Min [ms]	Max [ms]
3	8	83	74	2	118	22	75	159	103	22	62	143
4	1	96	74	2	131	23	88	175	125	21	87	164
4	2	107	74	3	133	23	89	177	125	21	90	162
4	3	105	74	1	135	22	93	175	129	22	87	171
4	4	119	74	3	124	22	82	163	119	22	81	163
4	5	118	74	1	121	23	77	167	115	22	72	156
4	6	106	74	3	138	23	93	181	131	22	89	174
4	7	105	74	2	128	22	86	170	122	21	82	159
4	8	93	74	3	146	23	103	195	138	22	102	196
4	9	94	74	2	134	23	90	180	130	21	91	167
4	10	104	74	3	132	22	91	170	125	21	86	169
4	11	114	74	3	138	22	98	185	130	22	89	170
5	1	102	78	9	125	27	66	189	137	26	81	209
5	2	112	79	10	120	24	69	174	140	27	86	223
5	3	103	79	10	126	27	71	230	145	25	95	226
5	4	95	79	10	141	26	86	193	158	28	103	244
5	5	99	79	10	141	26	91	212	160	28	109	256
5	6	95	78	10	131	24	77	195	155	30	99	250
5	7	87	78	10	134	25	87	194	160	28	106	247
5	8	96	79	11	127	24	80	192	146	28	93	224
5	9	91	78	10	127	25	82	177	149	28	93	238
5	10	104	79	10	121	25	78	172	142	28	90	224
5	11	107	78	10	127	25	82	188	152	29	96	232

A.3 Correlation coefficients

Table A.3.: Correlation coefficients (CC) for Anzai versus VisionRT. For normalized and non-normalized motion traces the CC as well as the phase shift corrected CCs based on ϕ_{MM} and ϕ_{CC} are given. $|CC|^{NB}_{CC}$ represents the correlation results for VisionRT cases without beam status.

PatID	Fraction	Field	A	V	F	$\lvert CC\rvert$	$\lvert CC\rvert_{MM}$	$\lvert CC\rvert_{CC}$	$\lvert CC\rvert^{Norm}_{MM}$	$\lvert CC\rvert^{Norm}_{CC}$	$\lvert CC\rvert^{NB}_{CC}$
1	1	1	✓	✓		−0.42	−0.01	0.04	0.79	0.8	
1	1	2	✓	✓		0.35	0.77	0.78	0.8	0.79	
1	1	3	✓	✓		−0.01	0.64	0.67	0.86	0.87	
1	1	4	✓	✓		0.28	0.72	0.72	0.85	0.86	
1	1	5	✓	✓	✓	0.06	0.68	0.7	0.73	0.73	
1	2	1	✓	✓		0.24	0.41	0.43	0.88	0.88	
1	2	2	✓	✓		0.79	0.81	0.81	0.88	0.92	
1	2	3	✓	✓		0.09	0.11	0.15	0.7	0.73	
1	2	4	✓	✓		0.6	0.62	0.65	0.75	0.77	
1	2	5	✓	✓	✓	0.11	0.41	0.44	0.76	0.78	
1	3	1	✓	✓		0.8	0.84	0.84	0.81	0.82	
1	3	2	✓	✓		0.32	0.76	0.76	0.64	0.67	
1	3	3	✓	✓		0.23	0.67	0.66	0.82	0.83	
1	3	4	✓	✓		0.69	0.83	0.8	0.82	0.85	
1	3	5	✓	✓	✓	0.44	0.7	0.72	0.86	0.86	
2	1	6	✓	(✓)	✓						0.58
3	1	4	✓	(✓)	✓						0.99
3	1	5	✓	(✓)	✓						0.99
3	1	6	✓	(✓)	✓						0.98
3	1	7	✓	(✓)	✓						0.99
3	2	4	✓	(✓)	✓						1.00
3	2	6	✓	(✓)	✓						0.99
3	2	7	✓	(✓)	✓						0.99
3	3	4	✓	(✓)	✓						0.99
3	3	5	✓	(✓)	✓						0.98
3	3	6	✓	(✓)	✓						0.99
3	3	7	✓	(✓)	✓						0.99
3	4	4	✓	(✓)	✓						0.99

Continued on next page

Table A.3 – continued from previous page

PatID	Fraction	Field	A	V	F	$\lvert CC \rvert$	$\lvert CC \rvert_{MM}$	$\lvert CC \rvert_{CC}$	$\lvert CC \rvert^{Norm}_{MM}$	$\lvert CC \rvert^{Norm}_{CC}$	$\lvert CC \rvert^{NB}_{CC}$
3	4	5	✓	(✓)	✓						0.99
3	4	6	✓	(✓)	✓						0.98
3	4	7	✓	(✓)	✓						0.93
3	5	4	✓	(✓)	✓						0.98
3	5	5	✓	(✓)	✓						0.96
3	5	6	✓	(✓)	✓						0.96
3	5	7	✓	(✓)	✓						0.93
4	1	5	✓	✓		0.97	0.98	0.98	0.96	0.99	
4	1	6	✓	✓		0.96	0.98	0.98	0.94	0.98	
5	1	3	✓	(✓)	✓						0.90

Table A.4.: Correlation coefficients (CC) for Anzai versus fluoroscopy. For normalized and non-normalized motion traces the CC as well as the phase shift corrected CCs based on ϕ_{MM} and ϕ_{CC} are given.

PatID	Fraction	Field	A	V	F	$\lvert CC\rvert$	$\lvert CC\rvert_{MM}$	$\lvert CC\rvert_{CC}$	$\lvert CC\rvert^{Norm}_{MM}$	$\lvert CC\rvert^{Norm}_{CC}$
1	1	5	✓	✓	✓	−0.64	−0.66	−0.72	−0.97	−0.97
1	2	5	✓	✓	✓	−0.75	−0.75	−0.76	−0.96	−0.97
1	3	5	✓	✓	✓	−0.92	−0.93	−0.94	−0.96	−0.98
2	1	6	✓	(✓)	✓	−0.9	−0.9	−0.92	−0.9	−0.93
3	1	2	✓		✓	−0.92	−0.92	−0.93	−0.92	−0.94
3	1	3	✓		✓	0.46	0.48	−0.79	0.48	−0.82
3	1	4	✓	(✓)	✓	−0.7	−0.73	−0.82	−0.95	−0.95
3	1	5	✓	(✓)	✓	−0.87	−0.87	−0.89	−0.89	−0.91
3	1	6	✓	(✓)	✓	−0.53	−0.53	−0.51	−0.85	−0.87
3	1	7	✓	(✓)	✓	−0.87	−0.88	−0.9	−0.93	−0.96
3	2	2	✓		✓	−0.93	−0.93	−0.93	−0.93	−0.94
3	2	3	✓		✓	−0.95	−0.95	−0.95	−0.96	−0.98
3	2	4	✓	(✓)	✓	−0.65	−0.7	−0.74	−0.95	−0.96
3	2	6	✓	(✓)	✓	−0.65	−0.62	−0.62	−0.9	−0.92
3	2	7	✓	(✓)	✓	−0.68	−0.68	−0.67	−0.91	−0.94
3	3	2	✓		✓	−0.68	−0.68	−0.75	−0.92	−0.96
3	3	3	✓		✓	−0.71	−0.68	−0.79	−0.9	−0.97
3	3	4	✓	(✓)	✓	−0.69	−0.72	−0.77	−0.89	−0.89
3	3	5	✓	(✓)	✓	−0.54	−0.53	−0.61	−0.84	−0.83
3	3	6	✓	(✓)	✓	−0.91	−0.91	−0.92	−0.93	−0.93
3	3	7	✓	(✓)	✓	−0.77	−0.79	−0.8	−0.93	−0.94
3	4	2	✓		✓	−0.59	−0.59	−0.74	−0.81	−0.89
3	4	3	✓		✓	−0.9	−0.92	−0.94	−0.95	−0.96
3	4	4	✓	(✓)	✓	−0.71	−0.78	−0.8	−0.92	−0.92
3	4	5	✓	(✓)	✓	−0.64	−0.64	−0.61	−0.84	−0.86
3	4	6	✓	(✓)	✓	−0.85	−0.82	−0.87	−0.86	−0.94
3	4	7	✓	(✓)	✓	−0.83	−0.64	−0.85	−0.63	−0.93
3	5	2	✓		✓	−0.85	−0.87	−0.88	−0.89	−0.9
3	5	3	✓		✓	−0.84	−0.9	−0.91	−0.92	−0.93
3	5	4	✓	(✓)	✓	−0.8	−0.8	−0.83	−0.88	−0.89
3	5	5	✓	(✓)	✓	−0.63	−0.67	−0.69	−0.75	−0.75

Continued on next page

Table A.4 – continued from previous page

PatID	Fraction	Field	A	V	F	$\lvert CC \rvert$	$\lvert CC \rvert_{MM}$	$\lvert CC \rvert_{CC}$	$\lvert CC \rvert_{MM}^{Norm}$	$\lvert CC \rvert_{CC}^{Norm}$
3	5	6	✓	(✓)	✓	−0.55	−0.57	−0.62	−0.8	−0.84
3	5	7	✓	(✓)	✓	−0.74	−0.78	−0.82	−0.84	−0.84
4	1	3	✓		✓	−0.85	−0.85	−0.9	−0.94	−0.95
4	1	4	✓		✓	−0.54	−0.54	−0.61	−0.92	−0.93
5	1	2	✓		✓	−0.63	−0.62	−0.7	−0.97	−0.98
5	1	3	✓	(✓)	✓	−0.36	−0.37	−0.48	−0.96	−0.97
5	1	4	✓		✓	−0.65	−0.61	−0.74	−0.93	−0.94

Table A.5.: Correlation coefficients (CC) for VisionRT versus fluoroscopy. For normalized and non-normalized motion traces the CC as well as the phase shift corrected CCs based on ϕ_{MM} and ϕ_{CC} are given. $|\mathrm{CC}|^{\mathrm{NB}}_{\mathrm{CC}}$ represents the correlation results for VisionRT cases without beam status.

PatID	Fraction	Field	A	V	F	$\|\mathrm{CC}\|$	$\|\mathrm{CC}\|_{\mathrm{MM}}$	$\|\mathrm{CC}\|_{\mathrm{CC}}$	$\|\mathrm{CC}\|^{\mathrm{Norm}}_{\mathrm{MM}}$	$\|\mathrm{CC}\|^{\mathrm{Norm}}_{\mathrm{CC}}$	$\|\mathrm{CC}\|^{\mathrm{NB}}_{\mathrm{CC}}$
1	1	5	✓	✓	✓	0.22	−0.35	−0.49	−0.73	−0.76	
1	2	5	✓	✓	✓	−0.47	−0.8	−0.82	−0.8	−0.82	
1	3	5	✓	✓	✓	−0.19	−0.55	−0.63	−0.81	−0.84	
2	1	6	✓	(✓)	✓						−0.56
3	1	4	✓	(✓)	✓						−0.73
3	1	5	✓	(✓)	✓						−0.86
3	1	6	✓	(✓)	✓						−0.54
3	1	7	✓	(✓)	✓						−0.87
3	2	4	✓	(✓)	✓						−0.69
3	2	6	✓	(✓)	✓						−0.68
3	2	7	✓	(✓)	✓						−0.71
3	3	4	✓	(✓)	✓						−0.71
3	3	5	✓	(✓)	✓						−0.55
3	3	6	✓	(✓)	✓						−0.92
3	3	7	✓	(✓)	✓						−0.79
3	4	4	✓	(✓)	✓						−0.77
3	4	5	✓	(✓)	✓						−0.64
3	4	6	✓	(✓)	✓						−0.85
3	4	7	✓	(✓)	✓						−0.78
3	5	4	✓	(✓)	✓						−0.82
3	5	5	✓	(✓)	✓						−0.70
3	5	6	✓	(✓)	✓						−0.62
3	5	7	✓	(✓)	✓						−0.86
5	1	3	✓	(✓)	✓						−0.29

Bibliography

H. Alasti, Y. B. Cho, A. D. Vandermeer, A. Abbas, B. Norrlinger, S. Shubbar, and A. Bezjak. A novel four-dimensional radiotherapy method for lung cancer: imaging, treatment planning and delivery. *Physics in Medicine & Biology*, 51(12):3251–3267, 2006.

H. H. Andersen and J. F. Ziegler. *Hydrogen: Stopping Powers and Ranges in All Elements*. Pergamon Press, first edition, 1977.

Anzai. *AZ 773V Users's Manual*, 2011. Version: 3.0AW1.

O. Avila, I. Gamboa-deBuen, and M. E. Brandan. Study of the energy deposition in LiF by heavy charged particle irradiation and its relation to the thermoluminescent efficiency of the material. *Journal of Physics D*, 32(10):1175–1181, 1999.

W. H. Barkas. *Techniques and Theory*. Nuclear Research Emulsions. Academic Press, 1963.

W. H. Barkas and M. J. Berger. Table of Energy Loss and Ranges of Heavy Charged Particles. *NASA Report*, SP-3013, 1964.

W. H. Barkas, W. Birnbaum, and F. M. Smith. Mass-Ratio Method Applied to the Measurement of L-Meson Masses and the Energy Balance in Pion Decay. *Physical Review*, 101(2):778–795, 1956.

A. S. Beddar, K. Kainz, T. M. Briere, Y. Tsunashima, T. Pan, K. Prado, R. Mohan, M. Gillin, and S. Krishnan. Correlation between internal fiducial tumor motion and external marker motion for liver tumors imaged with 4D-CT. *International Journal of Radiation Oncology*Biology*Physics*, 67(2):630–638, 2007.

M. Belli, F. Cera, R. Cherubini, M. Dalla Vecchia, A. M. Haque, F. Ianzini, G. Moschini, O. Sapora, G. Simone, M. A. Tabocchini, and P. Tiveron. RBE-LET relationships for cell inactivation and mutation induced by low energy protons in V79 cells: further results at the LNL facility. *International Journal of Radiation Biology*, 74(4):501–509, 1998.

A. M. Berson, R. Emery, L. Rodriguez, G. M. Richards, T. Ng, S. Sanghavi, and J. Barsa. Clinical experience using respiratory gated radiation therapy: Comparison of free-breathing and breath-hold techniques. *International Journal of Radiation Oncology*Biology*Physics*, 60(2): 419–426, 2004.

C. Bert and M. Durante. Motion in radiotherapy: particle therapy. *Physics in Medicine & Biology*, 56(16):R113–R144, 2011.

C. Bert and E. Rietzel. 4D treatment planning for scanned ion beams. *Radiation Oncology*, 2 (24), 2007.

C. Bert, N. Saito, A. Schmidt, N. Chaudhri, D. Schardt, and E. Rietzel. Target motion tracking with a scanned particle beam. *Medical Physics*, 34(12):4768–4771, 2007.

C. Bert, S. O. Groezinger, and E. Rietzel. Quantification of interplay effects of scanned particle beams and moving targets. *Physics in Medicine & Biology*, 53(9):2253–2265, 2008.

C. Bert, A. Gemmel, N. Saito, and E. Rietzel. Gated irradiation with scanned particle beams. *International Journal of Radiation Oncology*Biology*Physics*, 73(4):1270–1275, 2009.

C. Bert, A. Gemmel, N. Saito, N. Chaudhri, D. Schardt, M. Durante, G. Kraft, and E. Rietzel. Dosimetric precision of an ion beam tracking system. *Radiation Oncology*, 5(61), 2010.

J. Besserer, P. Bilski, J. de Boer, T. Kwiecien, M. Moosburger, P. Olko, and P. Quicken. Dosimetry of low-energy protons and light ions. *Physics in Medicine & Biology*, 46(2):473–485, 2001.

H. Bethe. Zur Theorie des Durchgangs schneller Korpuskularstrahlung durch Materie. *Annalen der Physik*, 5(5):325–400, 1930.

H. Bichsel. Stopping power and ranges of fast ions in heavy elements. *Physical Review A*, 46(9): 5761–5773, 1992.

J. Biederer and M. Heller. Artificial thorax for MR imaging studies in porcine heart-lung preparations. *Radiology*, 226(1):250–255, 2003.

P. Bilski, M. Budzanowski, W. Hoffmann, A. Molokanov, P. Olko, and M. Waligorski. Investigation of Efficiency of Thermoluminescence Detectors for Particle Therapy Beams. *Radiation Protection Dosimetry*, 70(1–4):501–504, 1997.

P. Binns and J. Hough. Secondary Dose Exposures During 200 MeV Proton Therapy. *Radiation Protection Dosimetry*, 70(1–4):441–444, 1997.

F. Bloch. Zur Bremsung rasch bewegter Teilchen beim Durchgang durch Materie. *Annalen der Physik*, 5(16):285–321, 1933a.

F. Bloch. Bremsvermoegen von Atomen mit mehreren Elektronen. *Zeitschrift für Physik A*, 81 (5–6):363–376, 1933b.

BNL. Chart of Nuclides. http://www.nndc.bnl.gov/chart/. Internet source accessed on July 28th, 2011.

T. Bortfeld, K. Jokivarsi, M. Goitein, K. J, and S. B. Jiang. Effects of intra-fraction motion on IMRT dose delivery: statistical analysis and simulation. *Physics in Medicine & Biology*, 47(13): 2203–2220, 2002.

R. Brevet. Internal/External Motion Correlation. Master's thesis, Université de Strasbourg, 2011.

K. R. Britton, G. Starkschall, S. L. Tucker, T. Pan, C. Nelson, J. Y. Chang, J. D. Cox, R. Mohan, and R. Komaki. Assessment of gross tumor volume regression and motion changes during radiotherapy for non-small-cell lung cancer as measured by four-dimensional computed tomography. *International Journal of Radiation Oncology*Biology*Physics*, 68(4):1036–1046, 2007.

A. Chandra, L. Dong, E. Huang, D. A. Kuban, L. O'Neill, I. Rosen, and A. Pollack. Experience of ultrasound-based daily prostate localization. *International Journal of Radiation Oncology*Biology*Physics*, 56(2):436–447, 2003.

N. Chaudhri, N. Saito, C. Bert, B. Franczak, P. Steidl, M. Durante, E. Rietzel, and D. Schardt. Ion-optical studies for a range adaptation method in ion beam therapy using a static wedge degrader combined with magnetic beam deflection. *Physics in Medicine & Biology*, 55(12): 3499–3513, 2010.

W. T. Chu, B. A. Ludewigt, and T. R. Renner. Instrumentation for treatment of cancer using proton and light-ion beams. *Review of Scientific Instruments*, 64(8):2055–2122, 1993.

C. S. Chui, E. Yorke, and L. Hong. The effects of intra-fraction organ motion on the delivery of intensity-modulated field with a multileaf collimator. *Medical Physics*, 30(7):1736–1746, 2003.

L. Dietrich, T. Tncking, S. Nill, and U. Oelfke. Compensation for respiratory motion by gated radiotherapy: an experimental study. *Physics in Medicine & Biology*, 50(10):2405–2414, 2005.

W. D'Souza, Y. Kwok, C. Deyoung, N. Zacharapoulos, M. Pepelea, P. Klahr, and C. X. Yu. Gated CT imaging using a free-breathing respiration signal from flow-volume spirometry. *Medical Physics*, 32(12):3641–3649, 2005.

M. Durante and J. S. Loeffler. Charged particles in radiation oncology. *Nature Reviews Clinical Oncology*, 7(1):37–43, 2010.

P. M. Evans. Anatomical imaging for radiotherapy. *Physics in Medicine & Biology*, 53(12):R151–R191, 2008.

D. S. Followill, D. R. Evans, C. Cherry, A. Molineu, G. Fisher, W. F. Hanson, and G. S. Ibbott. Design, development, and implementation of the radiological physics center's pelvis and thorax anthropomorphic quality assurance phantoms. *Medical Physics*, 34(6):2070–2076, 2007.

E. C. Ford, G. S. Mageras, E. Yorke, and C. C. Ling. Respiration-correlated spiral CT: A method of measuring respiratory-induced anatomic motion for radiation treatment planning. *Medical Physics*, 30(1):88–97, 2003.

T. Furukawa, T. Inaniwa, S. Sato, T. Tomitani, S. Minohara, K. Noda, and T. Kanai. Design study of a raster scanning system for moving target irradiation in heavy-ion radiotherapy. *Medical Physics*, 34(3):1085–1097, 2007.

T. Furukawa, T. Inaniwa, S. Sato, T. Shirai, S. Mori, E. Takeshita, K. Mizushima, T. Himukai, and K. Noda. Moving target irradiation with fast rescanning and gating in particle therapy. *Medical Physics*, 37(9):4874–4879, 2010a.

T. Furukawa, T. Inaniwa, S. Sato, T. Shirai, Y. Takei, E. Takeshita, K. Mizushima, Y. Iwata, T. Himukai, S. Mori, S. Fukuda, S. Minohara, E. Takada, T. Murakami, and K. Noda. Performance of the NIRS fast scanning system for heavy-ion radiotherapy. *Medical Physics*, 37 (11):5672–5682, 2010b.

Y. Furusawa, K. Fukutsu, M. Aoki, H. Itsukaichi, K. Eguchi-Kasai, H. Ohara, F. Yatagai, T. Kanai, and K. Ando. Inactivation of aerobic and hypoxic cells from three different cell lines by accelerated (3)He-, (12)C- and (20)Ne-ion beams. *Radiation Research*, 154(5):485–496, 2000.

A. Gemmel, C. Bert, N. Saito, N. C. von, G. Iancu, W. Weyrather, M. Durante, and E. Rietzel. Development and performance evaluation of a dynamic phantom for biological dosimetry of moving targets. *Physics in Medicine & Biology*, 55(11):2997–3009, 2010.

D. P. Gierga, J. Brewer, G. C. Sharp, M. Betke, C. G. Willett, and G. T. Y. Chen. The correlation between internal and external markers for abdominal tumors: Implications for respiratory gating. *International Journal of Radiation Oncology*Biology*Physics*, 61(5):1551–1558, 2005.

S. O. Groezinger. *Volume Conformal Irradiation of Moving Target Volumes with Scanned Ion Beams*. PhD thesis, TU Darmstadt, 2004.

S. O. Groezinger, Q. Li, E. Rietzel, T. Haberer, and G. Kraft. 3D online compensation of target motion with scanned particle beam. *Radiotherapy and Oncology*, 73(Supplement 2):S77–S79, 2004.

S. O. Groezinger, E. Rietzel, Q. Li, C. Bert, T. Haberer, and G. Kraft. Simulations to design an online motion compensation system for scanned particle beams. *Physics in Medicine & Biology*, 51(14):3517–3531, 2006.

T. Haberer, W. Becher, D. Schardt, and G. Kraft. Magnetic scanning system for heavy ion therapy. *Nuclear Instruments & Methods in Physics Research, Section A*, 330(1–2):296–305, 1993.

T. Haberer, J. Debus, H. Eickhoff, O. Jaekel, D. Schulz-Ertner, and U. Weber. The Heidelberg Ion Therapy Center. *Radiotherapy and Oncology*, 73(Supplement 2):S186–S190, 2004.

E. J. Hall and A. J. Giaccia. *Radiobiology for the Radiologist*. Lipincott Williams & Wilkins, seventh edition, 2011.

B. Hartmann, M. Martisikova, and O. Jakel. Homogeneity of Gafchromic EBT2 film. *Medical Physics*, 37(4):1753–1756, 2010.

HIT. HIT press picture. http://www.klinikum.uni-heidelberg.de/Bildergalerien.117970.0.html. Internet source accessed on September 8th, 2011.

J. D. Hoisak, K. E. Sixel, R. Tirona, P. C. Cheung, and J. P. Pignol. Prediction of lung tumour position based on spirometry and on abdominal displacement: accuracy and reproducibility. *Radiotherapy and Oncology*, 78(3):339–346, 2006.

J. D. P. Hoisak, K. E. Sixel, R. Tirona, P. C. F. Cheung, and J. P. Pignol. Correlation of lung tumor motion with external surrogate indicators of respiration. *International Journal of Radiation Oncology*Biology*Physics*, 60(4):1298–1306, 2004.

Y. Horowitz. Mathematical Modelling of TL Supralinearity for Heavy Charged Particles. *Radiation Protection Dosimetry*, 33(1–4):75–81, 1990.

Y. Horowitz and N. Stern. Relative Thermoluminescent Efficiency of LiF:Cu,Mg,P to Alpha Particles: Theory and Experiment. *Radiation Protection Dosimetry*, 33(1–4):287–290, 1990.

S. Hughes, J. McClelland, S. Tarte, D. Lawrence, S. Ahmad, D. Hawkes, and D. Landau. Assessment of two novel ventilatory surrogates for use in the delivery of gated/tracked radiotherapy for non-small cell lung cancer. *Radiotherapy and Oncology*, 91(3):336–341, 2009.

IAEA. Absorbed dose determination in external beam radiotherapy: an international code of practice for dosimetry based on standards of absorbed dose to water. *IAEA Technical Report Series*, 398, 2000.

IARC. GLOBOCAN 2008. http://globocan.iarc.fr/factsheets/populations/factsheet.asp?uno=900. Internet source accessed on July 26th, 2011.

ICRU. Stopping Power and Ranges for Protons and Alpha Particles. *ICRU Report*, 49, 1993a.

ICRU. Prescribing, Recording, and Reporting Photon Beam Therapy. *ICRU Report*, 50, 1993b.

ICRU. Prescribing, Recording and Reporting Photon Beam Therapy (Supplement to ICRU Report 50). *ICRU Report*, 62, 1999.

D. Ionascu, S. B. Jiang, S. Nishioka, H. Shirato, and R. I. Berbeco. Internal-external correlation investigations of respiratory induced motion of lung tumors. *Medical Physics*, 34(10):3893–3903, 2007.

O. Jaekel, C. Jacob, D. Schardt, C. P. Karger, and G. H. Hartmann. Relation between carbon ion ranges and x-ray CT numbers. *Medical Physics*, 28(4):701–703, 2001.

S. B. Jiang, C. Pope, K. M. A. Jarrah, J. H. Kung, T. Bortfeld, and G. T. Y. Chen. An experimental investigation on intra-fractional organ motion effects in lung IMRT treatments. *Physics in Medicine & Biology*, 48(12):1773–1784, 2003.

T. Kanai, M. Endo, S. Minohara, N. Miyahara, H. Koyama-ito, H. Tomura, N. Matsufuji, Y. Futami, A. Fukumura, and H. e. a. Takeshi. Biophysical characteristics of HIMAC clinical irradiation system for heavy-ion radiation therapy. *International Journal of Radiation Oncology*Biology*Physics*, 44(1):201–210, 1999.

E. Kanoulas, J. A. Aslam, G. C. Sharp, R. I. Berbeco, S. Nishioka, H. Shirato, and S. B. Jiang. Derivation of the tumor position from external respiratory surrogates with periodical updating of the internal/external correlation. *Physics in Medicine & Biology*, 52(17):5443–5456, 2007.

C. P. Karger, O. Jaekel, and G. H. Hartmann. A system for three-dimensional dosimetric verification of treatment plans in intensity-modulated radiotherapy with heavy ions. *Medical Physics*, 26(10):2125–2132, 1999.

C. P. Karger, O. Jakel, H. Palmans, and T. Kanai. Dosimetry for ion beam radiotherapy. *Physics in Medicine & Biology*, 55(21):R193–R234, 2010.

R. Kashani, K. Lam, D. Litzenberg, and J. Balter. Technical note: a deformable phantom for dynamic modeling in radiation therapy. *Medical Physics*, 34(1):199–201, 2007.

P. J. Keall, V. R. Kini, S. S. Vedam, and R. Mohan. Motion adaptive x-ray therapy: a feasibility study. *Physics in Medicine & Biology*, 46(1):1–10, 2001.

P. J. Keall, H. Cattell, D. Pokhrel, S. Dieterich, K. H. Wong, M. J. Murphy, S. S. Vedam, K. Wijesooriya, and R. Mohan. Geometric accuracy of a real-time target tracking system with dynamic multileaf collimator tracking system. *International Journal of Radiation Oncology*Biology*Physics*, 65(5):1579–1584, 2006.

G. F. Knoll. *Radiation Detection and Measurement*. John Wiley & Sohns, Inc., fourth edition, 2010.

A. Knopf, C. Bert, E. Heath, S. Nill, K. Kraus, D. Richter, E. Hug, E. Pedroni, S. Safai, F. Albertini, S. Zenklusen, D. Boye, M. Sohn, M. Soukup, B. Sobotta, and A. Lomax. Special report:

Workshop on 4D-treatment planning in actively scanned particle therapy—Recommendations, technical challenges, and future research directions. *Medical Physics*, 37(9):4608–4614, 2010.

N. Koch, H. H. Liu, G. Starkschall, M. Jacobson, K. Forster, Z. Liao, R. Komaki, and C. W. Stevens. Evaluation of internal lung motion for respiratory-gated radiotherapy using MRI: Part I?correlating internal lung motion with skin fiducial motion. *International Journal of Radiation Oncology*Biology*Physics*, 60(5):1459–1472, 2004.

A. F. Kolen, N. R. Miller, E. E. Ahmed, and J. C. Bamber. Characterization of cardiovascular liver motion for the eventual application of elasticity imaging to the liver in vivo. *Physics in Medicine & Biology*, 49(18):4187–4206, 2004.

M. Kraemer, O. Jaekel, T. Haberer, G. Kraft, D. Schardt, and U. Weber. Treatment planning for heavy-ion radiotherapy: physical beam model and dose optimization. *Physics in Medicine & Biology*, 45(11):3299–3317, 2000.

H. D. Kubo and B. C. Hill. Respiration gated radiotherapy treatment: a technical study. *Physics in Medicine & Biology*, 41(1):83–91, 1996.

J. Lambert, N. Suchowerska, D. R. McKenzie, and M. Jackson. Intrafractional motion during proton beam scanning. *Physics in Medicine & Biology*, 50(20):4853–4862, 2005.

K. M. Langen and D. T. L. Jones. Organ motion and its management. *International Journal of Radiation Oncology*Biology*Physics*, 50(1):265–278, 2001.

R. Lüchtenborg, N. Saito, M. Durante, and C. Bert. Experimental verification of a real-time compensation functionality for dose changes due to target motion in scanned particle therapy. *Medical Physics*, 38(10):5448–5798, 2011.

W. P. Levin, H. Kooy, J. S. Loeffler, and T. F. Delaney. Proton beam therapy. *British Journal of Cancer*, 93(8):849–854, 2005.

T. Li, E. Schreibmann, B. Thorndyke, G. Tillman, A. Boyer, A. Koong, K. Goodman, and L. Xing. Radiation dose reduction in four-dimensional computed tomography. *Medical Physics*, 32(12): 3650–3660, 2005.

X. A. Li, C. Stepaniak, and E. Gore. Technical and dosimetric aspects of respiratory gating using a pressure-sensor motion monitoring system. *Medical Physics*, 33(1):145–154, 2006.

J. Lindhard. The Barkas effect - or Z^3, Z^4-corrections to stopping of swift charged particles. *Nuclear Instruments & Methods*, 132:1–5, 1976.

J. Lindhard, M. Scharff, and H. E. Schltt. Range concepts and heavy ion ranges. *Matematisk-Fysiske Meddelelser / udg. af Det Kongelige Danske Videnskabernes Selskab*, 33(14):1–42, 1963.

H. H. Liu, N. Koch, G. Starkschall, M. Jacobson, K. Forster, Z. Liao, R. Komaki, and C. W. Stevens. Evaluation of internal lung motion for respiratory-gated radiotherapy using MRI: Part II: margin reduction of internal target volume. *International Journal of Radiation Oncology*Biology*Physics*, 60(5):1473–1483, 2004.

A. J. Lomax, T. Bohringer, A. Bolsi, D. Coray, F. Emert, G. Goitein, M. Jermann, S. Lin, E. Pedroni, H. Rutz, O. Stadelmann, B. Timmermann, J. Verwey, and D. C. Weber. Treatment planning and verification of proton therapy using spot scanning: Initial experiences. *Medical Physics*, 31(11):3150–3157, 2004.

H. M. Lu, R. Brett, G. Sharp, S. Safai, S. Jiang, J. Flanz, and H. Kooy. A respiratory-gated treatment system for proton therapy. *Medical Physics*, 34(8):3273–3278, 2007.

W. Lu, M. M. Nystrom, P. J. Parikh, D. R. Fooshee, J. P. Hubenschmidt, J. D. Bradley, and D. A. Low. A semi-automatic method for peak and valley detection in free-breathing respiratory waveforms. *Medical Physics*, 33(10):3634–3636, 2006a.

W. Lu, P. J. Parikh, J. P. Hubenschmidt, J. D. Bradley, and D. A. Low. A comparison between amplitude sorting and phase-angle sorting using external respiratory measurement for 4D CT. *Medical Physics*, 33(8):2964–2974, 2006b.

J. Meyer, A. Richter, K. Baier, J. Wilbert, M. Guckenberger, and M. Flentje. Tracking moving objects with megavoltage portal imaging: a feasibility study. *Medical Physics*, 33(5):1275–1280, 2006.

S. Minohara, T. Kanai, M. Endo, K. Noda, and M. Kanazawa. Respiratory gated irradiation system for heavy-ion radiotherapy. *International Journal of Radiation Oncology*Biology*Physics*, 47(4):1097–1103, 2000.

K. Nakamura et al. The Review of Particle Physics. *Journal of Physics G*, 37(7A), 2010.

J. Naumann. personal communication, 2011.

T. Neicu, H. Shirato, Y. Seppenwoolde, and S. B. Jiang. Synchronized moving aperture radiation therapy (SMART): average tumour trajectory for lung patients. *Physics in Medicine & Biology*, 48(5):587–598, 2003.

E. Nioutsikou, N. S.-T. Richard, J. L. Bedford, and S. Webb. Quantifying the effect of respiratory motion on lung tumour dosimetry with the aid of a breathing phantom with deforming lungs. *Physics in Medicine & Biology*, 51(14):3359–3374, 2006.

O. Nohadani, J. Seco, and T. Bortfeld. Motion management with phase-adapted 4D-optimization. *Physics in Medicine & Biology*, 55(17):5189–5202, 2010.

Y. Otani, I. Fukuda, N. Tsukamoto, Y. Kumazaki, H. Sekine, E. Imabayashi, O. Kawaguchi, T. Nose, T. Teshima, and T. Dokiya. A comparison of the respiratory signals acquired by different respiratory monitoring systems used in respiratory gated radiotherapy. *Medical Physics*, 37(12):6178–6186, 2010.

H. Paganetti. Significance and implementation of RBE variations in proton beam therapy. *Technology in Cancer Research and Treatment*, 2(5):413–426, 2003.

H. Paganetti, A. Niemierko, M. Ancukiewicz, L. E. Gerweck, M. Goitein, J. S. Loeffler, and H. D. Suit. Relative biological effectiveness (RBE) values for proton beam therapy. *International Journal of Radiation Oncology*Biology*Physics*, 53(2):407–421, 2002.

K. Parodi, F. Poenisch, and W. Enghardt. Experimental study on the feasibility of in-beam PET for accurate monitoring of proton therapy. *IEEE Transactions on Nuclear Science*, 52(3):778–786, 2005.

K. Parodi, H. Paganetti, H. A. Shih, S. Michaud, J. S. Loeffler, T. F. DeLaney, N. J. Liebsch, J. E. Munzenrider, A. J. Fischman, A. Knopf, and T. Bortfeld. Patient Study of In Vivo Verification of Beam Delivery and Range, Using Positron Emission Tomography and Computed Tomography Imaging After Proton Therapy. *International Journal of Radiation Oncology*Biology*Physics*, 68(3):920–934, 2007.

K. Parodi, A. Mairani, S. Brons, J. Naumann, M. Kramer, F. Sommerer, and T. Haberer. The influence of lateral beam profile modifications in scanned proton and carbon ion therapy: a Monte Carlo study. *Physics in Medicine & Biology*, 55(17):5169–5187, 2010.

E. Pedroni, R. Bacher, H. Blattmann, T. Bohringer, A. Coray, A. Lomax, S. Lin, G. Munkel, S. Scheib, U. Schneider, and A. Tourovsky. The 200-MeV proton therapy project at the Paul Scherrer Institute: Conceptual design and practical realization. *Medical Physics*, 22(1):37–53, 1995.

E. Pedroni, R. Bearpark, T. Boehringer, and A. Coray. The PSI Gantry 2: a second generation proton scanning gantry. *Zeitschrift für medizinische Physik*, 14(1):25–34, 2004.

M. H. Phillips, E. Pedroni, H. Blattmann, T. Boehringer, A. Coray, and S. Scheib. Effects of respiratory motion on dose uniformity with a charged particle scanning method. *Physics in Medicine & Biology*, 37(1):223–233, 1992.

PTCOG. Particle Therapy Co-Operative Group. http://ptcog.web.psi.ch/. Internet source accessed on August 1rst, 2011.

A. Richter, J. Wilbert, K. Baier, M. Flentje, and M. Guckenberger. Feasibility study for markerless tracking of lung tumors in stereotactic body radiotherapy. *International Journal of Radiation Oncology*Biology*Physics*, 78(2):618–627, 2010a.

D. Richter, P. Steidl, J. Trautmann, A. Schwarzkopf, M. Krämer, A. Gemmel, J. Naumann, R. Panse, N. Saito, O. Jaekel, M. Durante, and C. Bert. Mitigation of residual motion effects in scanned ion beam therapy. *Radiotherapy and Oncology*, 96(Supplement 1):S72, 2010b.

D. Richter, J. Trautmann, A. Schwarzkopf, M. Kraemermer, A. Gemmel, O. Jaekel, M. Durante, and C. Bert. 4D Treatment Planning Implementations for TRiP98. *GSI Scientific Report 2009*, page 500, 2010c.

D. Richter, J. Trautmann, A. Schwarzkopf, M. Kraemer, R. Luechtenborg, J. G. Eley, A. Gemmel, M. Durante, and C. Bert. Status of 4D Treatment Planning Implementations for TRiP98. *GSI Scientific Report 2010*, page 476, 2011.

E. Rietzel and C. Bert. Respiratory motion management in particle therapy. *Medical Physics*, 37 (2):449–460, 2010.

E. Rietzel, T. Pan, and G. T. Y. Chen. Four-dimensional computed tomography: Image formation and clinical protocol. *Medical Physics*, 32(4):874–889, 2005.

RKI. *Cancer in Germany 2005/2006. Incidence and Trends.* Seventh edition. Robert Koch Institute (ed.) and Association of Population-based Cancer Registries in Germany (ed.). Berlin 2010.

N. Saito, C. Bert, N. Chaudhri, A. Gemmel, D. Schardt, and E. Rietzel. Speed and accuracy of a beam tracking system for treatment of moving targets with scanned ion beams. *Physics in Medicine & Biology*, 54(16):4849–4862, 2009.

D. Schardt, T. Elsaesser, and D. Schulz-Ertner. Heavy-ion tumor therapy: Physical and radiobiological benefits. *Reviews of Modern Physics*, 82(1):383–425, 2010.

M. Scholz. Effects of ion radiation on cells and tissues. *Advances in Polymer Science*, 162:95–155, 2003.

M. Scholz and G. Kraft. Track structure and the calculation of biological effects of heavy charged particles. *Advances in Space Research*, 18(1–2):5–14, 1996.

D. Schulz-Ertner, C. P. Karger, A. Feuerhake, A. Nikoghosyan, S. E. Combs, O. Jaekel, L. Edler, M. Scholz, and J. Debus. Effectiveness of carbon ion radiotherapy in the treatment of skull-base chordomas. *International Journal of Radiation Oncology*Biology*Physics*, 68(2):449–457, 2007.

A. Schweikard, H. Shiomi, and J. Adler. Respiration tracking in radiosurgery. *Medical Physics*, 31(10):2738–2741, 2004.

J. Seco, D. Robertson, A. Trofimov, and H. Paganetti. Breathing interplay effects during proton beam scanning: simulation and statistical analysis. *Physics in Medicine & Biology*, 54(14): N283–N294, 2009.

P. G. Seiler, H. Blattmann, S. Kirsch, R. K. Muench, and C. Schilling. A novel tracking technique for the continuous precise measurement of tumour positions in conformal radiotherapy. *Physics in Medicine & Biology*, 45(9):N103–N110, 2000.

Y. Seppenwoolde, H. Shirato, K. Kitamura, S. Shimizu, J. V. Lebesque, and K. Miyasaka. Precise and real-time measurement of 3D tumor motion in lung due to breathing and heartbeat, measured during radiotherapy. *International Journal of Radiation Oncology*Biology*Physics*, 53(4):822–834, 2002.

M. Serban, E. Heath, G. Stroian, D. L. Collins, and J. Seuntjens. A deformable phantom for 4D radiotherapy verification: design and image registration evaluation. *Medical Physics*, 35(3): 1094–1102, 2008.

H. Shirato, S. Shimizu, K. Kitamura, T. Nishioka, K. Kagei, S. Hashimoto, H. Aoyama, T. Kunieda, N. Shinohara, H. Dosaka-Akita, and K. Miyasaka. Four-dimensional treatment planning and fluoroscopic real-time tumor tracking radiotherapy for moving tumor. *International Journal of Radiation Oncology*Biology*Physics*, 48(2):435–442, 2000a.

H. Shirato, S. Shimizu, T. Kunieda, K. Kitamura, M. van Herk, K. Kagei, T. Nishioka, S. Hashimoto, K. Fujita, H. Aoyama, K. Tsuchiya, K. Kudo, and K. Miyasaka. Physical aspects of a real-time tumor-tracking system for gated radiotherapy. *International Journal of Radiation Oncology*Biology*Physics*, 48(4):1187–1195, 2000b.

H. Shirato, M. Oita, K. Fujita, Y. Watanabe, and K. Miyasaka. Feasibility of synchronization of real-time tumor-tracking radiotherapy and intensity-modulated radiotherapy from viewpoint of excessive dose from fluoroscopy. *International Journal of Radiation Oncology*Biology*Physics*, 60(1):335–341, 2004.

Siemens. Siemens press picture. http://www.siemens.com/press/en/presspicture/. Internet source accessed on September 8th, 2011.

A. Smith, M. Gillin, M. Bues, X. R. Zhu, K. Suzuki, R. Mohan, S. Woo, A. Lee, R. Komaki, J. Cox, K. Hiramoto, H. Akiyama, T. Ishida, T. Sasaki, and K. Matsuda. The M. D. Anderson proton therapy system. *Medical Physics*, 36(9):4068–4083, 2009.

J. J. Sonke, J. Lebesque, and H. M. van. Variability of four-dimensional computed tomography patient models. *International Journal of Radiation Oncology*Biology*Physics*, 70(2):590–598, 2008.

M. F. Spadea, M. Peroni, E. Preve, M. Riboldi, G. Baroni, G. T. Chen, and G. C. Sharp. Uncertainties in lung motion prediction relying on external surrogate: a 4DCT study in regular vs. irregular breathers. *Technology in Cancer Research and Treatment*, 9(3):307–316, 2010.

B. Spielberger, M. Kraemer, M. Scholz, and G. Kraft. Three-dimensional dose verification in complex particle radiaion fields based on X-ray films. *Nuclear Instruments & Methods in Physics Research, Section B*, 209:277–282, 2003.

P. Steidl, J. Buerkelbach, D. Richter, D. Muessig, G. Sroka-Perez, T. Haberer, M. Durante, and C. Bert. Motion tracking using MV-fluoroscopy. *GSI Scientific Report 2009*, page 504, 2010.

P. Steidl, M. Durante, and C. Bert. A Software for Quantitative Analysis of Irradiated X-Ray Films. *GSI Scientific Report 2010*, page 467, 2011.

R. M. Sternheimer. The Density Effect fot the Ionization Loss in Various Materials. *Physical Review*, 88(4):851–859, 1952.

R. M. Sternheimer. Density Effect for the Ionization Loss of Charged Particles. *Physical Review*, 145(1):247–250, 1966.

R. M. Sternheimer and R. F. Peieris. General Expression for the Density Effect for the Ionization Loss of CHarged Particles. *Physical Review B*, 3(11):3681–3692, 1971.

R. M. Sternheimer, M. J. Berger, and S. M. Seltzer. Density Effect for the Ionization Loss of Charged Particles in Various Substances. *Atomic Data and Nuclear Data Tables*, 30(2):261–271, 1984.

M. Suzuki, Y. Kase, T. Kanai, and K. Ando. Correlation between cell killing and residual chromatin breaks measured by PCC in six human cell lines irradiated with different radiation types. *International Journal of Radiation Biology*, 76(9):1189–1196, 2000.

H. Tsujii, J. Mizoe, T. Kamada, M. Baba, S. Kato, H. Kato, H. Tsuji, S. Yamada, S. Yasuda, and et a. Ohno. Overview of clinical experiences on carbon ion radiotherapy at NIRS. *Radiotherapy and Oncology*, 73(Supplement 2):S41–S49, 2004.

Y. Tsunashima, T. Sakae, Y. Shioyama, K. Kagei, T. Terunuma, A. Nohtomi, and Y. Akine. Correlation between the respiratory waveform measured using a respiratory sensor and 3D tumor motion in gated radiotherapy. *International Journal of Radiation Oncology*Biology*Physics*, 60 (3):951–958, 2004.

Y. Tsunashima, S. Vedam, L. Dong, M. Umezawa, T. Sakae, M. Bues, P. Balter, A. Smith, and R. Mohan. Efficiency of respiratory-gated delivery of synchrotron-based pulsed proton irradiation. *Physics in Medicine & Biology*, 53(7):1947–1959, 2008.

Y. Y. Vinogradskiy, P. Balter, D. S. Followill, P. E. Alvarez, R. A. White, and G. Starkschall. Verification of four-dimensional photon dose calculations. *Medical Physics*, 36(8):3438–3447, 2009.

von M. Siebenthal, G. Szekely, U. Gamper, P. Boesiger, A. Lomax, and P. Cattin. 4D MR imaging of respiratory organ motion and its variability. *Physics in Medicine & Biology*, 52(6):1547–1564, 2007a.

von M. Siebenthal, G. Szekely, A. J. Lomax, and P. C. Cattin. Systematic errors in respiratory gating due to intrafraction deformations of the liver. *Medical Physics*, 34(9):3620–3629, 2007b.

U. Weber. *Volumenkonforme Bestrahlung mit Kohlenstoff-Ionen zur Vorbereitung einer Strahlentherapie*. PhD thesis, Universität Kassel, 1996.

U. Weber and G. Kraft. Design and construction of a ripple filter for a smoothed depth dose distribution in conformal particle therapy. *Physics in Medicine & Biology*, 44(11):2765–2775, 1999.

W. K. Weyrather, S. Ritter, M. Scholz, and G. Kraft. RBE for carbon track-segment irradiation in cell lines of differing repair capacity. *International Journal of Radiation Biology*, 75(11): 1357–1364, 1999.

WHO. http://www.who.int/cancer/en/. Internet source accessed on July 26th, 2011.

J. Wilbert, J. Wilbert, J. Meyer, J. Meyer, K. Baier, K. Baier, M. Guckenberger, M. Guckenberger, C. Herrmann, C. Herrmann, R. Hess, R. Hess, C. Janka, C. Janka, L. Ma, L. Ma, T. Mersebach, T. Mersebach, A. Richter, A. Richter, M. Roth, M. Roth, K. Schilling, K. Schilling, M. Flentje, and M. Flentje. Tumor tracking and motion compensation with an adaptive tumor tracking system (ATTS): System description and prototype testing. *Medical Physics*, 35(9):3911–3921, 2008.

Q. Wu, R. Mohan, M. Morris, A. Lauve, and R. Schmidt-Ullrich. Simultaneous integrated boost intensity-modulated radiotherapy for locally advanced head-and-neck squamous cell carcinomas. I: dosimetric results. *International Journal of Radiation Oncology*Biology*Physics*, 56(2): 573–585, 2003.

Q. Xu and R. J. Hamilton. A novel respiratory detection method based on automated analysis of ultrasound diaphragm video. *Medical Physics*, 33(4):916–921, 2006.

X. Yan, U. Titt, A. Koehler, and W. Newhauser. Measurement of neutron dose equivalent to proton therapy patients outside of the proton radiation field. *Nuclear Instruments & Methods in Physics Research, Section A*, 476(1–2):429–434, 2002.

S. M. Zenklusen, E. Pedroni, and D. Meer. A study on repainting strategies for treating moderately moving targets with proton pencil beam scanning at the new Gantry 2 at PSI. *Physics in Medicine & Biology*, 55(17):5103–5121, 2010.

T. Zhang, H. Keller, M. J. O'Brien, T. R. Mackie, and B. Paliwal. Application of the spirometer in respiratory gated radiotherapy. *Medical Physics*, 30(12):3165–3171, 2003.

J. F. Ziegler, J. F. Biersac, and U. Littmark. *The stopping and range of ions in solids*. Pergamon Press, first edition, 1985.

List of Figures

List of Tables

List of Abbreviations

4DCT	time resolved computed tomography
AP	anterior-posterior
BEV	beam’s eye view
CC	correlation coefficient
CT	computed tomography
CTV	clinical target volume
DAQ	data acquisition
DVH	dose volume histogram
EPID	electronic portal imaging device
FWHM	full width at half maximum
GCS	gating control system
GTV	gross tumour volume
GW	gating window
HIT	Heidelberg Ion-Beam Therapy Center
IARC	International Agency for Research on Cancer
IES	iso-energy slice
IMPT	intensity modulated particle therapy
IMRT	intensity modulated radiotherapy
ITV	internal target volume
laOF	lateral overlap factor
LDS	laser distance sensor
LET	linear energy transfer
LINAC	linear accelerator
loOF	longitudinal overlap factor
MDACC	MD Anderson Cancer Center
MRI	magnetic resonance imaging
NIRS	National Institute of Radiological Sciences
OD	optical density
PD	prescribed dose
PET	position emission tomography
PMMA	polymethyl methacrylate
PSI	Paul Scherrer Institut
PTV	planning target volume
PU	polyurethane
PVC	polyvinyl chloride
RBE	relative biological effectiveness
RiFi	ripple filter
RMS	root mean square
ROI	region of interest
RPM	Real-time Position Management™
RPTC	Rinecker Proton Therapy Center
SD	standard deviation
SI	superior-inferior
SOBP	spread out Bragg-peak
TCS	treatment control system
TPS	treatment planning system
UCHD	University Clinic Heidelberg
WHO	World Health Organisation

Publications of this work

P. Steidl, D. Richter, C. Schuy, E. Schubert, Th. Haberer, M. Durante, and C. Bert. A breathing thorax phantom with independently programmable 6D tumour motion for dosimetric measurements in radiation therapy. *Physics in Medicine & Biology*, Submitted: September 2011.

Scientific reports

P. Steidl, M. Durante, and C. Bert. A Software for Quantitative Analysis of Irradiated X-Ray Films. *GSI Scientific Report 2010*, page 467, 2011.

P. Steidl, J. Bürkelbach, D. Richter, D. Müssig, G. Sroka-Perez, Th. Haberer, M. Durante, and C. Bert. Motion tracking using MV-fluoroscopy. *GSI Scientific Report 2009*, page 504, 2010.

Patent application

P. Steidl, D. Richter, C. Schuy, E. Schubert, and C. Bert. Bestrahlungsphantom. *Patent application*, 10 2010 061 121.2 (DE), 2010.

Conference contributions

P. Steidl, D. Richter, C. Schuy, E. Schubert, Th. Haberer, M. Durante, and C. Bert. A Breathing Thorax Phantom with Independently Programmable 6D Tumor Motion. *50th Annual Meeting of Particle Therapy Co-Operative Group*, Poster presentation, 2011.

P. Steidl, D. Richter, A. Gemmel, Th. Haberer, M. Durante, and C. Bert. Gating and Residual Motion Studies at HIT. *4D Treatment Planning Workshop*, Oral presentation, 2010.

P. Steidl, D. Richter, N. Saito, J. Naumann, S. Brons, R. Panse, Th. Haberer, M. Durante, and C. Bert. Beam Parameters for Gated Irradiations of Moving Targets in Scanned Particle Therapy. *Medical Physics*, 37:3289, Poster presentation, 2010.

P. Steidl, J. Bürkelbach, D. Richter, G. Sroka-Perez, Th. Haberer, M. Durante, and C. Bert. Motion monitoring for particle therapy of intra-fractional moving targets. *DPG Spring Meeting*, Oral presentation, 2010.

Curriculum vitae

Personal data

Name	Peter Steidl
Birth	17.03.1983 in Hadamar
Marital status	single
Citizenship	German

Academic studies and education

Since 05/2009	Participant of the Helmholtz Graduate School for Hadron and Ion Research
04/2009–04/2010	U Heidelberg, advanced training "*Medical physics for physicists*"
Since 09/2008	Ph.D. study at GSI supervised by Prof. Marco Durante, Ph.D.
10/2002–08/2008	TU Darmstadt, diploma in physics Thesis title: "*A new control system for the high-energy rasterscan facility at GSI and precision measurements of Bragg ionisation functions*"
07/1993–06/2002	Fürst Johann Ludwig Schule, Hadamar (grammar school)
07/1989–06/1993	Mittelpunktschule St. Blasiu, Frickhofen (primary school)

Employment history

Since 09/2009	Research assistant at GSI
09/2008–08/2009	Scholarship holder at GSI (Ph.D. scholarship of the TU Darmstadt)
02/2009–08/2009	Graduate assistant at GSI
01/2005–12/2008	Working student at GSI

Voluntary work

04/2005–08/2005	Team leader at the XX. World-Youth-Day in Cologne
11/2003–10/2007	Member of the parish parochial council of St. Martin Frickhofen
05/1998–09/2002	Voluntary work as a youth group leader and leading altar server of St. Martin Frickhofen

Danksagung

Als Erstes möchte ich Prof. Marco Durante, Ph.D., danken, der mir eine so interessante und vielseitige Doktorarbeit in der Biophysik der GSI ermöglicht hat. Er hat immer ein offenes Ohr und hat mich immer sehr unterstützt.

Nicht minder möchte ich Prof. Dr. Dr. h. c. Gerhard Kraft herzlich danken. Er war nicht nur bereit, als Zweitgutachter meine Arbeit zu bewerten, sondern stand auch während der letzten Jahre jederzeit für die Diskussion offener Fragen zur Verfügung. Vielen Dank für viele wertvolle Anregungen.

Ebenfalls sehr herzlich möchte ich meinem Betreuer Dr. Christoph Bert danken, der trotz seiner größer werdenden Arbeitsgruppe und seiner wachsenden organisatorischen Aufgaben sich immer Zeit für mich genommen hat. Ohne eine so gute Betreuung wäre diese Doktorarbeit nicht möglich gewesen.

Von unserer Arbeitsgruppe, dem Motion-Team, möchte ich besonders Dankiel Richter danken für die intensive Unterstützung bei der Vorbereitung und Durchführung der zahlreichen Experimente am HIT sowie für seine Hilfe beim Phantombau. Vielen Dank auch an alle anderen ehemaligen und aktuellen Mitglieder des Motion-Teams für Unterstützung und eine hervorragende Arbeitsatmosphäre.

Von GSI-Mitarbeitern außerhalb des Motion-Teams möchte ich insbesondere Crhstoph Schuy und Elko Schubert für die Unterstützung bei Phantombau und Experimentaufbauten sowie Tanya Torres de Heidenreich für die Hilfestellung im Zusammenhang mit Fragen zur Automatisierungstechnik sehr herzlich danken.

Allen anderen Mitgliedern der Biophysik sei natürlich auch recht herzlich für die vielen kleinen Dinge gedankt, die an dieser Stelle nicht im Einzelnen aufgeführt werden können.

Von der Siemens AG möchte ich insbesondere Dr. Alexander Gemmel für die Unterstützung bei der Durchführung von Experimenten sowie für wertvolle Anregungen sehr herzlich danken. Ebenfalls Dank gebührt Andreas von Knobloch, der auch während nächtlicher Stunden telefonisch gerne beim Beheben technischer Probleme half.

Prof. Dr. Thomas Haberer möchte ich recht herzlich für die Ermöglichung der vielen Experimente am HIT danken. Er hat meine Projekte jederzeit gerne unterstützt. Ebenfalls möchte ich Prof. Dr. Oliver Jäkel für zahlreiche Anregungen danken. Insbesondere bei Dr. Stephan Brons, aber auch Dr. Ralf Panse, Dr. Jakob Naumann, Dr. Markus Winter, Dr. Peter Heeg, Dr. Naved Chaudhri, Benjamin Ackermann und Bernadette Hartmann möchte ich mich für die Unterstützung im Zusammenhang mit der Durchführung meiner Experimente am HIT danken.

Besonderer Dank gilt auch PD Dr. Katia Parodi für die Bereitstellung von Basisdaten für den gekreuzten RiFi.

Prof. Dr. Christian Karger, Dr. Torsten Moser und Andrés C. Vásquez T. möchte ich für die Nutzung des VisionRT-Systems an der Universitätsklinik Heidelberg danken. Andrés war mir darüber heraus immer gerne bei CT-Aufnahmen behilflich.

Dr. Dieter Oetzel, Dr. Gabriele Sroka-Perez, Dr. Frank Hensley, Gerald Major und insbesondere Dr. Josef Bürkelbach danke ich für die Unterstützung bei der Durchführung von Fluoroskopie-Experimenten an der Universitätsklinik Heidelberg.

Natürlich gilt auch mein Dank den an der Patientenstudie beteiligten Ärzten, MTRAs und natürlich den Patienten, die die Verlängerung der Patientenbehandlung gerne akzeptiert haben. Vor allen Dingen PD Dr. Holger Hof und PD Dr. Marc Münter möchte ich für die Ermöglichung und Unterstützung der Patientendatenacquisition recht herzlich danken.

Neben oben bereits erwähnten Personen haben Dr. Robert Kaderka und Robert Lüchtenborg dankenswerterweise sich die Zeit genommen, diese Arbeit Korrektur zu lesen.

Nicht zuletzt danke ich meiner Freundin Britta, meiner Familie und meinen Freunden, die mich immer unterstützen und unterstützt haben und insbesondere in der Fertigstellungsphase dieser Arbeit und während Strahlzeiten viel Verständnis für meine Häufige Abwesenheit aufgebracht haben.